



THE UNIVERSITY *of* EDINBURGH

Edinburgh Research Explorer

Microstructurally controlled trace element (Zr, U–Pb) concentrations in metamorphic rutile: An example from the amphibolites of the Bergen Arcs

Citation for published version:

Moore, J, Beinlich, A, Porter, JK, Talavera, C, Berndt, J, Piazzolo, S, Austrheim, H & Putnis, A 2019, 'Microstructurally controlled trace element (Zr, U–Pb) concentrations in metamorphic rutile: An example from the amphibolites of the Bergen Arcs', *Journal of Metamorphic Geology*.
<https://doi.org/10.1111/jmg.12514>

Digital Object Identifier (DOI):

[10.1111/jmg.12514](https://doi.org/10.1111/jmg.12514)

Link:

[Link to publication record in Edinburgh Research Explorer](#)

Document Version:

Peer reviewed version

Published In:

Journal of Metamorphic Geology

General rights

Copyright for the publications made accessible via the Edinburgh Research Explorer is retained by the author(s) and / or other copyright owners and it is a condition of accessing these publications that users recognise and abide by the legal requirements associated with these rights.

Take down policy

The University of Edinburgh has made every reasonable effort to ensure that Edinburgh Research Explorer content complies with UK legislation. If you believe that the public display of this file breaches copyright please contact openaccess@ed.ac.uk providing details, and we will remove access to the work immediately and investigate your claim.



**Microstructurally controlled trace element (Zr, U–Pb)
concentrations in metamorphic rutile: An example from the
amphibolites of the Bergen Arcs**

Jo Moore^{*1}, Andreas Beinlich¹, Jennifer K. Porter^{1, 3}, Cristina Talavera^{2, 3}, Jasper Berndt⁴,
Sandra Piazzolo⁵, Håkon Austrheim⁶, Andrew Putnis^{1, 4}

¹*The Institute for Geoscience Research (TIGeR), School of Earth and Planetary Sciences, Curtin
University, Perth, WA, 6845, Australia*

²*School of Geosciences, University of Edinburgh, The King's Buildings, James Hutton Road, EH9
3FE, Edinburgh, UK*

³*John de Laeter Centre, Curtin University, Perth, WA 6102, Australia*

⁴*Institut für Mineralogie, University of Münster, 48149 Münster, Germany*

⁵*School of Earth and Environment, University of Leeds, Leeds, UK*

⁶*Physics of Geological Processes (PGP), The Njord Centre, Department of Geosciences, University of
Oslo, 0316, Oslo, Norway*

**Corresponding author (Email address: josephine.moore@postgrad.curtin.edu.au, ORCID ID: 0000-
0003-1842-5595)*

18 **Abstract**

19 As a common constituent of metamorphic assemblages, rutile provides constraints on the
20 timing and conditions of rock transformation at high resolution. However, very little is
21 known about the links between trace element mobility and rutile microstructures that result
22 from syn-metamorphic deformation. To address this issue, here we combine in situ LA-ICP-
23 MS and SHRIMP trace element data with EBSD microstructural analyses to investigate the
24 links between rutile lattice distortions and Zr and U–Pb systematics. Furthermore, we apply
25 this integrated approach to constrain further the temperature and timing of amphibolite-facies
26 metamorphism and deformation in the Bergen Arcs of southwestern Norway. In outcrop, the
27 formation of porphyroblastic rutile in dynamically hydrated leucocratic domains of otherwise
28 rutile-poor statically-hydrated amphibolite provides key contextual information on both the
29 ambient conditions of hydration and deformation and the composition of the reactive fluid.
30 Rutile in amphibolite recorded ambient metamorphic temperatures of ~590–730°C during
31 static hydration of the granulitic precursor. In contrast, rutile from leucocratic domains in the
32 directly adjacent shear zone indicates that deformation was accompanied by a localized
33 increase in temperature. These higher temperatures are recorded in strain-free rutile (~600–
34 860°C) and by Zr concentration measurements on low-angle boundaries and shear bands
35 (620–820°C). In addition, we also observe slight depletions of Zr and U along rutile low-
36 angle boundaries relative to strain-free areas in deformed grains from the shear zone. This
37 indicates that crystal-plastic deformation facilitated the compositional re-equilibration of
38 rutile upon cooling to slightly below the peak temperature of deformation. Cessation of
39 deformation at mid-crustal conditions near ~600°C is recorded by late stage growth of small
40 (< 150 μm) rutile in the high strain zones. U–Pb age data obtained from the strain-free and
41 distorted rutile grains cluster in distinct populations of 437.4 ± 2.7 Ma and *c.* 405–410 Ma,
42 respectively. These different ages are interpreted to reflect the difference in closure for

thermally-induced Pb diffusion between undeformed and deformed rutile during post-deformation exhumation and cooling. Thus, our results provide a reconstruction of the thermochronological history of the amphibolite-facies rocks of the Lindås Nappe and highlight the importance of integration of microstructural data during application of thermometers and geochronometers.

KEYWORDS

Zr-in-rutile thermometry, U–Pb geochronology, deformation microstructures, amphibolite, high diffusivity pathways

1. INTRODUCTION

Accessory minerals are useful tracers of the timing and the conditions at which rocks undergo physical and chemical changes. Recognition of the strong temperature dependence of Zr-content in rutile (Tomkins, Powell, & Ellis, 2007; Watson, Wark, & Thomas, 2006; Zack, Moraes, & Kronz, 2004) has caused a growing interest in rutile due to its applicability as a metamorphic thermometer. Combined application of Zr-in-rutile thermometry with rutile U–Pb geochronology (e.g. Kylander-Clark, Hacker, & Mattinson, 2008; Zack et al., 2011; Zeh, Cabral, Koglin, & Decker, 2018) can therefore provide invaluable constraints on a rock's metamorphic history. While providing an abundance of important geochemical data, the incomplete understanding of the susceptibility of rutile composition to deformation and fluid alteration during metamorphism complicates its application as a thermochronometer in strained and hydrated rocks.

Most studies of rutile Zr-thermometry and U–Pb geochronology have either focused on high-temperature granulites that have undergone slow cooling (e.g. Kooijman, Mezger, & Berndt, 2010; Vry & Baker, 2006) or have been performed under anhydrous experimental

conditions (Cherniak, Manchester, & Watson, 2007). Thus, compositional re-equilibration of rutile is commonly attributed to volume diffusion, whereas the effects of deformation and fluid alteration have received relatively little attention. Accordingly, rutile ages are interpreted as the time at which the grain cooled below the closure temperature for volume diffusion (e.g. Dodson, 1973; Flowers, Bowring, Tulloch, & Klepeis, 2005; Ganguly & Tirone, 1999; Hirdes & Davis, 2002; Mezger, Hanson, & Bohlen, 1989). For grains larger than 200 μm in diameter the U–Pb system closure is estimated to be at 600°C (2–3°C/Ma cooling rate; Cherniak, 2000; Vry & Baker, 2006), and that of Zr above ~640°C (2°C/Ma cooling rate; Cherniak et al., 2007). This implies that rutile in retrogressed metamorphic rocks should generally display correlating age and temperature data. However, analyses of natural rutile suggest that the concept of closure temperature mostly applies to the U–Pb system, whereas the frequently observed lack of correlation between grain size and calculated temperatures implies that Zr concentrations in rutile are relatively insensitive to volume diffusion (Ewing, Hermann, & Rubatto, 2013; Pape, Mezger, & Robyr, 2016).

Therefore, investigation into post-crystallisation modification of Zr contents in rutile is of importance to applications of the thermometer. Recent studies have demonstrated that high-pressure fluid alteration may not only mobilize Zr from the rutile but also provide the required Si for zircon formation, thus controlling Zr partitioning with rutile (Harley, 2008; Luvizotto & Zack, 2009; Meyer, John, Brandt, & Klemd, 2011; Mitchell & Harley, 2017; Pape et al., 2016). In addition, the variability of Zr concentration within and among grains has been attributed to the proximity of nearby Zr-bearing phases and rutile grain morphology, further indicating a textural control on the Zr concentration in rutile (Ewing et al., 2013; Kooijman, Smit, Mezger, & Berndt, 2012; Mitchell & Harley, 2017; Pape et al., 2016). Thus, despite the apparent validity of closure temperatures for the U–Pb system, mechanisms other than volume diffusion need to be considered when interpreting Zr concentrations in rutile. In

addition to the mechanisms outlined above, it is reasonable to assume that rutile Zr and U–Pb contents may be further modified by deformation. Particularly, low-angle boundaries have been shown to act as fast diffusion pathways for trace elements in both pyroxene and zircon (Piazolo, Austrheim, & Whitehouse, 2012; Piazolo et al., 2016; Timms et al., 2011), enhancing the resetting of both temperature and age data. If the effect of deformation on composition is similarly significant in rutile, then previous observations of the inconsistent nature of temperatures recorded by rutile within samples may be partially explained.

In the Lindås Nappe of the Bergen Arcs in southwestern Norway the complete dehydration of rocks at granulite-facies conditions prior to the fluid-induced Caledonian tectonometamorphic amphibolite-facies overprint provides an ideal geological setting for investigating the effects of fluid-rock interaction and deformation on element mobility in rutile. We observe a spatial association between strain, fluid infiltration and rutile distribution in amphibolite-facies rocks. Through targeted sampling of rutile-rich high strain zones and fractures, we show how combined microstructural and geochemical analyses of rutile can constrain the hydration-deformation history of the Lindås Nappe amphibolite. Furthermore, we explore the link between deformation and trace element distribution in rutile, which highlights the benefit of incorporating microstructural analyses in future applications of the Zr-in-rutile geothermometer.

2. BACKGROUND AND OUTCROP DESCRIPTION

2.1. General background and previous geochronological work

The Bergen Arcs lie within the hanging wall of the extensional Bergen Arc shear zone. The arcs encompass the Øygards gneiss complex, structurally overlain by a set of nappes, including the Lindås Nappe, which is the focus of this study (Figure 1a). The Lindås Nappe mainly consists of an anorthosite-mangerite-charnockite-granite (AMCG) suite and banded gneiss complexes. Pulse-like intrusion of the AMCG suite occurred between 1237 Ma and

951 Ma (Bingen, Davis, & Austrheim, 2001), followed by pervasive recrystallization at granulite-facies conditions during the late Grenvillian-Sveconorwegian Orogeny at *c.* 930–910 Ma (Bingen et al., 2001; Cohen, O'Nions, Siegenthaler, & Griffin, 1988). Partial transformation of the granulite-facies rocks to eclogite and amphibolite-facies mineral assemblages advanced via localized fluid infiltration along fractures (Austrheim, 1987; Jamtveit, Bucher-Nurminen, & Austrheim, 1990) between *c.* 440 Ma and 420 Ma during the Caledonian Orogeny (Bingen et al., 2001).

Previously acquired geochronological data for the amphibolite-facies rocks of the Bergen Arcs define a broad time-span for amphibolite-facies metamorphism and deformation (Figure 1b). Amphibole Ar-Ar data record the oldest ages at 455 ± 2 Ma and 439 ± 4 Ma (Boundy, Essene, Hall, Austrheim, & Halliday, 1996). However, the validity of these early ages has been questioned based on the interpretation that these Ar-Ar data might reflect the presence of excess Ar in the amphiboles instead of constraining the cooling age below the closure temperature for Ar diffusion (Kühn, Glodny, Austrheim, & Råheim, 2002; Roffeis, Corfu, & Austrheim, 2012). Zircon generally records slightly younger U–Pb concordia ages between 426 ± 4 Ma and 430 ± 3 Ma (Glodny, Kühn, & Austrheim, 2008; Roffeis et al., 2012). One U–Pb age of 437 ± 11 was obtained from zircons that had been deformed by amphibolite-facies shear (Piazolo et al., 2012). A zircon U–Pb age of 418 ± 9 Ma (Kühn et al., 2002) and a 433 ± 3 Ma biotite Ar-Ar age (Fossen & Dunlap, 1998) from a sheared trondhjemite dyke are interpreted as directly recording the timing of amphibolite-facies deformation. These ages define a span of *c.* 20 Ma for the amphibolite-facies deformation. Rb-Sr multi-mineral isochron data provide the youngest age estimates at 414 ± 5 Ma (apatite, feldspar, white mica; Glodny et al., 2008) and 409 ± 8 Ma (apatite, amphibole, biotite; Bingen et al., 2001), consistent with the reported low temperature resetting of the Rb-Sr

system in mica, giving an estimate for the timing of crystallization of these lower temperature minerals.

Additional constraints on the timing of the amphibolite-facies metamorphism are given by biotite muscovite $^{40}\text{Ar}/^{39}\text{Ar}$ plateau ages from the Ulriken Gneiss unit immediately to the west of the Lindås Nappe (Fossen & Dunlap, 1998). Plateau ages of *c.* 410 Ma from greenschist-facies shear zones constrain the time of nappe stacking in the Bergen Arcs, marking the end of Caledonian contractional deformation. In addition to the amphibolite-facies rocks, pre- to syn-tectonic pegmatites have been dated by Rb-Sr and Sm-Nd multi-mineral isochron methods at *c.* 425 Ma (Kühn et al., 2002) and by U-Pb in zircons at 424 ± 1 Ma (Jamtveit et al., 2018). These dates, interpreted as crystallization ages, indicate that the mobility of hot silicate rich fluid was synchronous with metamorphism. However, the exact relationship between the emplacement of the pegmatites and the amphibolite-facies alteration remains unknown.

If interpreted as an isolated event, the geochronology derived from the amphibolite-facies mineral assemblages provides a sensible timeline. However, this apparent *c.* 430 Ma amphibolite-facies episode overlaps with the 429 ± 3 Ma (Glodny et al., 2008) and 423 ± 4 Ma (Bingen, Austrheim, Whitehouse, & Davis, 2004) ages derived from eclogite-facies assemblages that are intercalated with the amphibolites on Holsnøy (Figure 1b). This overlapping of ages has been explained by a west-to-east pressure decrease during simultaneous amphibolite- and eclogite-facies metamorphism (Roffeis et al., 2012). However, the interpretation remains contentious, since the characteristics and timing of the amphibolitization are somewhat ambiguous compared to the robustly constrained eclogite facies metamorphism.

Here we focus on integrating rutile Zr-thermometry, U-Pb age determination, and EBSD microstructural analyses to establish a rigorous temperature-deformation-time history

of the amphibolite-facies event. With an emphasis on distinguishing the deformational and metamorphic controls on the amphibolite-facies rutile temperature and age data.

2.2. Description of lithological relationships

The sampled outcrop, situated on Radøy in the northeastern part of the Lindås Nappe (Figure 1a) (UTM zone 31V, 620260E, 6718524N), includes three main lithologies; granulite, amphibolite, and leucocratic domains within the shear zone (Figure 2a). The amphibolite occurs between the other two lithologies. The granulite, characterized as a lilac corona-bearing medium-grained rock, shares an irregular and transitional contact with the amphibolite. Where the granulite grades into the amphibolite the foliation becomes defined by elongate amphibole clusters (1-2 cm in length), directly replacing coronitic diopside and garnet that define the foliation in the granulite. Strain increases markedly throughout the amphibolite towards the shear zone that contains additional leucocratic domains (Figure 2a). Within 50 cm from the first appearance of leucocratic domains, the foliation of the amphibolite grades into a 5-40 cm wide zone, where the foliation is defined by mafic and felsic bands with 5 mm spacing, marking the outer limit of the shear zone. In the following we refer to this part of the amphibolite as strained amphibolite. Within the shear zone, the 2-3 cm spaced foliation is defined by dark, amphibole- and feldspar-bearing amphibolite bands that alternate with creamy white leucocratic domains dominated by feldspar and strongly aligned clinozoisite.

In addition, the granulite contains two types of fractures (Figure 2b). Fracture type-I presents as a 1-2 cm wide plane hosting amphibole. Fracture type-II is apparent as 1-2 mm wide greenish fractures surrounded by white alteration haloes with a width of 1-2 cm, oriented subparallel to the high strain zone.

3. METHODS

3.1. Sample preparation

Polished thin sections were used for electron microprobe (EMP) analyses of rutile grains from the amphibolite and fracture alteration haloes. Additional EMP analyses were performed on plugs (3.8 mm diameter) drilled from lineation parallel (XZ) sections of leucocratic domains. Plugs were mounted in epoxy resin, polished initially with 6 μm and 1 μm diamond suspension fluid and given a final chemomechanical polish with colloidal silica for electron back-scatter diffraction (EBSD) analysis.

3.2. Imaging and quantification of rutile microstructures

Back-scatter electron (BSE) imaging and EBSD analyses were carried out on the Tescan Mira3 Variable Pressure Field Emission Scanning Electron Microscope (VP-FESEM) at the John de Laeter Centre (JDL), Curtin University, Australia. For both BSE and EBSD acquisition, the VP-FESEM was run at a high vacuum with an accelerating voltage of 20 kV and a beam current of 5.0 nA.

EBSD patterns were acquired with a HKL NordlysNano high sensitivity EBSD detector and indexed with AzTec analysis software (Oxford Instruments). The samples were tilted to 70° and analysed at a working distance of 20 mm to 24.5 mm. The step size ranged between 1 μm and 10 μm depending on the grain size and required spatial resolution. EBSD data was processed using HKL's Channel 5 software. Non-indexed solutions were replaced by the most common neighbour orientation to reduce data noise following the procedure outlined in Prior, Wheeler, Peruzzo, Spiess, and Storey (2002), Bestmann and Prior (2003) and Piazzolo, Bestmann, Prior, and Spiers (2006).

Mineral abbreviations used in the figures follow Whitney and Evans (2010).

3.3. U–Pb geochronology

The sensitive high-resolution ion microprobe (SHRIMP) analytical procedure broadly follows those described by Compston, Williams, and Meyer (1984) and Williams (1998). SHRIMP rutile data were collected from one mount (N17-44) over one analytical session at JDL. During this session, a 10-15 μm diameter spot for grains 30 and 32 and a 20-25 μm diameter spot for grains 29, 31 and 33 were used (Table S4b), with a mass-filtered O^- primary beam of ~ 7.6 -8.3 and 25.0-29.5 nA on rutile from a leucocratic domain sample, respectively. Data for each spot was collected in sets of 6 scans on the rutile through the mass range of $^{192}\text{Ti}_3\text{O}_3^+$, $^{200}\text{WO}^+$, $^{204}\text{Pb}^+$, Background, $^{206}\text{Pb}^+$, $^{207}\text{Pb}^+$, $^{208}\text{Pb}^+$, $^{248}\text{ThO}^+$, $^{254}\text{UO}^+$ and $^{270}\text{UO}_2^+$. The rutile age standard used was WH (Windmill Hill), a multigrain standard from an Archean quartzite, with a $^{206}\text{Pb}/^{238}\text{U}$ age of 2625 Ma (Clark, Hensen, & Kinny, 2000). WH has been calibrated against the Wodgina single rutile crystal described by Ewing (2011) and Ewing, Rubatto, Beltrando, and Hermann (2015) using the procedures described therein. Although we note that a small proportion of rutile grains from WH have $^{207}\text{Pb}/^{206}\text{Pb}$ ages slightly older than the dominant age population (manuscript in preparation), we only observe this in the more precise $^{207}\text{Pb}/^{206}\text{Pb}$ ages, not in the $^{206}\text{Pb}/^{238}\text{U}$ data. These "older" grains were avoided during analysis of the WH standard. No U standard was analysed during this session although estimated U contents are shown in Table S4b and based on the average U concentration in WH of 164 ppm. The common Pb correction was based on the measured ^{208}Pb due to the negligible Th contents on rutile. The programs SQUID II and Isoplot (Ludwig, 2003, 2009) were used for rutile data processing.

Uncertainties (2σ) cited for individual analyses include uncertainties from counting statistics and the common-Pb correction. Analyses for which the proportion of common Pb was $\geq 1.4\%$ were not considered in the age discussion or plotted on the Concordia diagram.

Weighted mean values for the mean age given on pooled analyses are at the 95% confidence level.

Rutile grains from leucocratic domains were analysed for U–Pb ratios by LA-ICP-MS at the Institut für Mineralogie, University of Münster, Germany. Ablation was done with an excimer laser (Analyte G2, Photon Machines) connected to a Thermo Fisher Scientific Element2 magnetic sector field single collector ICP-MS, at a repetition rate of 10 Hz and a spot size of 50 µm, producing a pit depth of ~ 30 µm. Prior to sample analyses, the system was tuned for high sensitivity, stability, and low oxide-interference rates ($^{232}\text{Th}^{16}\text{O}/^{232}\text{Th} < 0.05\%$). For rutile U–Pb measurements five unknowns were bracketed with two analyses of R10, which was used as external standard (Luvizotto et al. 2009). Along with the unknowns, secondary reference rutiles SP1 (Mezger et al., 1989, 911 ± 2 Ma), Sugluk-4 (Bracciali, Parrish, Horstwood, Condon, & Najman, 2013, 1723.0 ± 6.8 Ma), and R-632 (Axelsson et al., 2018, 496 ± 2 Ma) were analysed to check for precision and accuracy. Obtained results show good agreement with the published values (917.2 ± 8.5 Ma for SP1, 1729 ± 14 Ma for Sugluk-4, 505.9 ± 6.4 Ma for R-632). U–Pb rutile data were corrected for common Pb and processed following the procedures described in Kooijman, Berndt, and Mezger (2012) and Zack et al. (2011). A common Pb correction was applied to analyses if the contribution of the estimated common ^{206}Pb to the total measured ^{206}Pb exceeded 1%. The isotope ratios for the common Pb were calculated using the evolution model for terrestrial Pb by Stacey and Kramers (1975).

LA-ICP-MS and SHRIMP data are presented in Concordia, weighted mean, and radial plots, produced in IsoplotR (Vermeesch, 2018). Ages in figures are $^{206}\text{Pb}/^{238}\text{U}$ dates.

3.4. Trace elements and Zr-in-rutile thermometry

Rutile trace element concentration measurements by EMP ($n = 72$) were carried out on a field-emission JEOL 8530F Hyperprobe equipped with five Wavelength-Dispersive

Spectrometers at the Centre for Microscopy, Characterization and Analysis (CMCA), The University of Western Australia. Operating conditions were a beam energy of 25 keV, the beam current was 60 nA, and the beam was fully focused. Elements were acquired using the following analysing crystals: LiF for Ti K α , V K α , Cr K α , Mn K α , Fe K α , and Ni K α ; TAP for Si K α and Al K α ; and PETH for Ca K α , Zr L α and Nb L α . The standards employed were commercially available silicates, oxides, and metals. Counting time was 20 s for Ti K α , 70 s for Cr K α , Mn K α , Fe K α , Ni K α , Hf L α , Si K α , Al K α , Ca K α , Zr L α and Nb L α , and 100 s for V K α . Mean atomic number background corrections were employed throughout (Donovan and Tingle, 1996). Unknown and standard intensities were corrected for dead time and the ZAF algorithm was used for matrix absorption (Armstrong, 1988). On-peak interference corrections were applied as appropriate (Donovan et al., 1993). Detection limits ranged from 10 ppm for Ca to 40 ppm for Hf.

Rutile grains were analysed for trace elements also by LA-ICP-MS at the Institut für Mineralogie, University of Münster. For trace element analyses the NIST 610 glass was used as external standard while synthetic TNT666 and TNT777 glasses (Klemme et al., 2008) as well as natural rutile R10 (Luvizotto et al., 2009) were measured along with the unknowns to monitor precision and accuracy. Obtained results generally match the published range of concentrations given in the GeoReM database (version 23) (Jochum et al., 2005). Approximately 25 sample measurements were bracketed by three analyses of the external standard. ^{47}Ti was used as internal standard element. Trace element data reduction was performed using Glitter 4.4.4 (Griffin, 2008). For LA-ICP-MS the elemental concentrations were analysed by measuring the following isotopes: ^{238}U , ^{118}Sn , ^{121}Sb , ^{182}W , ^{95}Mo , ^{53}Cr , ^{66}Zn , ^{51}V , ^{181}Ta , ^{93}Nb , ^{90}Zr , and ^{178}Hf . The obtained trace element data were filtered to exclude all measurements with > 800 ppm Si showing abnormally high Zr contents, a method adapted

from Zack et al. (2004) and Luvizotto and Zack (2009) in an effort to detect zircon-lamellae rich rutile and zircon micro inclusions.

Zr-in-rutile thermometry calculations follow the method of Tomkins et al. (2007), using pressure estimates obtained from associated amphibole through Al-in-hornblende barometry (Johnson & Rutherford, 1989; Schmidt, 1991). For accurate estimates, the thermometer requires the presence of zircon and quartz in equilibrium with rutile. Representative amphibole compositions and pressure estimates are provided in Table S1.

4. RESULTS

4.1. General microstructural description of the main lithologies

The transition from granulite to amphibolite is marked by an overall grain size reduction and replacement of diopside-garnet coronas by amphibole clusters (Figures 3a and b). The amphibolite features 1 cm-scale interlayering of two characteristic domains; an amphibole-rich and a plagioclase-rich domain. The amphibole-rich domain is composed of amphibole with minor amounts of chlorite, biotite, quartz, and kyanite (Figure 3b). Within the amphibole-rich domain, trace amounts of rutile and pyrite are observed associated with replaced diopside. The plagioclase-rich domain is composed of plagioclase with minor amounts of zoisite, kyanite, quartz and CO₃-rich scapolite (Figure 3b). The replacement of diopside and garnet by amphibole is also observed in alteration haloes around fractures type-I and II (Figure 4a).

In the strained amphibolite, interlayering of amphibole and plagioclase domains occurs on a finer, 1 mm-scale (Figure 3c). Amphibole-rich and plagioclase-rich domains of the strained amphibolite differ from those in the amphibolite in that they contain a higher abundance of clinozoisite and zoisite.

In the shear zone the foliation is defined by mm-scale interlayering of dark amphibole-rich with plagioclase-rich domains (Figure 3d), consistent with the lithological variation in the strained amphibolite. On the cm-scale, these dark bands are interlayered with porphyroblastic rutile-bearing leucocratic domains (Figures 3d and 5a). In areas of increased leucocratic component, small ($< 100\ \mu\text{m}$) plagioclase and zoisite grains dominate the rock and define the foliation (Figures 3d and 5b, c). In these areas clinozoisite and biotite laths are aligned with the foliation (S; Figure 3d) and form in shear bands at $\sim 30^\circ$ to S (C; Figure 5a).

4.2. General occurrence of rutile and its mineral association

Rutile occurs as an accessory phase (< 1 volume %) in all lithologies except for the granulite. Rutile always occurs together with quartz and zircon, except in the fracture alteration haloes where zircon is absent. In general, rutile overall abundance and grain size positively correlate with clinozoisite, biotite, quartz, CO_3 -rich scapolite and tschermakite abundances.

4.2.1. Amphibolite

Hydration of granulite to amphibolite proceeded through the replacement of granulite-facies diopside by secondary clusters of Mg-hornblende, tschermakite, quartz, carbonate and rutile (Figures 3b and 4b). In the strained parts of the amphibolite rutile grains ($< 10\ \mu\text{m}$) are associated with amphibole clusters, whereas larger rutile grains ($< 150\ \mu\text{m}$) occur in association with small ($< 100\ \mu\text{m}$) clinozoisite grains, very small zircon grains ($< 20\ \mu\text{m}$) and large grains ($< 1\ \text{mm}$) of biotite that are aligned with the foliation (Figure 4c).

4.2.2. Fracture alteration haloes within granulite

The fracture filling assemblage of type-I fractures comprises quartz and tschermakite (Figure 4a). Alteration haloes around type-I fractures in the granulitic anorthosite, visible only in thin section, contain abundant rutile in amphibole clusters (Figure 4d). Here, rutile grains are equant and rounded with diameters of up to $30\ \mu\text{m}$. On the outer edge of the

fracture type-I alteration halo, diopside is replaced by symplectites of magnesio-hornblende, clinozoisite, quartz, and rutile (Figure 4e).

Type-II fractures predominantly contain quartz, with minor amounts of fine-grained (< 10 μm) biotite and amphibole. Type-II fracture alteration haloes are visible at both the outcrop and thin section scale due to abundant zoisite inclusions in the host plagioclase, producing a milky white appearance. In the alteration halo, rutile is present in clinozoisite- and pargasite-filled fractures in diopside as clusters of rounded-cusped shaped grains ranging in diameter between 10 μm and 30 μm (Figure 4f). Zircon is not observed in association with either fracture types.

4.2.3. Leucocratic domains

The leucocratic domains of the shear zone are the primary rutile-bearing lithology. In the shear zone the mineralogical variation typical of the strained amphibolite is evidenced by amphibole-rich foliation-parallel bands primarily consisting of Mg-hornblende with tschermakitic rims, quartz and minor amounts of clinozoisite and rutile (< 20 μm in diameter) (Figure 5f). Where the strained amphibolite is interlayered at a higher frequency with the leucocratic domains, there is an increase in tschermakitic amphibole, coarse grained rutile (< 200 μm diameter), biotite and clinozoisite, concomitant with a decrease in Mg-hornblende (Figure 5d). In areas where the amphibole domains of the strained amphibolite are no longer interlayered with the leucocratic domains, the mafic component primarily consists of (< 1 mm) foliation-parallel laths of clinozoisite and biotite and porphyroblastic rutile (< 1 mm), aligned with their long axes parallel to the foliation (Figure 5b).

In plagioclase-dominated areas of the leucocratic domains, porphyroblastic rutile, biotite, CO_3 -rich scapolite and clinozoisite occur in S and C foliation parallel bands (Figure 5a, e). Rutile also occurs as foliation-parallel grains in the felsic component of the leucocratic rock together with plagioclase, kyanite, zoisite and quartz but only minor amounts of biotite

and clinozoisite (Figure 5c). Throughout the leucocratic domains zircon occurs as very small grains ($< 10\ \mu\text{m}$) on the rim of rutile (Figure 5b and c) and, uncommonly, as inclusions within the rutile grain (Figure 5c).

4.3. Details of rutile microstructures and quantitative orientation analysis

Since the leucocratic domains are the main rutile-bearing lithology, most of this section investigates rutile in the leucocratic domains unless stated otherwise. Rutile is categorized based on grain size, morphology, structure and the mineral assemblage described above. A first order division is made based on grain size into subsets of large ($> 150\ \mu\text{m}$) and small grains ($< 150\ \mu\text{m}$).

Large porphyroblastic rutile is mostly present as substructure-free grains (Figure 6a, b) that exhibit an internal grain orientation spread (GOS) of $< 1^\circ$. Porphyroblastic rutile has a highly irregular grain shape, typically displaying cusped protrusions into the surrounding matrix (e.g. Figure 6a). Most commonly, these grains are observed in the leucocratic domains (Figures 6a and c) and only one occurrence was found in an amphibole cluster within the amphibolite (Figure 6b).

However, there are substructured large porphyroblastic rutile grains showing a GOS of $> 1^\circ$ (Figures 7a, e and h). For these grains, four types of substructures can be identified: (1) shear bands; (2) continuous lattice bending and low-angle boundaries; (3) distinct, straight growth twins and (4) deformation twins. To exclude the possibility that the observation of substructured versus substructure-free grains is due to an orientation effect, the c-axis orientations of all large grains have been plotted (Figure S1), demonstrating no preferred orientations for grains of either structure.

Shear bands are observed in large rutile ($> 150\ \mu\text{m}$) and are associated with a high occurrence of recrystallized rutile and/or kyanite inclusions and are marked by a change in

trace element chemistry (Figure 8) and a $\sim 4^\circ$ grain orientation change across the plane (Figure 7a). Misorientation data for large substructured rutile grains identify three types of lattice distortions (Types-I to -III) associated with low-angle boundaries and/or shear bands. The first type, Type-I, is observed at low-angle boundaries associated with shear bands with a rotation axis near $\langle 112 \rangle$, lying on the low-angle boundary wall (Figure 7b and c). Shear bands are distinguished from continual lattice bending by their sharp misorientation profile. The misorientation profile across the boundary (A-A'; Figure 7d) shows a sharp change in orientation at the low-angle boundaries on the order of $\sim 1^\circ/\mu\text{m}$, without significant orientation variation outside of the bounding low-angle boundaries.

Low-angle boundaries appear as subparallel discontinuous bands, which are most commonly parallel to the short axis of the grain (Figure 7e). They may be associated with continuous lattice bending on either side of the low-angle boundary (Figure 7g). Continuous lattice bending is associated with Type-II lattice distortions. Type-II lattice distortions are characterized by their lamellar, subparallel appearance (Figure 7e) and a rotation axis lying approximately on the pole to the (110)-plane (Figure 7f). The misorientation profile across lamellar boundaries (B-B'; Figure 7g) indicates stepwise misorientation on the order of $0.6^\circ/\mu\text{m}$ at each boundary wall, resulting in a progressively increasing misorientation relative to the original grain orientation.

While both twin types are identified as a 65° misorientation around [010], deformation twins are differentiated from growth twins based on their characteristic thin and tapered appearance (e.g. Figures 6a and 7a, e). In contrast, growth twin boundaries appear lobate and irregular (e.g. Figure 7h). Type III lattice distortions are commonly spatially related to growth twinning (Figure 7h). Type-III lattice distortions are exclusively present within the outer 100 μm of the grain and are characterized by a rotation axis lying approximately on the pole to the (100)-plane (Figure 7i). Overprinting relationships between the different lattice distortion

types indicate that deformation twinning preceded the formation of shear bands and growth twins (Figure 7a), but occurred after at least some crystal lattice bending and is associated with the formation of low-angle boundaries (Figure 7e).

Small rutile grains occur either associated with porphyroblastic biotite (Figures 4c and 5e) or around large porphyroblastic rutile grains (Figure 5b). These grains exhibit a GOS of $< 1^\circ$ and very rarely show any low-angle boundaries or crystal lattice bending.

4.4. Trace element geochemistry

Fifty-one LA-ICP-MS trace element spot analyses were obtained from 39 rutile grains in the leucocratic gneiss. Trace element concentrations are summarised in Table S2 and plotted against distance to the grain boundary (Figure 8).

Hafnium, Zr and U concentrations show systematic changes in large grains vs. small grains, shear bands, low-angle boundaries and twins (Figure 8a, c and d). Due to the thin width of deformation twins and the resolution of the instruments used, trace element analyses of deformation twins could not be performed, hence chemical characteristics of only the growth twins are provided. The concentration of U is generally between 0.1 ppm and 18 ppm with an average concentration of 6 ppm. In substructure-free grains, the average U concentration is 8 ppm. In contrast, small grains and grains with irregular twins and shear bands have less than 5 ppm U. Grains with low-angle boundaries have on average 3 ppm U. The average concentrations of Zr and Hf of all analysed grains are 1260 ppm and 35 ppm, respectively. If only substructure-free grains are considered, the average concentrations of Zr and Hf are 1500 and 40 ppm, in comparison to an average of 950 ppm Zr and 30 ppm Hf for spot analyses on grains containing low-angle boundaries and 265 ppm Zr and 11 ppm Hf average concentrations in small grains and growth twins. Concentrations of V, Nb and Ta vary non-systematically (Figure 8b, e and f).

4.5. Zr-in-rutile thermometry

Rutile Zr concentrations and calculated temperature estimates for all rutile-bearing lithologies are summarised in Table S3 (Figure 9). The Al-hornblende pressure estimates used in the calculation are derived from tschermakite, ranging from 10 kbar to 14 kbar (Table S1). In the amphibolite, rutile contains between 146 ppm (607 ± 27 °C) and 572 ppm Zr (727 ± 17 °C) (Figure 9a). Small rutile from the strained amphibolite contains between 74 ppm Zr (557 ± 35 °C) and 247 ppm Zr (655 ± 22 °C) (Figure 9c). The Zr concentration in rutile from type-I fracture alteration haloes varies between 125 ppm (588 ± 28 °C) and 462 ppm (690 ± 18 °C), whereas rutile from type-II fracture haloes shows a narrower range between 238 ppm (640 ± 23 °C) and 470 ppm (696 ± 18 °C) (Figure 9b).

Rutile from the leucocratic domains shows the largest variation in Zr concentrations, ranging from 97 ppm (598 ± 32 °C) to 2331 ppm (861 ± 45 °C). Substructure-free areas in large rutile grains show a slightly smaller spread in Zr concentrations between 230 ppm (637 ± 23 °C) and 2331 ppm (861 ± 45 °C) (Figure 9f). Shear bands have a Zr concentration of up to 1330 ppm (797 ± 31 °C), while low-angle boundaries contain between 184 ppm (620 ± 25 °C) and 1690 ppm Zr (823 ± 33 °C) (Figure 9e). Small grains and growth twins in the leucocratic domains record lower values, ranging between of 97 ppm (598 ± 32 °C) to 262 ppm (669 ± 22 °C) (Figure 9d) and 231 ppm (638 ± 26 °C) to 596 ppm (718 ± 37 °C) (Figure 9e), respectively.

4.6. Rutile U–Pb Geochronology

Ninety-eight analyses were obtained from 33 large grains in the leucocratic domains by LA-ICP-MS ($n = 68$; 28 grains) and SHRIMP ($n = 30$; 5 grains) (Table S4). The results are shown in Concordia and radial plots (Figure 10). All rutile grains have less than 10% common Pb, defined here as the percentage of common ^{206}Pb on total ^{206}Pb . Common Pb ranges between 1.7 to 9.9% for LA-ICP-MS analyses and 0.4 to 1.4% for SHRIMP analyses.

4.6.1. LA-ICP-MS analyses

All analyses yield overlapping concordant ages, producing a LA-ICP-MS Concordia age of 416.4 ± 1.7 Ma (Figure 10a). By excluding LA-ICP-MS data points with more than 5% discordance ($n = 4$), the mean LA-ICP-MS age is 415.7 ± 2.7 Ma with a mean square weighted deviation (MSWD) of 2.0 (Figure 10c). Radial plots indicate that the LA-ICP-MS data are consistent with multiple age groups. For ages obtained by LA-ICP-MS, 36% of the analyses correspond to an age of 438.2 ± 5.9 Ma and 64% of the analyses correspond to an age of 404.8 ± 4.2 Ma (Figure 10e).

4.6.2. SHRIMP analyses

SHRIMP analyses produce a Concordia age of 419.6 ± 1.4 Ma (Figure 10b). For the calculated SHRIMP mean age of 419.2 ± 3.3 Ma all analyses were considered. However, the elevated MWSD of 5.6 (Figure 10d) indicates over-dispersion of the data relative to the estimated analytical uncertainty. Age data obtained by SHRIMP define two age populations of 437.4 ± 2.7 Ma (39%), 409.1 ± 2.2 Ma (57%) and one analysis with a younger date at 379.9 ± 7.2 Ma (3.6%) (Figure 10f).

5. DISCUSSION

5.1. Origin of rutile

Rutile exhibits distinct textures and a heterogeneous distribution in the different assemblages that result from localized deformation and/or hydration reactions. Large rutile is particularly abundant in leucocratic domains, whereas only a small quantity of fine-grained acicular to rounded rutile occurs in fracture alteration haloes and in the amphibolite (Figures 4, 5, and 11). The Ti required to form this fine-grained rutile in the amphibolite is most likely derived from the breakdown of the diopside during hydration, as evidenced by the spatial association between relict diopside and rutile (Figures 3b and 4b). Textural features, such as the cusped grain boundary morphology and the clustering of the rutile grains in the

leucocratic domains (Figures 5b - d) and fracture alteration haloes (Figures 4d and f) indicate that rutile in these areas precipitated from a grain boundary fluid. This is consistent with the general requirement of fluid for driving the retrogression of the granulite to amphibolite (Austrheim & Robins, 1981). Furthermore, the correlated abundance of rutile with tschermakite, clinozoisite, CO₃-rich scapolite, quartz and biotite in both fracture alteration haloes (Figures 4e, f) and leucocratic domains (Figure 5b) suggests a genetic link between rutile precipitation and the composition of the alteration fluid resulting in the described assemblage. In particular, the presence of quartz in fractures that are surrounded by rutile-rich alteration haloes (Figure 4a) likely reflects cm-scale Ti mobilisation in a Si-bearing fluid. Concomitant Si and Ti mobility is in agreement with experimental and natural observations of enhanced rutile solubility in Na-Al-Si-bearing crustal fluids, indicating that complexing with major rock-forming constituents is governing Ti mobility in fluids in addition to pressure and temperature (Antignano & Manning, 2008; Gao, John, Klemm, & Xiong, 2007; John, Klemm, Gao, & Garbe-Schönberg, 2008; Rapp, Klemme, Butler, & Harley, 2010). Hence, the spatial affinity between rutile grains and their host lithology suggests that both fractures and leucocratic domains acted as pathways channelizing Na-Al-Si-bearing fluid. Without more data concerning the chemical properties of the Na-Al-Si-bearing fluid it is not possible to make the distinction of whether it is in the form of a hydrous melt or an aqueous solution, both of which may be stable at the determined PT conditions (see discussion below for conditions) (Bureau & Keppler, 1999; Hermann, Spandler, Hack, & Korsakov, 2006; Manning, 2004). Nevertheless, in remainder of the discussion the Na-Al-Si-bearing fluid is distinguished from the fluid that forms the amphibolite due to a higher solute concentration.

5.2. Deformation microstructures of rutile

Low-angle boundaries are consistent with subgrain boundaries, some of which may have formed via crystal-plastic mechanisms. To date, very few examples of natural

deformation microstructures in rutile have been reported in the literature (e.g. Plavsa et al., 2018; Puelles et al., 2017). Nevertheless, experimental observations provide evidence for the activation of two slip systems in rutile, the $\{101\}\langle -101 \rangle$ system and the $\{110\}[001]$ system (Ashbee & Smallman, 1963; Hirthe & Brittain, 1963). These earlier studies attribute the activation of the different systems to the crystal orientation relative to the compressive axis during deformation, independent of temperature. Following these initial investigations, Blanchin, Bursill, and Lafage (1990) reported on the activation of the $\{101\}\langle -101 \rangle$ and $\{110\}[001]$ slip systems at temperatures above 600°C and 900°C, respectively. However, for the investigated substructured rutile grains the rotation axis orientations of $[110]$ and $[100]$ (Figures 7f and i, respectively) combined with the subgrain boundary geometry indicate activation of both the $\{101\}\langle -101 \rangle$ and the $\{110\}[001]$ slip systems during deformation (Figures 7f and i). The $[112]$ rotation axis observed on the shear band (Figures 7b and c) may be a result of the activation of multiple slip systems, unresolvable with the current EBSD data. It is unlikely that temperatures exceeded 900 °C during deformation, supporting the observation of temperature independence of slip system activation, thus highlighting the need for further research on rutile deformation-induced microstructures.

5.3. Conditions of rutile precipitation, deformation and recrystallization

The basic assumption made when applying the Zr-in-rutile thermometer is that activities of Zr and Si are 1 during rutile crystallization and re-equilibration (Tomkins et al., 2007; Watson et al., 2006; Zack et al., 2004). This condition is usually satisfied if it can be demonstrated that rutile precipitated in the presence of zircon and quartz, in which case the Zr-in-rutile temperature is representative of the rutile formation temperature. By contrast, the lack of zircon and/or quartz during rutile formation is equivalent to reduced Zr- and Si-activities, in which case the calculated temperature is either an overestimate ($a_{\text{Si}} < 1$) or underestimate ($a_{\text{Zr}} < 1$). If the presence of zircon and quartz can be demonstrated, then the

variability of Zr concentration of rutile allows for evaluation of post-formation Zr mobilization. In our samples rutile always occurs together with quartz and zircon is only absent from the fracture halo assemblage (Figures 3, 4 and 5). Furthermore, rutile likely crystallized in the presence of a Na-Al-Si-bearing fluid. Therefore, we infer that the high Zr-in-rutile temperatures reflect the temperature conditions during rutile growth and that the lower temperatures measured along deformation microstructures may be attributed to Zr mobilization during subsequent cooling.

Zr-in-rutile temperature estimates obtained for the amphibolite and the fracture alteration haloes are between $588 \pm 28^{\circ}\text{C}$ and $727 \pm 17^{\circ}\text{C}$ (Figures 9a and b) and the pressure range of 10-14 kbar for the crystallization of tschermakite has been estimated by amphibole barometry (Table S1). This PT range is consistent with estimates of $\sim 700^{\circ}\text{C}$ and 9-11 kbar obtained through thermodynamic modelling of the amphibolite assemblages in this outcrop (Moore, Beinlich, Austrheim, & Putnis, 2019). They are also consistent with estimates of 690°C and 10-12 kbar for petrographically similar amphibolites of the Bergen Arcs (see Figure 1a for locality; Boundy et al., 1996) that are based on the garnet-amphibole thermometer of Graham and Powell (1984), the hornblende-plagioclase thermometer of Blundy and Holland (1990) and garnet-rutile-ilmenite-plagioclase-silica (GRIPS) barometry (Bohlen & Liotta, 1986). The consistency with previously reported metamorphic conditions corroborates our PT estimate for the granulite hydration and indicates that rutile from the amphibolite is likely to be in equilibrium with its host assemblage.

In contrast, Zr-in-rutile temperature estimates for the leucocratic domains in the shear zone are between $598 \pm 32^{\circ}\text{C}$ and $861 \pm 45^{\circ}\text{C}$ (Table S3; Figure 9f), which are higher than most previously reported temperatures for the amphibolites of the Lindås Nappe. However, similar values ($874 \pm 26^{\circ}\text{C}$) are reported by Piazzolo et al. (2012) using Ti-in-zircon thermometry on undeformed inherited zircons hosted within veins cross-cutting an

anorthosite body in the Lindås Nappe. While the authors report the possibility of an erroneously high temperature due to potential integration of undetected rutile micro-inclusions during the zircon analysis, the similarity with our temperature estimate may also represent evidence for a high temperature Si-rich fluid event in the Lindås Nappe. Furthermore, temperature values obtained from deformed porphyroclastic zircon (~760 - 820°C; Piazzolo et al., 2012) are also similar to those obtained from low-angle boundaries of large rutile (~620 – 820°C; Figure 9e), reflecting deformation near peak metasomatic temperatures.

The closure temperature for volume diffusion of Zr-in-rutile with a grain radius of 200 μm is between 635 °C to 725 °C, for an initial temperature of 800°C and cooling rates of 1 and 10°C/Ma, respectively (Cherniak et al., 2007; Dodson, 1973; Ganguly & Tirone, 1999). Hence, even at fast cooling rates, large rutiles should have been modified by volume diffusion of Zr during cooling and temperatures up to ~860°C should not have been preserved. The lack of Zr diffusion profiles in rutile, i.e. Zr-depleted rims in large rutile (Figure 8c) thus indicates that volume diffusion does not mobilize Zr during cooling. Therefore, we infer that the high temperature recorded reflects the thermal condition during rutile crystallization. However, we observe systematically lower Zr concentrations at low-angle boundaries compared to the undeformed parts of the same grains (Figure 8c). This correlation may hint at enhanced geochemical exchange through fast-diffusion pathways in areas of high dislocation density, as previously described for zircon (Timms, Reddy, Gerald, Green, & Muhling, 2012), feldspar (Kramer & Seifert, 1991; Yund, Smith, & Tullis, 1981), garnet (Büttner & Kasemann, 2007), and pyroxene (Chapman, Clarke, Piazzolo, Robbins, & Trimby; Lund, Piazzolo, & Harley, 2006). Strain-enhanced diffusion occurs via crystallographic ordering and disordering due to the increased atomic mobility around dislocation cores (pipe diffusion). Both “static” and “dynamic” modals of strain-enhanced

diffusion have been proposed by previous workers. The dynamic model of strain-enhanced diffusion may only occur during the creep of dislocations, elemental mobility being enabled by dislocation climb or glide (Kramer & Seifert, 1991; Yund & Tullis, 1980). During creep, dislocations organise into lower energy arrangements, i.e. low-angle boundaries, forming fast diffusion pathways. This is the static model for strain-enhanced diffusion, where the grain size is effectively decreased due to the introduction of fast diffusion pathways, lowering the closure temperature and allowing increased interaction with infiltrating fluids (Büttner & Kasemann, 2007; Plümper et al., 2012; Reddy, Timms, Pantleon, & Trimby, 2007; Timms et al., 2011). While the models are not mutually exclusive, only the dynamic model of strain-enhanced diffusion is in agreement with the sustained record of high temperatures (up to ~820°C) along low-angle boundaries, as these temperatures indicate that diffusion of Zr along dislocation cores was not effective during post-deformational cooling but during active deformation. These results indicate that while volume diffusion may not effectively equilibrate Zr-in-rutile, the distortion of the crystal-lattice during deformation may enhance the mobility of trace elements within the affected lattice.

Calculated temperatures from small rutile grains from the leucocratic domains (~610 - 670°C) and rutile in the strained amphibolite (~560 – 660 °C) are distinctly lower than those of large rutile in the leucocratic domains (Figures 9c and d). These small grains, mostly present within biotite porphyroblasts (Figures 4c and 5e) and around large porphyroblastic rutile grains (Figure 5b), have a textural positioning that is consistent with late stage growth. The low Zr-content and the textural positioning of small grains suggest that these are new rutiles that precipitated at lower temperatures. Thus, the variability in Zr-in-rutile within the amphibolite-facies shear zone is attributed to initial growth of rutile at high temperatures followed by the remobilization of Zr along high diffusivity pathways during lattice distortion, and finally, late stage growth of small rutiles at lower temperatures.

Growth twins exhibit trace element concentrations that are more similar to those measured on low-angle boundaries (Figures 8 and 9e) than to substructure-free grains, suggesting that twinning also enhances Zr mobility. Even though the idea of twin boundaries acting as fast diffusion-pathways in rutile has been suggested previously (Zack & Kooijman, 2017), data with higher spatial resolution is still needed for further confirmation.

5.4. Timing of rutile crystallization and deformation

We consider the two age populations defined by SHRIMP U–Pb data (Figure 10f) (437.4 ± 2.7 Ma, 409.1 ± 2.2 Ma) as statistically valid. While the statistical analysis of the U–Pb data obtained from LA-ICP-MS and SHRIMP yielded consistent age populations, the relationship between age and grain microstructure can only be resolved with confidence by SHRIMP data due to its superior precision and spatial resolution (Figure 10). The combination of EBSD and SHRIMP data shows an apparent positive correlation of age with GOS, i.e. the apparently younger grains ($n = 2$) exhibit a larger orientation spread than the “older” undeformed grain (Figure 10f). The relationship between grain microstructure and LA-ICP-MS ages is consistent with the correlation found for the SHRIMP ages (Figure 10e; Table S4).

The resetting of U–Pb ages due to diffusive transport of mainly Pb from the rutile into the surrounding matrix is controlled by temperature and the diffusion length scale (Dodson, 1986). Consequently, closure temperatures are grain size dependent, while the cooling rate determines the timescale for diffusion to occur above the closure temperature (Cherniak, 2000; Kooijman et al., 2010; Vry & Baker, 2006). In addition, enhanced diffusion of U and Pb as has been demonstrated to occur at low-angle boundaries in zircon (Piazolo et al., 2016; Timms et al., 2011) and enhanced elemental diffusion in other deformed silicates such as pyroxene, feldspar and garnet (e.g. Chapman, Clarke, Piazolo, Robbins, & Trimby, 2019; Lund et al., 2006; Yund et al., 1981). The continued post-deformational loss of Pb is in

agreement with a static strain-enhanced diffusion model rather than a dynamic one (as described above for Zr). The presence of low-angle boundaries in rutile grains is expected to reduce the diffusion length scale, thus enhancing U and Pb transport, equivalent to lowering the closure temperatures for deformed grains versus undeformed grains of equal size. In such a scenario low-angle boundaries enhance element mobility and enable continuous re-equilibration during fluid-assisted deformation.

Indeed, U concentrations at low-angle boundaries and in growth twins (Figure 8a) are too low for reliable age determination. This indicates a likely mobility of U associated with the formation of low-angle boundaries subsequent to lattice distortion, suggesting that U mobility was syn-deformational. Due to its smaller ionic radii, Pb should diffuse much faster than U (Dowty, 1980; Fortier & Giletti, 1989), as a result Pb-loss should have continued after crystal-plasticity of rutile became inactive, if the rocks remained at mid-crustal temperatures. This does not however, reconcile the static diffusion of Pb versus the dynamic diffusion of U and Zr, the contrasting modes of mobility insinuating that there must be a further crystallographic influence on the diffusion of these elements, unresolvable with the data presented here. Thus, deformation-induced open system behaviour of both U and Pb provides an explanation for the bimodality of the measured rutile age data, the younger age reflecting the eventual closure for Pb diffusion in substructured grains.

5.5. Temperature-time-deformation path

The field relationships, temperature conditions, fluid composition and the geochronological data can be integrated to develop a comprehensive thermal and deformation chronology for the amphibolites of the Lindås Nappe. The rutile microstructures and corresponding U–Pb and Zr-in-rutile analyses are illustrated in Figure 11.

5.5.1. Stage 1 – Syn-tectonic fluid infiltration at lower to mid-crustal conditions

The location of type-I and –II fractures in the outcrop (Figure 2b) together with assemblages present within the fractures and the surrounding alteration haloes suggest that they either represent (1) a record of initial fluid infiltration along brittle fractures and were subsequently overprinted by hydration and deformation and/or (2) localized sites of brittle failure during hydration within the dry protolith. Both scenarios are consistent with syn-deformation fluid infiltration as has been suggested as the general mechanism for hydration of the Lindås Nappe (Austrheim, 1987; Jamtveit et al., 1990). Syn-tectonic fluid infiltration is further supported by the subparallel alignment of biotite, clinozoisite and rutile porphyroblasts in the leucocratic domains (Figures 5a, b, and e). Furthermore, the presence of similar mineral assemblages and the higher rutile abundance in the fracture haloes and the leucocratic domains suggest alteration of the granulite by a similar or even the same fluid. This relationship between the presence of the rutile-bearing assemblage and localization of fluid and deformation in the shear zone, producing the leucocratic domains, is summarised schematically in Figure 11a. Since the interlayering and consistent foliation of the amphibolite and the leucocratic domains (Figures 2a and 5a) indicate contemporaneous deformation of both lithologies, hydration is assumed to begin with the breakdown of the diopside in the granulite to form the amphibolite (Figure 11a). Where syn-deformational reaction continues at amphibolite-facies conditions, the rutile-bearing assemblage (tschermakite, clinozoisite, quartz and biotite) dominates.

Following rutile crystallization, large grains underwent crystal-plastic deformation in the presence of fluid (Figures 11a and b). Evidence of element transport associated with crystal-plastic deformation of rutile indicates that syn-tectonic fluid infiltration along fractures initiated the formation of the shear zone. Following initial fluid infiltration, the continuous syn-deformational re-equilibration of the rutile Zr concentrations is evidenced by

the spread of Zr-in-rutile temperatures between 620 to 820°C measured on rutile low-angle boundaries in the leucocratic domains (Figures 9 and 11b).

Rutile lattice deformation concomitant with re-equilibration of U resulted in the observed low concentrations at low angle boundaries (Figure 8a). Since the temperature during deformation was significantly higher than the Pb diffusion closure temperature of approximately 600°C (Cherniak, 2000; Vry & Baker, 2006), it is unlikely that U–Pb in both substructured and substructure-free rutile reached closure until the end of deformation. The 437 ± 2.7 Ma age is therefore interpreted to reflect the minimum age of deformation, recorded in large substructure-free rutile in the leucocratic domains (Figure 11b).

Ages of 455 ± 2 Ma and 439 ± 4 Ma recorded by Ar-Ar in amphibole (Boundy et al., 1996) have previously been interpreted to be erroneous due to possible excess Ar in the amphibole (Kühn et al., 2002; Roffeis et al., 2012). Alternatively, they may also reflect the first stage of fluid infiltration as recorded by rutile in the leucocratic domains. A similar re-interpretation of phengitic muscovite ages in Lindås Nappe eclogites (433 ± 1 to 429 ± 1 ; Boundy et al., 1996) was suggested by Bingen et al. (2004), based on evidence for the retention of radiogenic Ar in phengite in high-pressure environments at relatively high temperatures ($> 500^\circ\text{C}$) (Di Vincenzo, Tonarini, Lombardo, Castelli, & Ottolini, 2006; Giorgis, Cosca, & Li, 2000; Rodriguez, Cosca, Ibarguchi, & Dallmeyer, 2003).

However, the coeval formation of leucocratic domains and amphibolite does not reconcile with the distinct temperature values recorded by rutile from the two lithologies. Zr-in-rutile temperatures range from 640 to 860°C for large substructure-free grains in the leucocratic domains and 610 to 730 °C for the amphibolite (Figures 9a, f). Since a 130 °C temperature gradient over a distance of only 0.5 m appears inconsistent with a regional-scale thermal state, further explanation is required to account for the high temperatures recorded in the shear zone. Three explanations are considered: (1) Zr is undersaturated in the

amphibolite, resulting in an underestimation of the temperature by Zr-in-rutile thermometry for the statically hydrated wall rock of the shear zone; (2) rutile temperatures from the shear zone reflect infiltration of an externally derived high temperature fluid; (3) the high temperatures recorded by rutile from the shear zone reflect rutile formation during shear heating.

In the first explanation, temperature is controlled by the regional thermal state but rutile in the static amphibolite formed in Zr-unsaturated conditions and was therefore unable to reach the equilibrium concentration of Zr consistent with the temperature of formation (Watson et al., 2006). In this scenario, localized flow of Si-Al-Na-bearing fluid within the leucocratic domains facilitates transport of normally immobile elements through the deforming rock volume, thus enhancing the availability of Zr within Si-Al-Na-bearing fluid hosted zones. In contrast to option two, which requires an external fluid for heat input, in this option a hydrous fluid with low thermal mass could infiltrate the rock and produce an internally derived Si-Na-Al-bearing fluid along fractures pathways. The Si-Na-Al-bearing fluid, being of higher viscosity than the hydrous fluid, would be restricted to these fracture pathways, resulting in temperature and consequently textural and mineralogical differences that are coupled to strain variations as observed between the amphibolite and leucocratic domains and localized re-equilibration of trace element concentrations.

The second explanation is that the localized occurrence of high-temperature rutile is due to the channelization of externally derived hot Na-Al-Si-bearing fluid along a deformation-induced high permeability zone (e.g. Daczko, Piazzolo, Meek, Stuart, & Elliott, 2016). Modelling of heat transfer by fluids suggests that conduction or advection of heat requires a large, channelized, continuous flux and/or repeated pulses of high temperature fluid (Bickle & McKenzie, 1987; Brady, 1988; Hoisch, 1991; Thompson & Connolly, 1990). Fluid channelization is consistent with the distribution of leucocratic domains, appearing as

highly localized zones of distinct composition in outcrop and thin section (Figures 2a and 4a). Fluid channelization most effectively occurs under high strain, where the partitioning of strain into discrete zones of deformation couples with fluid-flow (Mancktelow, 2006). To account for the coupling between high strain and fluid flow the initial infiltration must have been syn-tectonic, resulting in localized mechanical weakening and subsequent fluid channelization along optimally orientated pathways. This link between deformation and syn-tectonic fluid channelling has been recently shown to occur in the lower continental crust (Daczko et al., 2016; Meek, Piazzolo, & Daczko, 2019; Stuart, Meek, Daczko, Piazzolo, & Huang, 2018).

In the third option, increased temperature coupled with strain is accounted for by shear heating. Shear heating occurs at relatively high shear stresses (>100 MPa) and strain rates ($10^{-11} - 10^{-12} \text{ s}^{-1}$) (Molnar & England, 1990) and is the result of the conversion of mechanical energy into heat during progressive deformation (Brun & Cobbold, 1980). Temperature increases in shear zones as result of shear heating have been inferred to be in the order of $100 - 200^{\circ}\text{C}$ above ambient conditions (Camacho, McDougall, Armstrong, & Braun, 2001; Whittington, Hofmeister, & Nabelek, 2009). The coincidence here between the deformation zone and higher temperatures (up to $\sim 860^{\circ}\text{C}$; Figures 9 and 11b) is in agreement with these previous estimates. At ambient crustal temperatures exceeding $\sim 600^{\circ}\text{C}$ heat produced by shear heating may be retained due to thermal insulation (Whittington et al., 2009). In fact, thermo-mechanical modelling indicates that during intermittent stress relaxation the shear zone temperature remains elevated and progressively increases toward the peak temperature with successive shear heating events (Kelemen & Hirth, 2007). This is consistent with the range of Zr-in-rutile temperatures recorded in substructure-free areas of deformed porphyroblastic rutile ($620-820^{\circ}\text{C}$; Figures 9e and 11b). In contrast to the second

explanation, Si-Al-Na-bearing fluid is produced internally by dissolution of the rock during deformation.

Based on the data presented in this study none of the above explanations can be excluded with certainty. However, the consistency of temperatures of 610 – 730°C recorded by rutile in the statically hydrated amphibolite with previous estimates of regional peak-metamorphic conditions (~690 °C) of the Bergen Arcs (Bhowany et al., 2018; Boundy et al., 1996; Glodny et al., 2008) supports a scenario where rutile formed above ambient temperature within the shear zone, requiring either shear heating or heat advection through an externally derived fluid. Crystallization ages of 428 ± 8 Ma and 422 ± 17 Ma (Kühn et al., 2002) and a U–Pb zircon age of 424 ± 1 Ma (Jamtveit et al., 2018) for pegmatites within the Lindås Nappe further support the transport of Na-Al-Si-bearing fluids at a time approximate to the amphibolite-facies event. However, whether the emplaced pegmatites are derived externally or from internal reactions remains ambiguous.

5.5.2. Stage 2 – Exhumation to the upper-crust

The 404.8 ± 4.5 Ma and 409.1 ± 2.2 Ma LA-ICP-MS and SHRIMP rutile ages agree with reported Rb-Sr ages of 413 ± 4 Ma (Glodny et al., 2008) and 409 ± 8 Ma (Bingen et al., 2001). These ages are interpreted to record the cessation of diffusional re-equilibration of Pb along low-angle boundaries during exhumation. According to estimated closure temperatures for Pb-loss from rutile, the investigated rocks must have resided at temperatures in the range of ~500-700°C (Cherniak, 2000; Kooijman et al., 2010; Vry & Baker, 2006). Any temperature in excess of this range would have resulted in complete resetting of the substructure-free grains, indicating Pb-loss at mid-crustal temperature conditions for a period of *c.* 30 My following Stage 1 deformation. In addition, the *c.* 410-405 Ma age for exhumation is additionally consistent with $^{40}\text{Ar}/^{39}\text{Ar}$ plateau ages of *c.* 410 Ma from Fossen and Dunlap (1998), interpreted as the last stage of nappe stacking and cooling below ~500°C.

The eventual cessation of Pb-loss at *c.* 410–405 Ma therefore marks the exhumation to upper-crustal conditions where thermally driven Pb loss is no longer operative.

6. CONCLUSIONS/IMPLICATIONS

Rutile from the Bergen Arcs amphibolite-facies shear zone records not only the cooling history of the amphibolites but also the timing and temperature of deformation. Combined microstructural and geochemical analyses of rutile allow a reconstruction of the multi-stage history of the shear zone. While mid-crustal conditions ($\sim 610\text{--}730^\circ\text{C}$) are recorded in the statically hydrated wall rock of the shear zone, syn-tectonically precipitated rutile in the dynamically hydrated shear zone records a localized temperature increase to $\sim 860^\circ\text{C}$. Whether this temperature increase was driven by externally derived high-temperature fluids or by shear heating remains to be investigated. Progressive fluid-assisted deformation resulted in the localized resetting of U–Pb ages and slightly lower Zr-in-rutile temperatures of $\sim 820^\circ\text{C}$ along deformation structures in deformed grains from the shear zone. Finally, crystal-plastic deformation subsides at conditions consistent with the statically hydrated rock ($\sim 560\text{--}670^\circ\text{C}$) accompanied by the formation of small ($< 150\ \mu\text{m}$) rutile in the strained lithologies. This is estimated to be concomitant with the cessation of U mobility along low-angle boundaries at $437.4 \pm 2.7\ \text{Ma}$. The final closure of Pb diffusion from rutile is recorded at *c.* 410–405 Ma, indicating that the rocks remained at mid-crustal conditions ($\sim 500\text{--}700^\circ\text{C}$) during the interim period.

Our findings indicate that U–Pb ages and trace element concentrations in rutile may be strongly dependent on microstructure. In this particular instance both U–Pb and Zr-in-rutile show systematic changes with crystal-lattice distortion. Young ages are consistently correlated with significant crystal-plastic deformation and low-angle boundaries have lower Zr concentrations than substructure-free domains in rutile. Low-angle boundaries are therefore proposed to act as fast diffusion pathways in rutile, allowing for enhanced element

mobility. Therefore, in instances where the trace element distribution and U–Pb ratios are controlled by fast diffusion due to deformation, rutile can be a useful tool for constraining a near complete deformation and cooling history of the rock.

ACKNOWLEDGEMENTS

The review of an earlier version of this manuscript by Klaus Mezger is gratefully acknowledged. This paper has benefited from the constructive reviews of Andrew Kylander-Clark and Thomas Zack in addition to editorial handling by Richard White. This research was funded by the Australian Research Council Discovery Project of Putnis, Raimondo, and Daczko (ARC grant number DP160103449). The authors acknowledge the facilities, and the scientific and technical assistance of the Australian Microscopy and Microanalysis Research Facility at the Centre for Microscopy, Characterisation and Analysis, The University of Western Australia, a facility funded by the University, State and Commonwealth Governments. Part of this research was undertaken using the EM instrumentation (ARC LE130100053) at the John de Laeter Centre, Curtin University.

REFERENCES

- Antignano, A., & Manning, C. E. (2008). Rutile solubility in H₂O, H₂O–SiO₂, and H₂O–NaAlSi₃O₈ fluids at 0.7–2.0 GPa and 700–1000 C: implications for mobility of nominally insoluble elements. *Chemical Geology*, 255(1-2), 283-293.
- Ashbee, K., & Smallman, R. E. (1963). The plastic deformation of titanium dioxide single crystals. *Proc. R. Soc. Lond. A*, 274(1357), 195-205.
- Austrheim, H. (1987). Eclogitization of lower crustal granulites by fluid migration through shear zones. *Earth and Planetary Science Letters*, 81(2-3), 221-232.
- Austrheim, H. (1990). *Fluid induced processes in the lower crust as evidenced by Caledonian eclogitization of Precambrian granulites, Bergen Arcs, western-Norway*.
- Austrheim, H., & Robins, B. (1981). Reactions involving hydration of orthopyroxene in anorthosite-gabbro. *Lithos*, 14(4), 275-281.
- [http://dx.doi.org/https://doi.org/10.1016/0024-4937\(81\)90055-4](http://dx.doi.org/https://doi.org/10.1016/0024-4937(81)90055-4)

829 Axelsson, E., Pape, J., Berndt, J., Corfu, F., Mezger, K., & Raith, M. M. (2018). Rutile
 830 R632–A New Natural Reference Material for U-Pb and Zr Determination.
 831 *Geostandards and Geoanalytical Research*, 42(3), 319-338.

832 Bestmann, M., & Prior, D. J. (2003). Intragranular dynamic recrystallization in naturally
 833 deformed calcite marble: diffusion accommodated grain boundary sliding as a result
 834 of subgrain rotation recrystallization. *Journal of Structural Geology*, 25(10), 1597-
 835 1613.

836 Bhowany, K., Hand, M., Clark, C., Kelsey, D., Reddy, S., Pearce, M., . . . Morrissey, L.
 837 (2018). Phase equilibria modelling constraints on P–T conditions during fluid
 838 catalysed conversion of granulite to eclogite in the Bergen Arcs, Norway. *Journal of*
 839 *Metamorphic Geology*, 36(3), 315-342.

840 Bickle, M., & McKenzie, D. (1987). The transport of heat and matter by fluids during
 841 metamorphism. *Contributions to Mineralogy and Petrology*, 95(3), 384-392.

842 Bingen, B., Austrheim, H., Whitehouse, M. J., & Davis, W. J. (2004). Trace element
 843 signature and U–Pb geochronology of eclogite-facies zircon, Bergen Arcs,
 844 Caledonides of W Norway. *Contributions to Mineralogy and Petrology*, 147(6), 671-
 845 683.

846 Bingen, B., Davis, W. J., & Austrheim, H. (2001). Zircon U-Pb geochronology in the Bergen
 847 arc eclogites and their Proterozoic protoliths, and implications for the pre-Scandian
 848 evolution of the Caledonides in western Norway. *Geological Society of America*
 849 *Bulletin*, 113(5), 640-649.

850 Blanchin, M., Bursill, L., & Lafage, C. (1990). Deformation and microstructure of rutile.
 851 *Proc. R. Soc. Lond. A*, 429(1876), 175-202.

852 Blundy, J. D., & Holland, T. J. (1990). Calcic amphibole equilibria and a new amphibole-
 853 plagioclase geothermometer. *Contributions to mineralogy and petrology*, 104(2), 208-
 854 224.

855 Bohlen, S. R., & Liotta, J. J. (1986). A barometer for garnet amphibolites and garnet
 856 granulites. *Journal of Petrology*, 27(5), 1025-1034.

857 Boundy, T. M., Essene, E. J., Hall, C. M., Austrheim, H., & Halliday, A. (1996). Rapid
 858 exhumation of lower crust during continent-continent collision and late extension:
 859 Evidence from $^{40}\text{Ar}/^{39}\text{Ar}$ incremental heating of hornblendes and muscovites,

860 Caledonian orogen, western Norway. *Geological Society of America Bulletin*,
861 108(11), 1425-1437.

862 Boundy, T. M., Mezger, K., & Essene, E. J. (1997). Temporal and tectonic evolution of the
863 granulite-eclogite association from the Bergen Arcs, western Norway. *Lithos*, 39(3-4),
864 159-178.

865 Bracciali, L., Parrish, R. R., Horstwood, M. S., Condon, D. J., & Najman, Y. (2013). UPb
866 LA-(MC)-ICP-MS dating of rutile: New reference materials and applications to
867 sedimentary provenance. *Chemical Geology*, 347, 82-101.

868 Brady, J. B. (1988). The role of volatiles in the thermal history of metamorphic terranes.
869 *Journal of Petrology*, 29(6), 1187-1213.

870 Brun, J., & Cobbold, P. (1980). Strain heating and thermal softening in continental shear
871 zones: a review. *Journal of Structural Geology*, 2(1-2), 149-158.

872 Bureau, H., & Keppler, H. (1999). Complete miscibility between silicate melts and hydrous
873 fluids in the upper mantle: experimental evidence and geochemical implications.
874 *Earth and Planetary Science Letters*, 165(2), 187-196.

875 Büttner, S. H., & Kasemann, S. A. (2007). Deformation-controlled cation diffusion in
876 tourmaline: A microanalytical study on trace elements and boron isotopes. *American*
877 *Mineralogist*, 92(11-12), 1862-1874.

878 Camacho, A., McDougall, I., Armstrong, R., & Braun, J. (2001). Evidence for shear heating,
879 Musgrave Block, central Australia. *Journal of Structural Geology*, 23(6-7), 1007-
880 1013.

881 Centrella, S., Austrheim, H., & Putnis, A. (2015). Coupled mass transfer through a fluid
882 phase and volume preservation during the hydration of granulite: An example from
883 the Bergen Arcs, Norway. *Lithos*, 236, 245-255.

884 Chapman, T., Clarke, G. L., Piazzolo, S., Robbins, V. A., & Trimby, P. W. Grain-scale
885 dependency of metamorphic reaction on crystal plastic strain. *Journal of*
886 *Metamorphic Geology*, 0(ja) <http://dx.doi.org/doi:10.1111/jmg.12473>

887 Chapman, T., Clarke, G. L., Piazzolo, S., Robbins, V. A., & Trimby, P. W. (2019). Grain-scale
888 dependency of metamorphic reaction on crystal plastic strain. *Journal of*
889 *Metamorphic Geology*,

890 Cherniak, D. (2000). Pb diffusion in rutile. *Contributions to Mineralogy and Petrology*,
891 139(2), 198-207.

892 Cherniak, D., Manchester, J., & Watson, E. (2007). Zr and Hf diffusion in rutile. *Earth and*
893 *Planetary Science Letters*, 261(1-2), 267-279.

894 Clark, D., Hensen, B., & Kinny, P. (2000). Geochronological constraints for a two-stage
895 history of the Albany–Fraser Orogen, Western Australia. *Precambrian Research*,
896 102(3-4), 155-183.

897 Cohen, A., O'nions, R., Siegenthaler, R., & Griffin, W. (1988). Chronology of the pressure-
898 temperature history recorded by a granulite terrain. *Contributions to Mineralogy and*
899 *Petrology*, 98(3), 303-311.

900 Compston, W., Williams, I., & Meyer, C. (1984). U-Pb geochronology of zircons from lunar
901 breccia 73217 using a sensitive high mass-resolution ion microprobe. *Journal of*
902 *Geophysical Research: Solid Earth*, 89(S02), B525-B534.

903 Daczko, N. R., Piazzolo, S., Meek, U., Stuart, C. A., & Elliott, V. (2016). Hornblendite
904 delineates zones of mass transfer through the lower crust. *Scientific reports*, 6, 31369.

905 Di Vincenzo, G., Tonarini, S., Lombardo, B., Castelli, D., & Ottolini, L. (2006). Comparison
906 of ^{40}Ar – ^{39}Ar and Rb–Sr data on phengites from the UHP Brossasco–Isasca Unit
907 (Dora Maira Massif, Italy): implications for dating white mica. *Journal of Petrology*,
908 47(7), 1439-1465.

909 Dodson, M. (1986). *Closure profiles in cooling systems*. Paper presented at the Materials
910 Science Forum

911 Dodson, M. H. (1973). Closure temperature in cooling geochronological and petrological
912 systems. *Contributions to Mineralogy and Petrology*, 40(3), 259-274.

913 Dowty, E. (1980). Crystal-chemical factors affecting the mobility of ions in minerals.
914 *American Mineralogist*, 65(1-2), 174-182.

915 Ewing, T. A. (2011). Hf isotope analysis and U-Pb geochronology of rutile: technique
916 development and application to a lower crustal section (Ivrea-Verbano Zone, Italy).

917 Ewing, T. A., Hermann, J., & Rubatto, D. (2013). The robustness of the Zr-in-rutile and Ti-
918 in-zircon thermometers during high-temperature metamorphism (Ivrea-Verbano Zone,
919 northern Italy). *Contributions to Mineralogy and Petrology*, 165(4), 757-779.
920 <http://dx.doi.org/10.1007/s00410-012-0834-5>

921 Ewing, T. A., Rubatto, D., Beltrando, M., & Hermann, J. (2015). Constraints on the thermal
922 evolution of the Adriatic margin during Jurassic continental break-up: U–Pb dating of

923 rutile from the Ivrea–Verbano Zone, Italy. *Contributions to mineralogy and*
924 *petrology*, 169(4), 44.

925 Flowers, R., Bowring, S., Tulloch, A., & Klepeis, K. (2005). Tempo of burial and
926 exhumation within the deep roots of a magmatic arc, Fiordland, New Zealand.
927 *Geology*, 33(1), 17-20.

928 Fortier, S. M., & Giletti, B. J. (1989). An empirical model for predicting diffusion
929 coefficients in silicate minerals. *Science*, 245(4925), 1481-1484.

930 Fossen, H., & Dunlap, W. J. (1998). Timing and kinematics of Caledonian thrusting and
931 extensional collapse, southern Norway: evidence from $^{40}\text{Ar}/^{39}\text{Ar}$ thermochronology.
932 *Journal of Structural Geology*, 20(6), 765-781.
933 [http://dx.doi.org/https://doi.org/10.1016/S0191-8141\(98\)00007-8](http://dx.doi.org/https://doi.org/10.1016/S0191-8141(98)00007-8)

934 Galbraith, R. (1988). Graphical display of estimates having differing standard errors.
935 *Technometrics*, 30(3), 271-281.

936 Galbraith, R. F. (1990). The radial plot: graphical assessment of spread in ages. *International*
937 *Journal of Radiation Applications and Instrumentation. Part D. Nuclear Tracks and*
938 *Radiation Measurements*, 17(3), 207-214.

939 Ganguly, J., & Tirone, M. (1999). Diffusion closure temperature and age of a mineral with
940 arbitrary extent of diffusion: theoretical formulation and applications. *Earth and*
941 *Planetary Science Letters*, 170(1-2), 131-140.

942 Gao, J., John, T., Klemm, R., & Xiong, X. (2007). Mobilization of Ti–Nb–Ta during
943 subduction: evidence from rutile-bearing dehydration segregations and veins hosted in
944 eclogite, Tianshan, NW China. *Geochimica et Cosmochimica Acta*, 71(20), 4974-
945 4996.

946 Giorgis, D., Cosca, M., & Li, S. (2000). Distribution and significance of extraneous argon in
947 UHP eclogite (Sulu terrain, China): insight from in situ $^{40}\text{Ar}/^{39}\text{Ar}$ UV-laser ablation
948 analysis. *Earth and Planetary Science Letters*, 181(4), 605-615.

949 Glodny, J., Kühn, A., & Austrheim, H. (2002). Rb/Sr record of fluid-rock interaction in
950 eclogites, Bergen Arcs, Norway. *Geochimica et Cosmochimica Acta*, 66(15 A), A280-
951 A280.

952 Glodny, J., Kühn, A., & Austrheim, H. (2008). Geochronology of fluid-induced eclogite and
953 amphibolite facies metamorphic reactions in a subduction–collision system, Bergen
954 Arcs, Norway. *Contributions to Mineralogy and Petrology*, 156(1), 27-48.

955 Graham, C. M., & Powell, R. (1984). A garnet–hornblende geothermometer: calibration,
 956 testing, and application to the Pelona Schist, Southern California. *Journal of*
 957 *metamorphic Geology*, 2(1), 13-31.

958 Griffin, W. (2008). GLITTER: data reduction software for laser ablation ICP-MS. *Laser*
 959 *Ablation ICP-MS in the Earth Sciences: Current practices and outstanding issues*,
 960 308-311.

961 Harley, S. (2008). Refining the P–T records of UHT crustal metamorphism. *Journal of*
 962 *metamorphic Geology*, 26(2), 125-154.

963 Hermann, J., Spandler, C., Hack, A., & Korsakov, A. V. (2006). Aqueous fluids and hydrous
 964 melts in high-pressure and ultra-high pressure rocks: implications for element transfer
 965 in subduction zones. *Lithos*, 92(3-4), 399-417.

966 Hirdes, W., & Davis, D. W. (2002). U–Pb zircon and rutile metamorphic ages of Dahomeyan
 967 garnet-hornblende gneiss in southeastern Ghana, West Africa. *Journal of African*
 968 *Earth Sciences*, 35(3), 445-449.

969 Hirthe, W. M., & Brittain, J. O. (1963). High-Temperature Steady-State Creep in Rutile.
 970 *Journal Of The American Ceramic Society*, 46(9), 411-417.

971 Hoisch, T. D. (1991). The thermal effects of pervasive and channelized fluid flow in the deep
 972 crust. *The Journal of Geology*, 99(1), 69-80.

973 Jamtveit, B., Bucher-Nurminen, K., & Austrheim, H. (1990). Fluid controlled eclogitization
 974 of granulites in deep crustal shear zones, Bergen arcs, Western Norway. *Contributions*
 975 *to Mineralogy and Petrology*, 104(2), 184-193.

976 Jamtveit, B., Moulas, E., Andersen, T. B., Austrheim, H., Corfu, F., Petley-Ragan, A., &
 977 Schmalholz, S. M. (2018). High Pressure Metamorphism Caused by Fluid Induced
 978 Weakening of Deep Continental Crust. *Scientific Reports*, 8(1), 17011.
 979 <http://dx.doi.org/10.1038/s41598-018-35200-1>

980 Jochum, K. P., Nohl, U., Herwig, K., Lammel, E., Stoll, B., & Hofmann, A. W. (2005).
 981 GeoReM: a new geochemical database for reference materials and isotopic standards.
 982 *Geostandards and Geoanalytical Research*, 29(3), 333-338.

983 John, T., Klemd, R., Gao, J., & Garbe-Schönberg, C.-D. (2008). Trace-element mobilization
 984 in slabs due to non steady-state fluid–rock interaction: constraints from an eclogite-
 985 facies transport vein in blueschist (Tianshan, China). *Lithos*, 103(1-2), 1-24.

- 986 Johnson, M. C., & Rutherford, M. J. (1989). Experimental calibration of the aluminum-in-
 987 hornblende geobarometer with application to Long Valley caldera (California)
 988 volcanic rocks. *Geology*, 17(9), 837-841.
- 989 Kelemen, P. B., & Hirth, G. (2007). A periodic shear-heating mechanism for intermediate-
 990 depth earthquakes in the mantle. *Nature*, 446(7137), 787.
- 991 Klemme, S., Prowatke, S., Münker, C., Magee, C. W., Lahaye, Y., Zack, T., . . . Kaeser, B.
 992 (2008). Synthesis and preliminary characterisation of new silicate, phosphate and
 993 titanite reference glasses. *Geostandards and Geoanalytical Research*, 32(1), 39-54.
- 994 Kooijman, E., Berndt, J., & Mezger, K. (2012). U-Pb dating of zircon by laser ablation ICP-
 995 MS: recent improvements and new insights. *European Journal of Mineralogy*, 24(1),
 996 5-21.
- 997 Kooijman, E., Mezger, K., & Berndt, J. (2010). Constraints on the U-Pb systematics of
 998 metamorphic rutile from in situ LA-ICP-MS analysis. *Earth and Planetary Science*
 999 *Letters*, 293(3-4), 321-330.
- 1000 Kooijman, E., Smit, M., Mezger, K., & Berndt, J. (2012). Trace element systematics in
 1001 granulite facies rutile: implications for Zr geothermometry and provenance studies.
 1002 *Journal of Metamorphic Geology*, 30(4), 397-412.
- 1003 Kramer, M. J., & Seifert, K. E. (1991). Strain enhanced diffusion in feldspars *Diffusion,*
 1004 *atomic ordering, and mass transport* (pp. 286-303): Springer.
- 1005 Kühn, A., Glodny, J., Austrheim, H., & Råheim, A. (2002). The Caledonian tectono-
 1006 metamorphic evolution of the Lindås Nappe: Constraints from U-Pb, Sm-Nd and Rb-
 1007 Sr ages of granitoid dykes. *Norwegian Journal of Geology/Norsk Geologisk Forening*,
 1008 82(1)
- 1009 Kylander-Clark, A., Hacker, B., & Mattinson, J. (2008). Slow exhumation of UHP terranes:
 1010 titanite and rutile ages of the Western Gneiss Region, Norway. *Earth and Planetary*
 1011 *Science Letters*, 272(3-4), 531-540.
- 1012 Lund, M. D., Piazzolo, S., & Harley, S. L. (2006). Ultrahigh temperature deformation
 1013 microstructures in felsic granulites of the Napier Complex, Antarctica.
 1014 *Tectonophysics*, 427(1-4), 133-151.
- 1015 Luvizotto, G., & Zack, T. (2009). Nb and Zr behavior in rutile during high-grade
 1016 metamorphism and retrogression: an example from the Ivrea-Verbano Zone.
 1017 *Chemical Geology*, 261(3-4), 303-317.

1018 Luvizotto, G., Zack, T., Meyer, H., Ludwig, T., Triebold, S., Kronz, A., . . . Klemme, S.
1019 (2009). Rutile crystals as potential trace element and isotope mineral standards for
1020 microanalysis. *Chemical Geology*, 261(3-4), 346-369.

1021 Mancktelow, N. S. (2006). How ductile are ductile shear zones? *Geology*, 34(5), 345-348.

1022 Manning, C. E. (2004). The chemistry of subduction-zone fluids. *Earth and Planetary
1023 Science Letters*, 223(1-2), 1-16.

1024 Meek, U., Piazzolo, S., & Daczko, N. R. (2019). The field and microstructural signatures of
1025 deformation-assisted melt transfer: Insights from magmatic arc lower crust, New
1026 Zealand. *Journal of Metamorphic Geology*,

1027 Meyer, M., John, T., Brandt, S., & Klemd, R. (2011). Trace element composition of rutile
1028 and the application of Zr-in-rutile thermometry to UHT metamorphism (Epupa
1029 Complex, NW Namibia). *Lithos*, 126(3-4), 388-401.

1030 Mezger, K., Hanson, G., & Bohlen, S. (1989). High-precision UPb ages of metamorphic
1031 rutile: application to the cooling history of high-grade terranes. *Earth and Planetary
1032 Science Letters*, 96(1-2), 106-118.

1033 Mitchell, R. J., & Harley, S. L. (2017). Zr-in-rutile resetting in aluminosilicate bearing ultra-
1034 high temperature granulites: Refining the record of cooling and hydration in the
1035 Napier Complex, Antarctica. *Lithos*, 272, 128-146.

1036 Molnar, P., & England, P. (1990). Temperatures, heat flux, and frictional stress near major
1037 thrust faults. *Journal of Geophysical Research: Solid Earth*, 95(B4), 4833-4856.

1038 Moore, J., Beinlich, A., Austrheim, H., & Putnis, A. (2019). Stress orientation-dependent
1039 reactions during metamorphism. *Geology*,

1040 Pape, J., Mezger, K., & Robyr, M. (2016). A systematic evaluation of the Zr-in-rutile
1041 thermometer in ultra-high temperature (UHT) rocks. *Contributions to mineralogy and
1042 petrology*, 171(5), 44.

1043 Piazzolo, S., Austrheim, H., & Whitehouse, M. (2012). Brittle-ductile microfabrics in naturally
1044 deformed zircon: Deformation mechanisms and consequences for U-Pb dating.
1045 *American Mineralogist*, 97(10), 1544-1563.

1046 Piazzolo, S., Bestmann, M., Prior, D., & Spiers, C. (2006). Temperature dependent grain
1047 boundary migration in deformed-then-annealed material: observations from
1048 experimentally deformed synthetic rocksalt. *Tectonophysics*, 427(1), 55-71.

1049 Piazzolo, S., La Fontaine, A., Trimby, P., Harley, S., Yang, L., Armstrong, R., & Cairney, J.
1050 M. (2016). Deformation-induced trace element redistribution in zircon revealed using
1051 atom probe tomography. *Nature communications*, 7, 10490.

1052 Plavsa, D., Reddy, S. M., Agangi, A., Clark, C., Kylander-Clark, A., & Tiddy, C. J. (2018).
1053 Microstructural, trace element and geochronological characterization of TiO₂
1054 polymorphs and implications for mineral exploration. *Chemical Geology*, 476, 130-
1055 149.

1056 Plümper, O., King, H. E., Vollmer, C., Ramasse, Q., Jung, H., & Austrheim, H. (2012). The
1057 legacy of crystal-plastic deformation in olivine: high-diffusivity pathways during
1058 serpentinization. *Contributions to Mineralogy and Petrology*, 163(4), 701-724.

1059 Prior, D. J., Wheeler, J., Peruzzo, L., Spiess, R., & Storey, C. (2002). Some garnet
1060 microstructures: an illustration of the potential of orientation maps and misorientation
1061 analysis in microstructural studies. *Journal of Structural Geology*, 24(6), 999-1011.

1062 Puelles, P., Beranoaguirre, A., Ábalos, B., Gil Ibarguchi, J., García de Madinabeitia, S.,
1063 Rodríguez, J., & Fernández-Armas, S. (2017). Eclogite inclusions from subducted
1064 metaigneous continental crust (Malpica-Tui Allochthonous Complex, NW Spain):
1065 Petrofabric, geochronology, and calculated seismic properties. *Tectonics*, 36(7), 1376-
1066 1406.

1067 Rapp, J., Klemme, S., Butler, I., & Harley, S. (2010). Extremely high solubility of rutile in
1068 chloride and fluoride-bearing metamorphic fluids: An experimental investigation.
1069 *Geology*, 38(4), 323-326.

1070 Reddy, S. M., Timms, N. E., Pantleon, W., & Trimby, P. (2007). Quantitative
1071 characterization of plastic deformation of zircon and geological implications.
1072 *Contributions to Mineralogy and Petrology*, 153(6), 625-645.

1073 Rodriguez, J., Cosca, M., Ibarguchi, J. G., & Dallmeyer, R. (2003). Strain partitioning and
1074 preservation of ⁴⁰Ar/³⁹Ar ages during Variscan exhumation of a subducted crust
1075 (Malpica–Tui complex, NW Spain). *Lithos*, 70(3-4), 111-139.

1076 Roffeis, C., Corfu, F., & Austrheim, H. (2012). Evidence for a Caledonian amphibolite to
1077 eclogite facies pressure gradient in the Middle Allochthon Lindås Nappe, SW-
1078 Norway. *Contributions to Mineralogy and Petrology*, 164(1), 81-99.

1079 Schmidt, M. (1991). *Experimental calibration of the Al-in-hornblende geobarometer at 650*
1080 *C, 3.5-13.0 kbar*. Paper presented at the Terra abstr

1081 Stacey, J. t., & Kramers, J. (1975). Approximation of terrestrial lead isotope evolution by a
 1082 two-stage model. *Earth and planetary science letters*, 26(2), 207-221.

1083 Stuart, C., Meek, U., Daczko, N., Piazzolo, S., & Huang, J.-X. (2018). chemical signatures of
 1084 melt–rock interaction in the root of a magmatic arc. *Journal of Petrology*, 59(2), 321-
 1085 340.

1086 Thompson, A. B., & Connolly, J. (1990). Metamorphic fluids and anomalous porosities in the
 1087 lower crust. *Tectonophysics*, 182(1-2), 47-55.

1088 Timms, N. E., Kinny, P. D., Reddy, S. M., Evans, K., Clark, C., & Healy, D. (2011).
 1089 Relationship among titanium, rare earth elements, U–Pb ages and deformation
 1090 microstructures in zircon: Implications for Ti-in-zircon thermometry. *Chemical*
 1091 *Geology*, 280(1-2), 33-46.

1092 Timms, N. E., Reddy, S. M., Gerald, J. D. F., Green, L., & Muhling, J. R. (2012). Inclusion-
 1093 localised crystal-plasticity, dynamic porosity, and fast-diffusion pathway generation
 1094 in zircon. *Journal of Structural Geology*, 35, 78-89.

1095 Tomkins, H., Powell, R., & Ellis, D. (2007). The pressure dependence of the zirconium-in-
 1096 rutile thermometer. *Journal of metamorphic Geology*, 25(6), 703-713.

1097 Vermeesch, P. (2018). IsoplotR: A free and open toolbox for geochronology. *Geoscience*
 1098 *Frontiers*,

1099 Vry, J. K., & Baker, J. A. (2006). LA-MC-ICPMS Pb–Pb dating of rutile from slowly cooled
 1100 granulites: confirmation of the high closure temperature for Pb diffusion in rutile.
 1101 *Geochimica et Cosmochimica Acta*, 70(7), 1807-1820.

1102 Watson, E., Wark, D., & Thomas, J. (2006). Crystallization thermometers for zircon and
 1103 rutile. *Contributions to Mineralogy and Petrology*, 151(4), 413.

1104 Whitney, D. L., & Evans, B. W. (2010). Abbreviations for names of rock-forming minerals.
 1105 *American mineralogist*, 95(1), 185.

1106 Whittington, A. G., Hofmeister, A. M., & Nabelek, P. I. (2009). Temperature-dependent
 1107 thermal diffusivity of the Earth’s crust and implications for magmatism. *Nature*, 458,
 1108 319. <http://dx.doi.org/10.1038/nature07818>

1109 Williams, I. S. (1998). U-Th-Pb geochronology by ion microprobe. *Reviews in Economic*
 1110 *Geology*, 7, 1-35.

1111 Yund, R., Smith, B., & Tullis, J. (1981). Dislocation-assisted diffusion of oxygen in albite.
 1112 *Physics and Chemistry of Minerals*, 7(4), 185-189.

- 1113 Yund, R. A., & Tullis, J. (1980). The effect of water, pressure, and strain on Al/Si order-
 1114 disorder kinetics in feldspar. *Contributions to Mineralogy and Petrology*, 72(3), 297-
 1115 302.
- 1116 Zack, T., & Kooijman, E. (2017). Petrology and geochronology of rutile. *Reviews in*
 1117 *Mineralogy and Geochemistry*, 83(1), 443-467.
- 1118 Zack, T., Moraes, R., & Kronz, A. (2004). Temperature dependence of Zr in rutile: empirical
 1119 calibration of a rutile thermometer. *Contributions to Mineralogy and Petrology*,
 1120 148(4), 471-488.
- 1121 Zack, T., Stockli, D. F., Luvizotto, G. L., Barth, M. G., Belousova, E., Wolfe, M. R., &
 1122 Hinton, R. W. (2011). In situ U–Pb rutile dating by LA-ICP-MS: 208 Pb correction
 1123 and prospects for geological applications. *Contributions to Mineralogy and Petrology*,
 1124 162(3), 515-530.
- 1125 Zeh, A., Cabral, A. R., Koglin, N., & Decker, M. (2018). Rutile alteration and authigenic
 1126 growth in metasandstones of the Moeda Formation, Minas Gerais, Brazil—A result of
 1127 Transamazonian fluid–rock interaction. *Chemical Geology*, 483, 397-409.

1128 **LIST OF SUPPORTING INFORMATION**

1129 Supporting information is in the form of data tables and can be found in the document
 1130 Supdataset.xlsx. The data tables provided are as follows:

- 1131 - Figure S1 – c-axis orientation of large rutile
- 1132 - Table S1 – Representative amphibole
- 1133 - Table S2 – LA-ICP-MS trace element
- 1134 - Table S3 – EMPA Major and trace element
- 1135 - Table S4a – LA-ICP-MS U-Pb
- 1136 - Table S4b – SHRIMP U-Pb

1137 **FIGURE CAPTIONS**

1138 **FIGURE 1** – (a) Regional setting of study area at Radøy in the Lindås Nappe of the Bergen
 1139 Arcs, Western Norway. The outcrop locality is indicated by the white star. The locality of

amphibolite-facies samples collected for age data and P-T estimates by previous workers are annotated on the map with symbols corresponding to those used in (b) and numbered according to the references listed below. MCTZ = Main Caledonian Thrust Zone. BASZ = Bergen Arcs Shear Zone. Modified from Boundy, Mezger, and Essene (1997), Glodny et al. (2008) and Centrella, Austrheim, and Putnis (2015). (b) Summary of previous geochronological work for Caledonian age events affecting the Lindås Nappe. Amphibolite zircon U–Pb data are from ¹Kühn et al. (2002), ²Roffeis et al. (2012), ³Piazolo et al. (2012), and ⁴Glodny et al. (2008). Multi-mineral Rb-Sr and Sm-Nd data for amphibolites are from ⁵Glodny, Kühn, and Austrheim (2002), ⁴Glodny et al. (2008) and ⁸Austrheim (1990). Amphibole and white mica Ar-Ar data are from ⁶Boundy et al. (1996), biotite Ar-Ar data are from ⁷Fossen and Dunlap (1998). Rb-Sr and Sm-Nd Pegmatite ages were determined by ¹Kühn et al. (2002) and the U–Pb zircon age is from ⁹Jamtveit et al. (2018). Eclogite U–Pb data are from the following sources: U–Pb zircon (Bingen et al., 2004; Bingen et al., 2001; Glodny et al., 2008), titanite-epidote-zircon U–Pb (Boundy et al., 1997). Error bars represent 2σ uncertainty.

FIGURE 2 – Lithological relationships in outcrop. (a) The porphyroblastic rutile-bearing lithology, the leucocratic domains, are observed interlayered with the amphibolite in the shear zone. (b) Fracture type-I and type-II in the granulite in outcrop. Sample locations are indicated by red boxes, annotated with image figure numbers.

FIGURE 3 – Photomicrographs of the main lithologies (a) granulite (b) amphibolite, here incompletely reacted, (c) strained amphibolite and (d) the shear zone rock comprised of the amphibolite interlayered with leucocratic domains. Scale bar is 5 mm.

FIGURE 4 – Rutile occurrence in amphibolite and in association with fracture haloes in the granulite. (a) Fracture type-I, hosting quartz and tschermakite, crosscutting horizontal foliation in partially replaced granulite. BSE images (b-f) showing (b) rutile needles in

1165 amphibole clusters in the amphibolite (c) rutile associated with both amphibole clusters and
1166 biotite and clinozoisite in the strained amphibolite (d) rutile in amphibole clusters in
1167 alteration halo of fracture type-I, and, (e) rutile forming in a symplectitic assemblage of
1168 magnesio-hornblende quartz and zoisite replacing diopside on the edge of the fracture type-I
1169 alteration halo. (f) Rutile in a clinozoisite and pargasite filled fracture in diopside, occurring
1170 in the alteration halo of fracture type-II.

1171 **FIGURE 5** - Rutile distribution in leucocratic domains, interlayered with strained
1172 amphibolite in the shear zone. (a) Photograph of sample showing the location of
1173 microtextural analyses. Note the bottom to top increase in the proportion of the leucocratic
1174 component. BSE images (b-f) illustrate the mineralogical changes with increased leucocratic
1175 component. (f) Original amphibole clusters display a lower abundance of rutile and biotite
1176 then (d) amphibole clusters interlayered with the leucocratic component. Porphyroblastic
1177 rutiles are apparent in both (b) the mafic (c) and plagioclase dominated components of the
1178 leucocratic vein. Within leucocratic domains porphyroblastic clinozoisite and biotite form in
1179 (b) foliation parallel mafic clusters and in (e) foliation parallel bands. All images are aligned
1180 with the S foliation parallel to that shown in (a).

1181 **FIGURE 6** – Microstructures of substructure-free rutile associated with leucocratic domains;
1182 rutiles are characterized by low GOS ($< 1^\circ$) and lack of subgrain boundaries; (a-d) EBSD
1183 phase maps with grain, subgrain and twin boundaries in rutile show (a, c) grain morphology
1184 and phase associations of large substructure- free grains in both the plagioclase dominated
1185 leucocratic domain and, (b) in the preserved amphibole banding, as well as, (d) small
1186 substructure-free grains in the extensional veinlets. GOS: Grain orientation spread ($^\circ$). Grain
1187 numbering applies to grains with reported U–Pb data (see Table S4).

1188 **FIGURE 7** – Microstructures of large substructured rutile grains in the leucocratic domains.
1189 For visualisation of substructures, representative large substructured grains are presented as

EBSD maps showing the deviation of each pixel from the mean orientation of the grain (a, e & h). Presented here are grains showing (a) shear bands, (e) lamellar subgrain boundaries and (h) low-angle boundaries related to twinning at grain edges. Lower hemisphere equal area plots (b, f, & i) exhibit disorientation axes relative to the crystallographic directions. (b) disorientation axes for the entire grain shown in (a); (f and i) disorientation axes for selected areas in (e) and (h) that are outlined by stippled boxes. For (a) the shear band the (b) disorientation axes cluster on the $\langle 112 \rangle$ axis but show no correlation with known slip systems while for (f) disorientation axes plot at $\langle 110 \rangle$, consistent with operation of the $\langle 001 \rangle \{110\}$ slip system and (i) and at $\langle 100 \rangle$ consistent with the $\{101\} \langle -101 \rangle$ slip system. Plotted grain orientation axes (c), coloured according to the misorientation in the EBSD map, further exhibit that the principal rotation axis for the sheared grain is $\sim \langle 112 \rangle$. Cumulative misorientation profile (d, g) showing the misorientation across the subgrain boundaries associated with the shear band (d) and the lamellar subgrain boundaries (g). GOS: Grain orientation spread ($^\circ$). Grain numbering applies to grains with reported U–Pb data (see Table S4).

FIGURE 8 – LA-ICP-MS trace element spot analyses plotted by distance from grain boundary. Individual analyses are coloured to represent the grain structure of the analysis spot. Shaded grey areas indicate the spread of the data from low-angle boundaries (LAB) (darker) and substructure free grains (lighter). The weighted average concentration for trace elements measured from substructure free spots within 80 μm of the grain boundary in large grains (grey stippled line) is compared to the weighted average value of spots containing low-angle boundaries (cyan stippled lines). Dotted lines represent the mean 2σ uncertainty.

FIGURE 9 - Frequency histograms displaying Zr-in-rutile temperature estimates for individual EMP and LA-ICP-MS analyses in all lithologies (a-f).

FIGURE 10 - U–Pb data for porphyroblastic rutile in leucocratic domains obtained via LA-ICP-MS (a, c, and e) and SHRIMP (b, d, and f) analysis. (a, b) U–Pb concordia diagrams, ellipses representing the 2-sigma uncertainty. (c, d) Weighted mean age of individual analyses. (e, f) Radial plot exhibiting dispersion of U–Pb ages, coloured according to GOS; for graphical method see Galbraith (1988); Galbraith (1990). The grey coloured analyses in (f) represent a grain with no corresponding EBSD data. In weighted mean and radial plots data are restricted to analyses within 5% discordance, eliminating 4 of the LA-ICP-MS analyses.

FIGURE 11 - Characteristic textural setting of rutile in each lithology, showing correlation between rutile growth, recorded temperature and strain. (a) Schematic illustration of (i) the microstructure of rutile in the amphibolite where it forms as part of a symplectitic assemblage replacing diopside, (ii) rutile in strained and shear zone amphibolite where it occurs with biotite and quartz in amphibole and (iii) large and small rutile replacing amphibole in the leucocratic domains of the shear zone due to increasing deformation and reaction. (b) Schematic of deformation microstructures in large rutile in the leucocratic domains and box plots showing the corresponding spread in Zr-in-rutile temperatures for microstructures and small grains.

(a)

Amphibolite^{3,2}
♦ 437 ± 11
♦ 426 ± 4

Pegmatite¹
● 422 ± 17
■ 428 ± 8

Amphibolite¹
♦ 418 ± 9

Amphibolite⁶
✱ 455 ± 2
P-T-estimate
690°C, 10-12 kbar

Amphibolite⁶
✱ 439 ± 4
T-estimate
690°C

Amphibolite⁴
● 422 ± 10

Amphibolite⁴
■ 414 ± 5

Amphibolite¹
● 431 ± 5
■ 422 ± 6
Amphibolite²
♦ 430 ± 3

Amphibolite⁶
■ 409 ± 8

Amphibolite⁶
♦ 427 ± 1

Pegmatite⁵
♦ 424 ± 1

Amphibolite¹
▲ 433 ± 3

Basal zone (BASZ)

Radøy

Lindås

Holsnøy

Bergen

Study area

Caledonian belt

Sveconorwegian belt

300 km

60°07' N
4°35' E

10 km

Legend:

- Øygarden Gneiss Complex
- Hardangerfjord nappe
- Ulriken gneiss
- Bergsdalen tectonic unit
- Western Gneiss Region
- undiff. Caled. nappes

Lindås nappe

- Amphibolitic to granitic gneiss
- Anorthosite to gabbro
- Mangerite/Jotunite

★ Outcrop locality

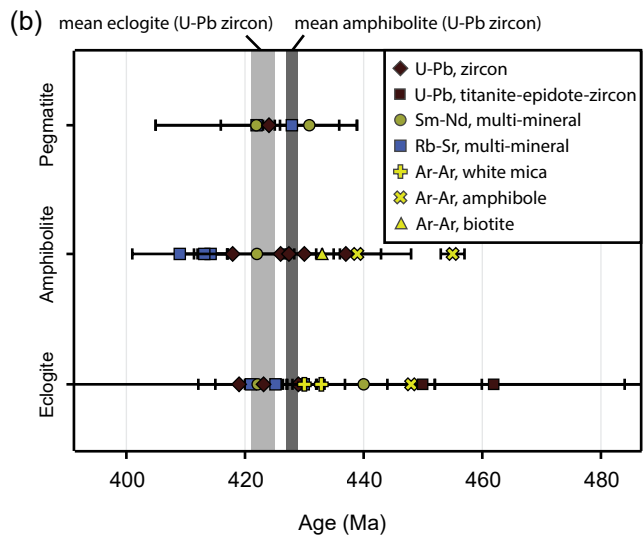


Figure 2

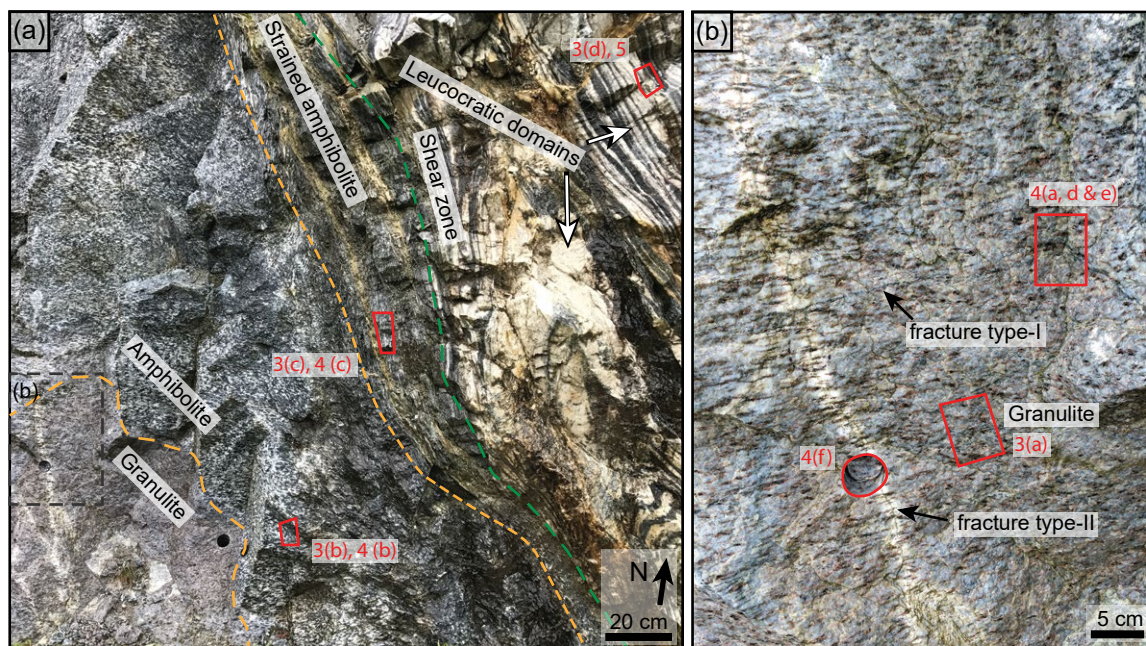


Figure 3

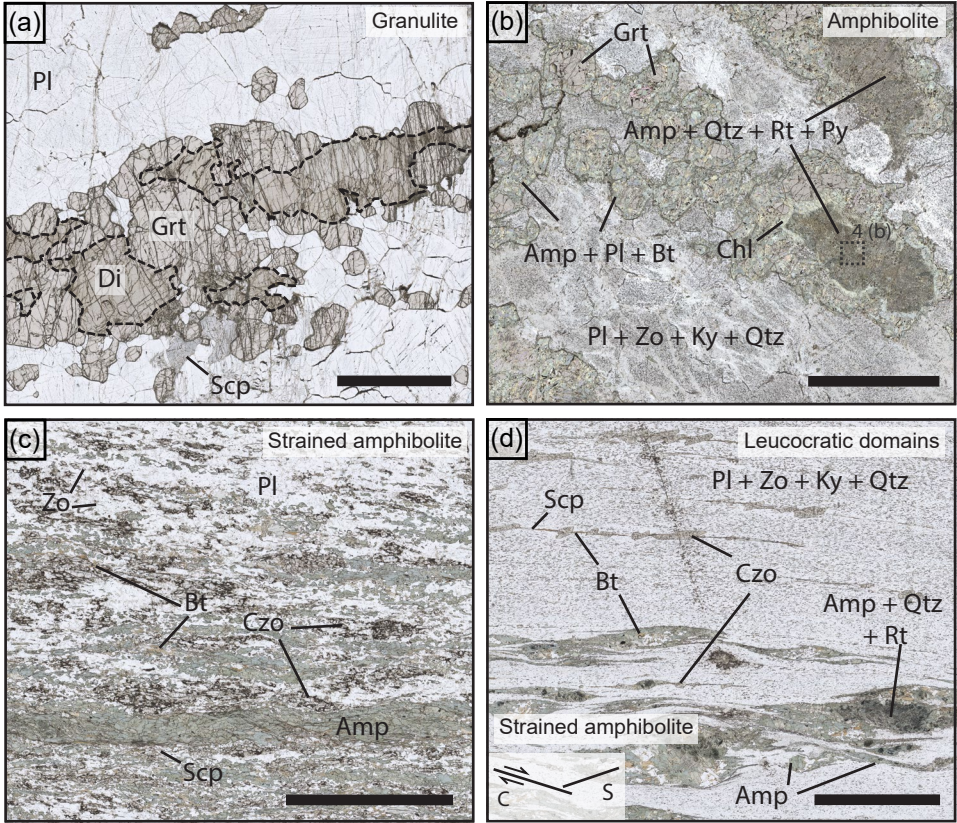


Figure 4

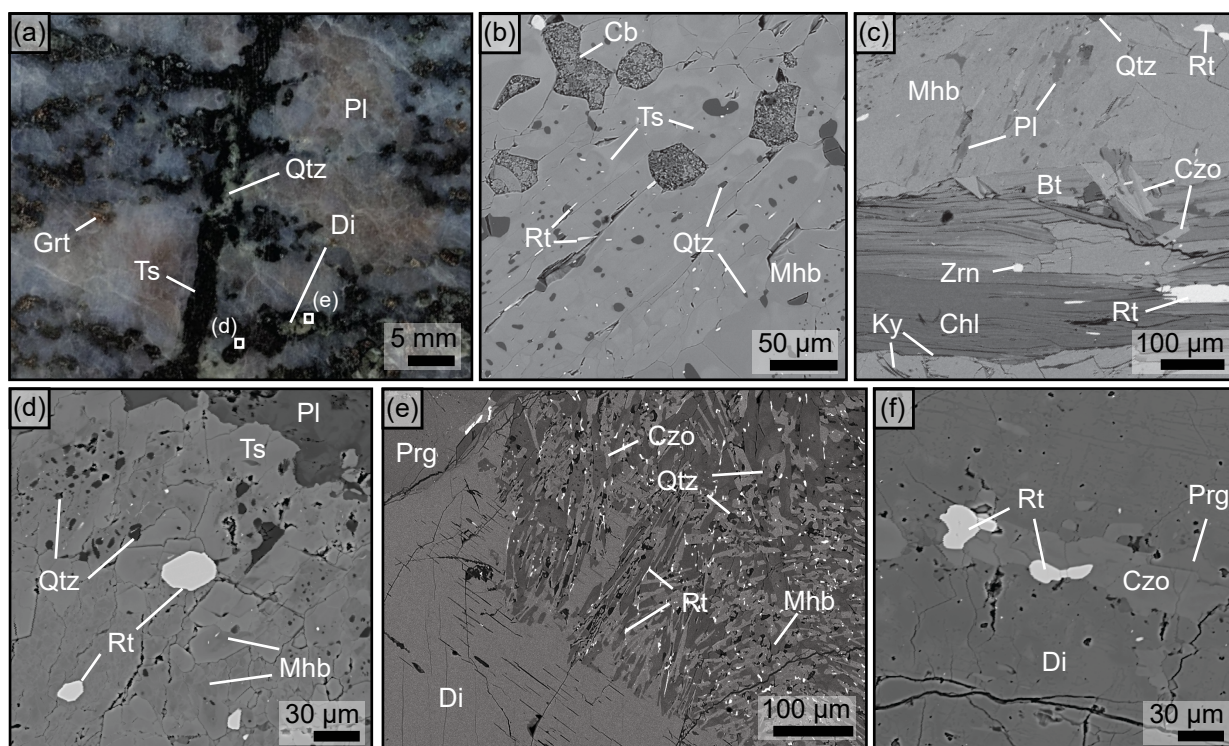


Figure 5

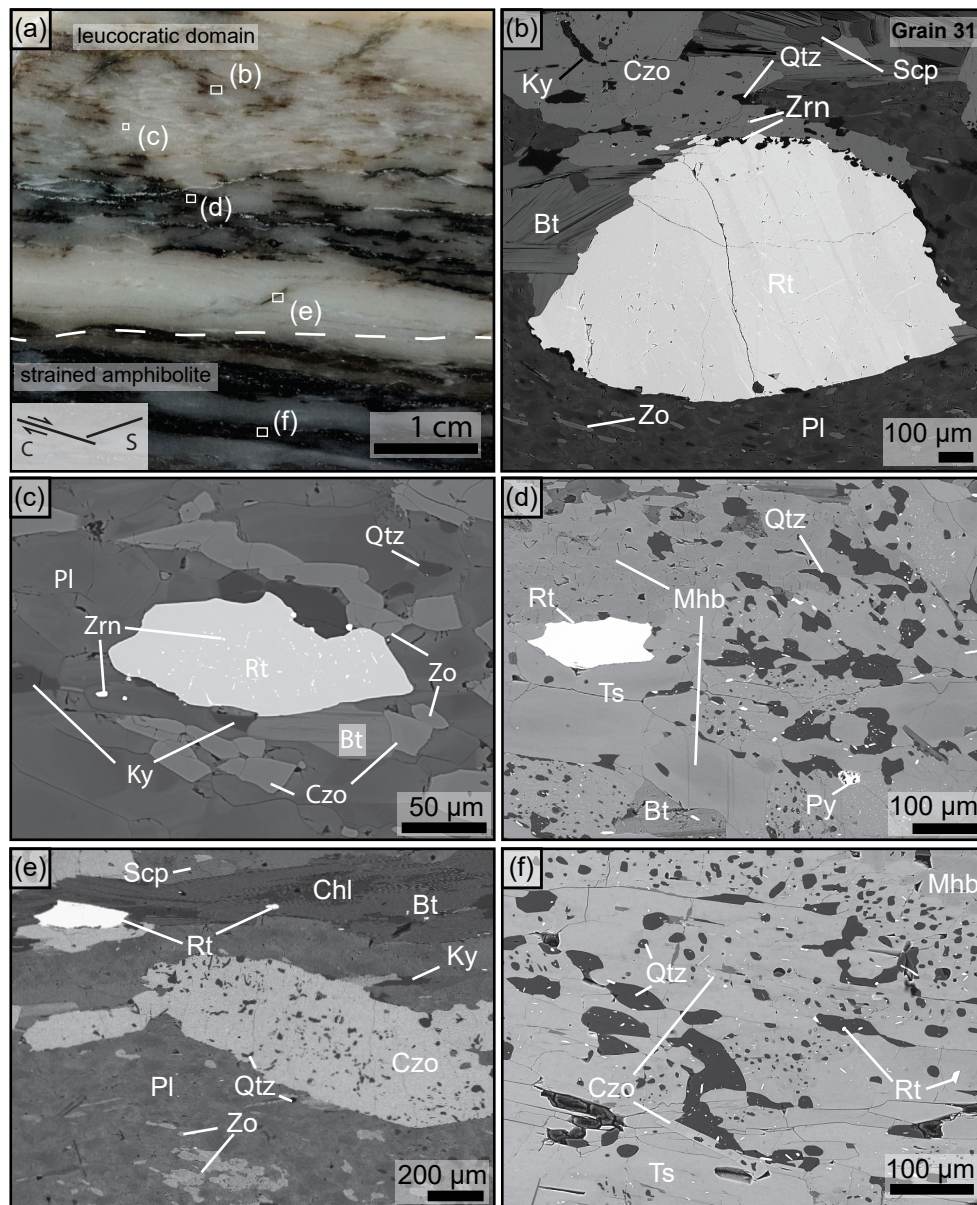


Figure 6

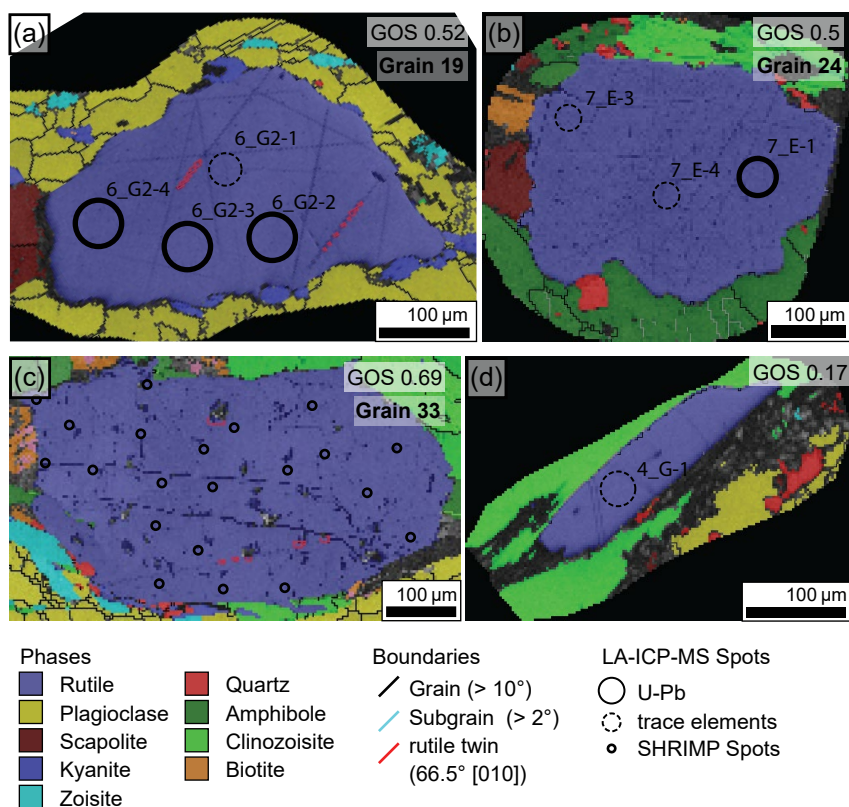


Figure 7

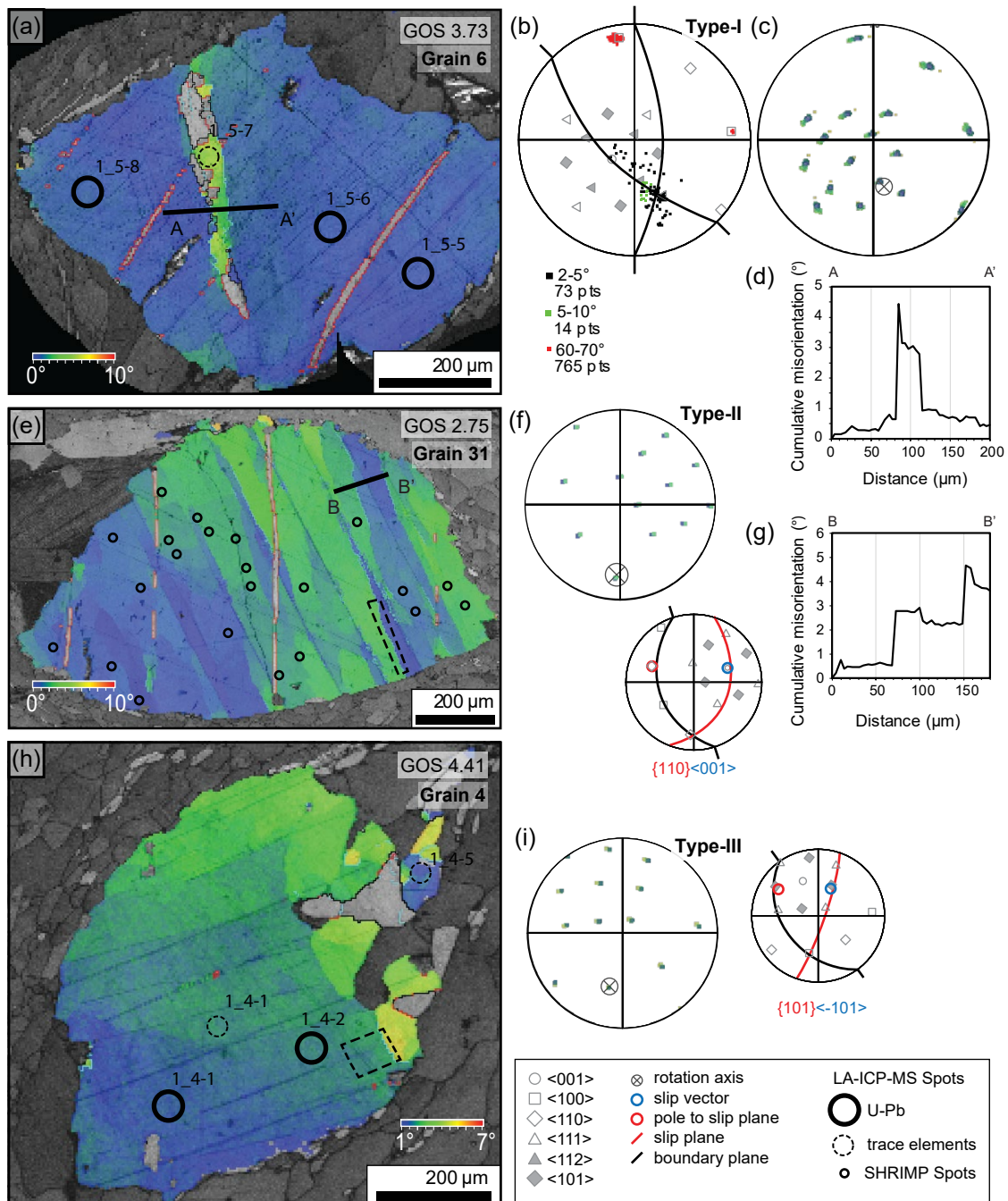


Figure 8

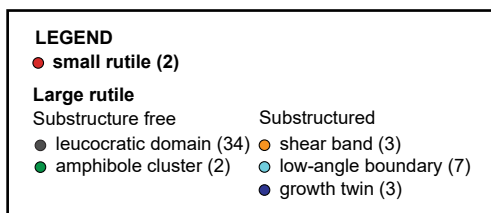
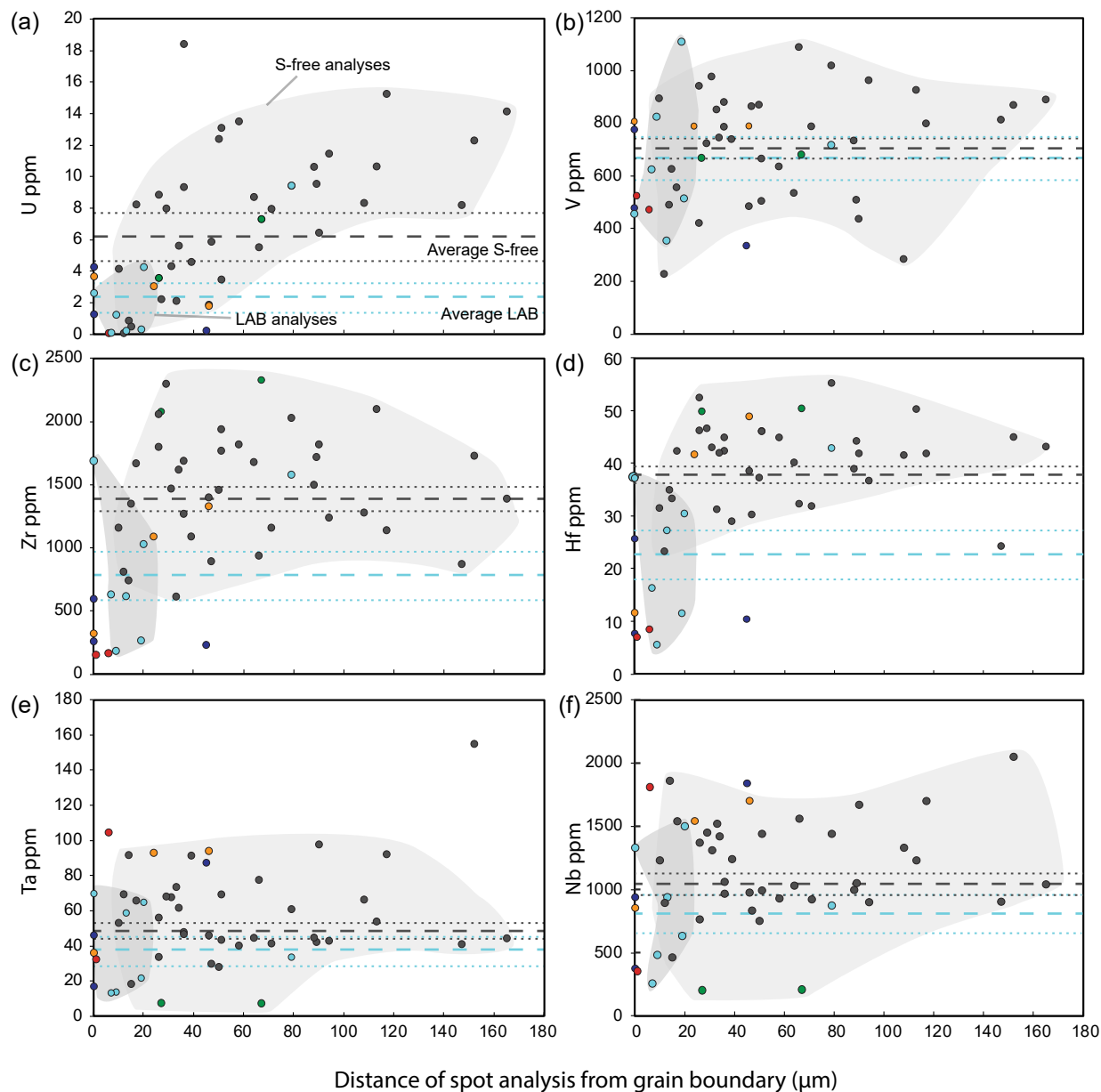


Figure 9

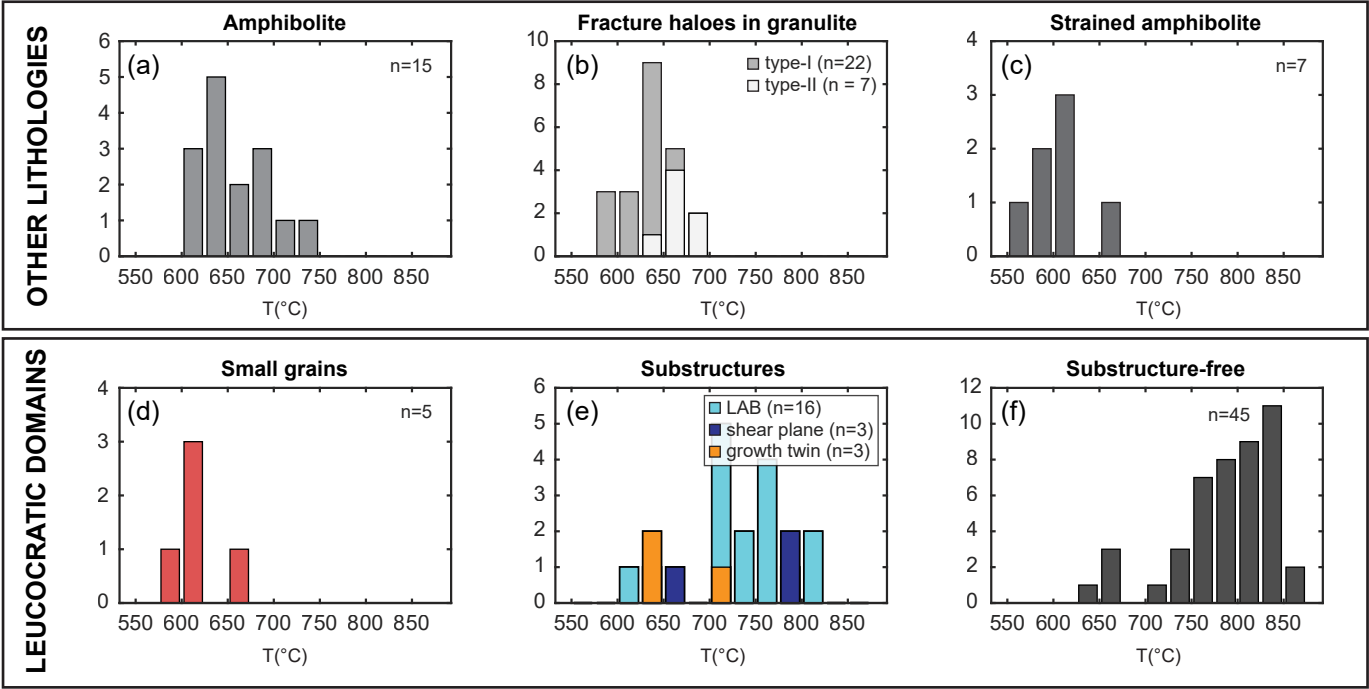


Figure 10

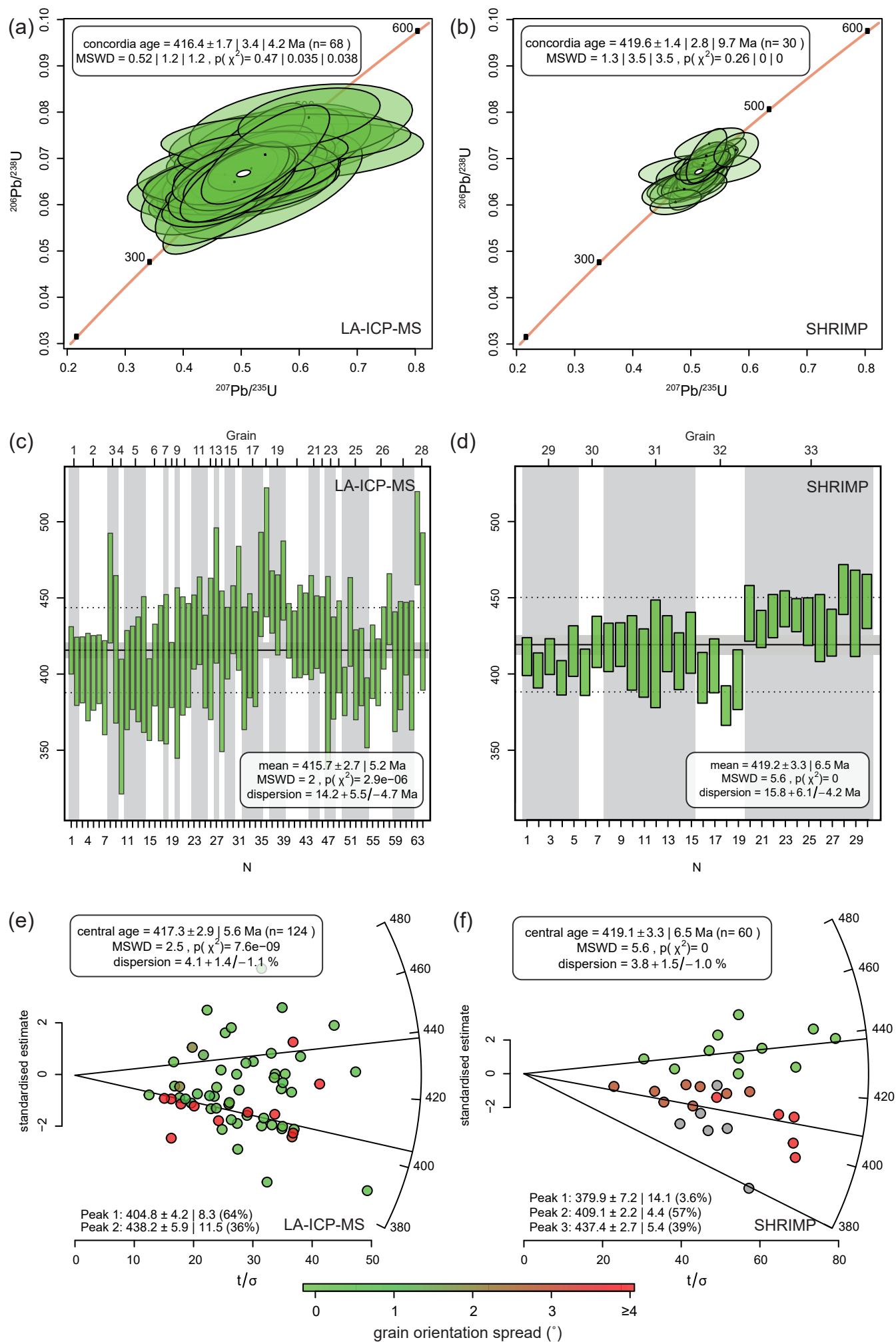
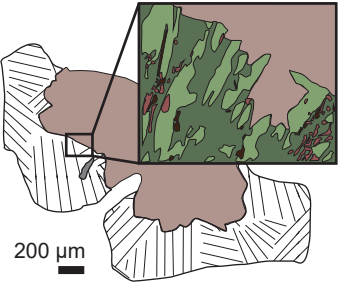


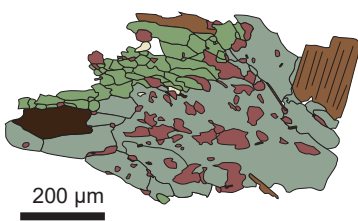
Figure 11

(a) Textural setting of rutile by lithology

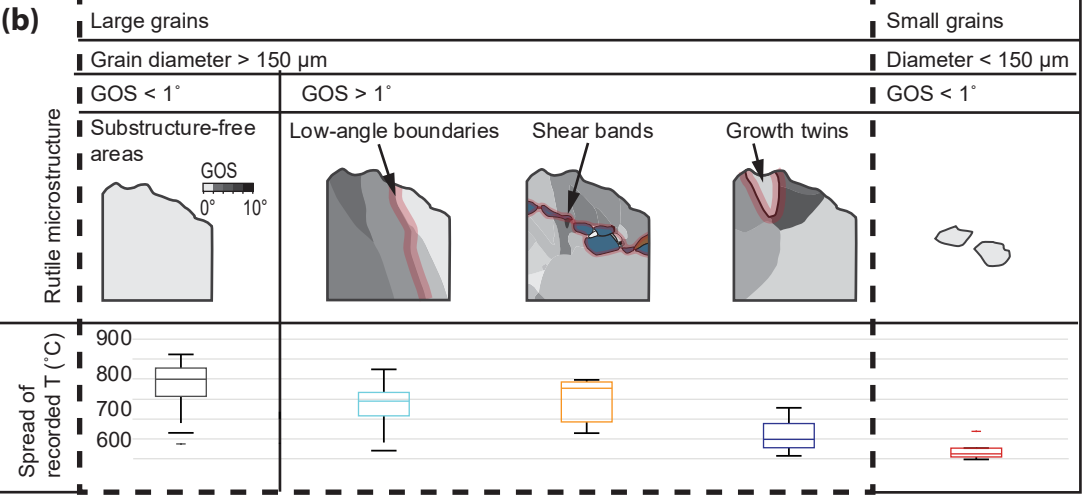
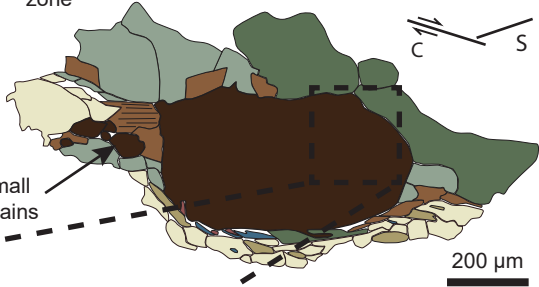
(i) granulite → amphibolite



(ii) Strained amphibolite and shear zone amphibolite



(iii) Leucocratic domains in shear zone



- Diopside
- Symplectite
- Rutile
- Mg-hornblende
- Tschermakite
- Clinzoisite
- Biotite
- Plagioclase
- Zoisite
- Quartz
- Kyanite

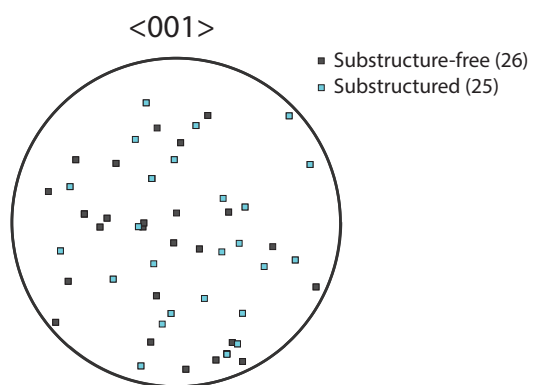


Figure S1 - C-axis orientation of all large rutile grains in respect to the cutting plane.

Table S1 - Representative amphibole analyses used for pressure calculations (b.d.l.; below detection limit, n.m.; not measured)

Lithology	Fracture type-I halo		Fracture type-II halo Amphibolite		Strained amphibolite	
Calcic amphibole classification	tschermakite	Mg-hornblende	pargasite	tschermakite	Mg-hornblende	Mg-hornblende
Technique	EDS	EDS	WDS	WDS	WDS	WDS
P estimate (kbar)						
Johnson and Rutherford, 1989 (± 0.5 kbar)	11.6	6.0	12.4	13.6	7.8	12.7
Schmidt 1991 (± 0.6 kbar)	10.6	4.3	11.5	12.8	6.3	11.8
Wt% oxide						
SiO ₂	43.2	48.8	42.2	41.5	48.0	44.7
TiO ₂	0.330	0.650	0.143	0.147	0.0836	0.144
Al ₂ O ₃	17.0	9.20	17.6	19.4	11.6	16.8
Cr ₂ O ₃	b.d.l.	b.d.l.	b.d.l.	0.0348	b.d.l.	b.d.l.
Fe ₂ O ₃	4.55	3.45	0.594	0.939	1.73	#REF!
FeO	7.03	3.23	9.75	9.71	7.55	9.02
MnO	b.d.l.	b.d.l.	0.116	0.117	0.166	0.206
MgO	12.8	18.0	11.4	10.9	14.6	11.8
CaO	11.9	13.1	12.1	12.2	12.0	11.3
Na ₂ O	1.60	0.690	1.50	1.48	1.08	1.72
K ₂ O	0.270	0.250	0.720	0.503	0.217	0.745
Cl	0.260	b.d.l.	0.341	0.206	0.0714	0.324
F	b.d.l.	b.d.l.	0.01	b.d.l.	b.d.l.	b.d.l.
O	n.m.	n.m.	0.00	n.m.	n.m.	n.m.
H ₂ O	2.02	2.14	1.98	2.02	2.10	2.01
Total	101	99.5	98.5	99.1	99.3	100

Table S1 - Representative amphibole analyses used for pressure calculations (b.d.l.; below detection limit, n.m.; not measured)

Lithology Calcic amphibole classification Technique	Leucocratic domain	
	tschermakite WDS	Mg-hornblende WDS
P estimate (kbar)		
Johnson and Rutherford, 1989 (± 0.5 kbar)	12.7	11.1
Schmidt 1991 (± 0.6 kbar)	11.9	10.1
Wt% oxide		
SiO ₂	42.1	44.6
TiO ₂	0.246	0.390
Al ₂ O ₃	18.0	16.1
Cr ₂ O ₃	0.0177	b.d.l.
Fe ₂ O ₃	2.07	#REF!
FeO	11.2	11.2
MnO	0.180	0.206
MgO	9.90	10.8
CaO	11.7	11.7
Na ₂ O	1.50	1.44
K ₂ O	0.489	0.543
Cl	0.238	0.205
F	b.d.l.	0.06
O	n.m.	0.00
H ₂ O	2.00	2.00
Total	99.6	100

Table S2 - LA-ICP-MS trace element analyses from rutile of leucocratic domains

Grain number**	Elements (ppm) (MDL filtered)	Growth twin						Shear plane		
		25		No U-Pb		No U-Pb		6		11
		7_G1-1	±2σ	7_B-3	±2σ	2_H-1	±2σ	1_5-7	±2σ	3_K-4
Analyses	Si	498	180	346	150	252	150	311	170	446
	Fe	4400	940	5010	1200	6860	990	7220	1000	6000
	U	4.26	1.10	1.26	0.34	0.22	0.040	3.65	0.56	3.04
	V	777	190	479	130	336	53	807	130	790
	Zr	260	61	596	150	231	35	322	48	1090
	Hf	7.59	1.8	25.6	6.6	10.3	1.5	11.5	1.7	41.7
	Cr	49.8	12	42.1	11	16.5	3.2	47.1	7.8	75.0
	Nb	374	88	938	240	1840	270	854	130	1542
	Ta	16.8	4.0	46.0	12	87.3	13	36.0	5.4	92.9
	Zn	136	36	4.78	4.5	8.72	4.1	12.6	4.7	6.00
	Mo	180	42	55.4	14	33.5	5.1	58.2	8.8	49.7
	W	58.3	14	47.1	12	76.8	12	31.4	4.9	44.7
	Sb	1.57	0.44	1.40	0.42	2.44	0.44	1.34	0.28	1.34
	Sn	8.72	2.2	11.0	3.0	10.2	1.7	10.5	1.7	13.5
Ratios	Nb/Ta	22.2		20.4		21.1		23.7		16.6
	Zr/Hf	34.2		23.3		22.5		27.9		26.1
Thermometry	Ln (Zr)	5.56		6.39		5.44		5.77		6.99
	P (Kbars)	12		12		12		12		12
	Temperature (°C)	647	33	718	37	638	26	664	26	776
Distance from grain boundary (µm)		0.1		0.1		45		0.1		24
	GROD	56		3.4		1.9		4.46		1.5

Table S2 - LA-ICP-MS trace element analyses from rutile of leucocratic domains

Grain number**	Elements (ppm) (MDL filtered)	11			Low angle boundaries						
		$\pm 2\sigma$	3_K-6	$\pm 2\sigma$	4	$\pm 2\sigma$	7	$\pm 2\sigma$	No U-Pb	$\pm 2\sigma$	No U-Pb
					1_4-5		2_D-1		4_BI-4		7_K-1
Analyses	Si	170	364	150	642	200	1084	290	1703	450	329
	Fe	890	5480	820	3610	510	3440	500	3740	610	3730
	U	0.50	1.79	0.30	1.23	0.19	4.25	0.68	2.60	0.48	0.09
	V	130	790	130	825	130	515	83	456	83	625
	Zr	170	1330	210	184	27	1030	150	1690	290	631
	Hf	6.4	48.9	7.6	5.45	0.80	30.4	4.6	37.2	6.4	16.3
	Cr	12	61.0	10	13.0	2.6	30.6	5.3	43.1	8.1	13.1
	Nb	240	1702	260	481	69	1500	230	1330	230	255
	Ta	14	94.0	15	13.6	2.0	64.7	9.8	69.7	12	13.1
	Zn	4.1	3.68	3.8	1.28	3.0	11.9	4.5	4.07	4.1	9.53
	Mo	7.8	57.9	9.1	4.66	0.78	59.6	9.1	18.0	3.2	17.2
	W	7.2	42.4	6.8	77.1	12	49.6	7.8	99.4	18	57.2
	Sb	0.28	1.52	0.30	2.37	0.42	1.72	0.34	2.21	0.46	2.26
	Sn	2.3	15.3	2.5	6.34	1.0	13.8	2.2	5.82	1.1	7.55
Ratios	Nb/Ta		18.1		35.3		23.2		19.1		19.4
	Zr/Hf		27.2		33.8		33.8		45.5		38.8
Thermometry	Ln (Zr)		7.19		5.22		6.94		7.43		6.45
	P (Kbars)		12		12		12		12		12
	Temperature (°C)	29	797	31	620	25	770	28	823	33	723
Distance from grain boundary (µm)			46		9		20		0.1		7
	GROD		2.47		1.21		6.99		24.6		6.33

Table S2 - LA-ICP-MS trace element analyses from rutile of leucocratic domains

Grain number**	Elements (ppm) (MDL filtered)								<i>Small grains</i>		
		No U-Pb		No U-Pb		22			No U-Pb		No U-Pb
		$\pm 2\sigma$	3_I-1	$\pm 2\sigma$	5_B-1	$\pm 2\sigma$	6_H3-3	$\pm 2\sigma$	4_BI-1	$\pm 2\sigma$	4_G-1
Analyses	Si	150	282	140	445	190	486	180	66.9	130	1366
	Fe	790	3330	500	3890	700	6920	1400	4130	660	2790
	U	0.024	0.301	0.054	0.21	0.050	9.41	2.20	0.06	0.016	b.d.l
	V	150	1110	180	355	71	718	160	473	84	525
	Zr	150	267	42	618	120	1580	350	166	28	153
	Hf	3.8	11.4	1.8	27.2	5.2	42.9	9.5	8.37	1.4	6.90
	Cr	3.6	32.3	5.7	86.2	18	66.6	16	42.4	7.9	16.5
	Nb	59	632	99	939	180	873	190	1810	310	353
	Ta	3.1	21.6	3.4	58.7	11	33.5	7.5	105	18	32.3
	Zn	4.9	6.38	4.0	8.41	5.4	7.07	4.4	3.33	3.7	2.31
	Mo	4.0	13.5	2.2	40.8	7.9	78.5	17	23.4	4.1	3.85
	W	14	101	16	37.3	7.4	43.5	9.9	78.0	14	103
	Sb	0.60	2.59	0.50	2.24	0.52	1.00	0.28	1.92	0.40	1.49
	Sn	1.9	8.2	1.4	11.4	2.4	13.2	3.1	8.23	1.5	3.73
Ratios	Nb/Ta		29.3		16.0		26.0		17.3		10.9
	Zr/Hf		23.3		22.7		36.8		19.8		22.2
Thermometry	Ln (Zr)		5.59		6.43		7.37		5.11		5.03
	P (Kbars)		12		12		12		12		12
	Temperature (°C)	35	649	26	721	31	816	39	613	26	607
Distance from grain boundary (µm)			19		13		79		6		1
	GROD		1.07		5.17		0.225		22.9		0.265

Table S2 - LA-ICP-MS trace element analyses from rutile of leucocratic domains

Grain number**	Elements (ppm) (MDL filtered)	$\pm 2\sigma$	<i>Amphibole cluster</i>				<i>Large grains in leucocratic domain</i>				
			24		24		1		2		2
			7_E-3	$\pm 2\sigma$	7_E-4	$\pm 2\sigma$	1_1-1	$\pm 2\sigma$	1_2-2	$\pm 2\sigma$	1_2-4
Analyses	Si	380	516	190	276	140	307	160	718	250	435
	Fe	490	4310	980	3620	820	4950	700	6650	940	5740
	U		7.28	1.9	2.21	0.58	18.4	2.8	14.1	2.1	9.32
	V	100	682	170	669	170	787	120	891	140	881
	Zr	28	2330	580	2080	520	1690	240	1390	200	1270
	Hf	1.3	50.5	13	49.9	13	44.9	6.5	43.2	6.3	42.4
	Cr	3.7	14.4	4.1	13.3	3.9	32.0	5.4	46.2	7.7	42.1
	Nb	65	207	51	202	50	966	140	1040	150	1060
	Ta	6.1	7.20	1.8	7.38	1.9	47.8	7.0	44.2	6.5	46.6
	Zn	4.1	1.79	4.7	16.7	6.6	4.40	3.5	6.64	4.7	5.43
	Mo	0.86	35.8	8.8	30.4	7.6	60.4	8.9	64.8	9.7	65.2
	W	20	11.7	3.0	13.0	3.4	25.9	3.9	32.5	4.9	32.7
	Sb	0.36	1.14	0.34	1.38	0.40	1.05	0.22	1.20	0.26	1.16
	Sn	0.80	15.8	4.1	14.6	3.9	15.5	2.4	15.5	2.5	14.2
Ratios	Nb/Ta		28.8		27.3		20.2		23.5		22.7
	Zr/Hf		46.2		41.7		37.6		32.2		30.0
Thermometry	Ln (Zr)		7.75		7.64		7.43		7.24		7.15
	P (Kbars)		12		12		12		12		12
	Temperature (°C)	27	861	45	847	43	823	30	802	30	792
Distance from grain boundary (μm)			67		27		36		165		36
	GROD		0.125		0.595		0.585		0.865		0.255

Table S2 - LA-ICP-MS trace element analyses from rutile of leucocratic domains

Grain number**	Elements (ppm) (MDL filtered)	3		4		5		5		7	
		$\pm 2\sigma$	1_3-1	$\pm 2\sigma$	1_4-1	$\pm 2\sigma$	1_5-2	$\pm 2\sigma$	1_5-4	$\pm 2\sigma$	2_D-3
Analyses	Si	210	354	170	705	210	1280	390	612	290	492
	Fe	810	8660	1200	7160	1000	7650	1100	5160	730	4900
	U	1.4	8.31	1.3	12.3	1.8	10.6	1.6	4.14	0.64	8.22
	V	140	285	45	870	130	927	140	895	140	557
	Zr	180	1280	190	1730	250	2100	310	1160	170	1670
	Hf	6.2	41.6	6.2	45.0	6.5	50.3	7.4	31.5	4.6	42.4
	Cr	7.1	31.0	5.4	18.4	3.3	45.3	7.8	46.1	8.0	32.3
	Nb	150	1330	200	2050	300	1230	180	1230	180	1540
	Ta	6.9	66.3	9.9	155	23	53.8	7.9	53.0	7.9	65.7
	Zn	4.7	5.92	4.2	b.d.l.	3.0	13.5	6.7	12.4	6.8	12.6
	Mo	9.7	66.3	10	68.3	10	92.0	14	77.0	12	73.6
	W	5.0	41.2	6.4	42.3	6.3	55.6	8.5	56.0	8.6	52.8
	Sb	0.24	1.03	0.22	1.11	0.22	1.11	0.26	1.73	0.36	1.16
	Sn	2.3	15.3	2.5	17.6	2.7	17.1	2.7	15.1	2.4	15.4
Ratios	Nb/Ta		20.1		13.2		22.9		23.2		23.4
	Zr/Hf		30.8		38.4		41.7		36.8		39.4
Thermometry	Ln (Zr)		7.15		7.46		7.65		7.06		7.42
	P (Kbars)		12		12		12		12		12
	Temperature (°C)	29	793	30	826	30	849	31	783	28	822
Distance from grain boundary (µm)			108		152		113		10		17
	GROD		0.485		2.04		0.295		0.415		1.23

Table S2 - LA-ICP-MS trace element analyses from rutile of leucocratic domains

Grain number**	Elements (ppm) (MDL filtered)	8		9		10		11		No U-Pb	
		$\pm 2\sigma$	2_G-1	$\pm 2\sigma$	3_C-1	$\pm 2\sigma$	3_G2-1	$\pm 2\sigma$	3_K-1	$\pm 2\sigma$	4_BII-1
Analyses	Si	180	277	150	536	180	988	280	331	160	462
	Fe	710	5480	800	3980	600	6970	1000	6700	990	4990
	U	1.3	11.4	1.8	4.31	0.72	6.43	1.1	15.2	2.4	0.86
	V	90	964	150	978	160	438	72	800	130	491
	Zr	250	1240	190	1470	230	1820	290	1140	170	743
	Hf	6.4	36.7	5.5	43.0	6.8	41.9	6.5	41.9	6.4	34.9
	Cr	5.5	60.3	9.9	48.9	8.4	34.3	6.1	69.7	12	38.1
	Nb	230	899	130	1310	210	1670	260	1700	260	1860
	Ta	10	42.8	6.5	67.7	11	97.7	15	92.1	14	91.7
	Zn	4.6	13.1	4.6	2.01	3.9	6.45	4.9	6.52	4.3	2.42
	Mo	11	69.0	11	50.4	8.1	70.0	11	76.9	12	40.3
	W	8.3	32.5	5.1	42.6	7.0	49.0	7.9	42.4	6.7	62.2
	Sb	0.24	1.17	0.24	1.39	0.28	1.16	0.26	1.20	0.24	1.60
	Sn	2.5	15.0	2.4	14.0	2.4	17.3	2.9	17.2	2.8	12.1
Ratios	Nb/Ta		21.0		19.4		17.1		18.5		20.3
	Zr/Hf		33.8		34.2		43.4		27.2		21.3
Thermometry	Ln (Zr)		7.12		7.29		7.51		7.04		6.61
	P (Kbars)		12		12		12		12		12
	Temperature (°C)	31	790	29	808	31	832	32	781	29	738
Distance from grain boundary (µm)			94		31		90		117		14
	GROD		0.185		0.35		0.475		1.99		0.305

Table S2 - LA-ICP-MS trace element analyses from rutile of leucocratic domains

Grain number**	Elements (ppm) (MDL filtered)	13		14		15		16		No U-Pb	
		$\pm 2\sigma$	4_I-1	$\pm 2\sigma$	4_M-2	$\pm 2\sigma$	4_N-5	$\pm 2\sigma$	4_NII-2	$\pm 2\sigma$	5_A-1
Analyses	Si	170	1050	300	377	190	514	180	1768	470	317
	Fe	820	6370	1100	6030	1000	4940	840	4480	770	5330
	U	0.16	5.51	1.1	2.11	0.40	9.40	1.8	8.83	1.7	3.46
	V	90	1090	210	853	160	1020	190	943	180	667
	Zr	130	939	170	614	110	2030	370	1800	330	1770
	Hf	6.1	32.3	6.0	31.2	5.5	55.3	10	52.5	9.6	46.1
	Cr	7.3	38.8	7.8	64.3	12	67.7	13	77.6	15	42.9
	Nb	320	1560	290	1520	270	1440	260	1370	250	1440
	Ta	16	77.5	14	73.5	13	60.8	11	56.0	10	69.2
	Zn	3.8	14.2	5.2	b.d.l.	5.1	6.24	4.0	10.8	4.5	5.05
	Mo	7.1	67.3	12	59.6	11	70.5	13	65.9	12	68.9
	W	11.2	49.8	9.5	39.4	7.3	41.2	7.7	44.7	8.5	44.7
	Sb	0.34	1.15	0.28	1.29	0.32	1.26	0.28	1.50	0.34	1.00
	Sn	2.3	15.0	3.0	14.1	2.7	14.2	2.8	16.8	3.3	14.9
Ratios	Nb/Ta		20.1		20.7		23.7		24.5		20.8
	Zr/Hf		29.1		19.7		36.7		34.3		38.4
Thermometry	Ln (Zr)		6.84		6.42		7.62		7.50		7.48
	P (Kbars)		12		12		12		12		12
	Temperature (°C)	30	761	31	720	29	845	35	831	35	829
Distance from grain boundary (µm)			66		33		79		26		51
	GROD		0.615		0.405		1.02		1.706		0.295

Table S2 - LA-ICP-MS trace element analyses from rutile of leucocratic domains

Grain number**	Elements (ppm) (MDL filtered)	No U-Pb		No U-Pb		19		20		20	
		$\pm 2\sigma$	6_A-1	$\pm 2\sigma$	6_B-1	$\pm 2\sigma$	6_G2-1	$\pm 2\sigma$	6_H1-2	$\pm 2\sigma$	6_H1-3
Analyses	Si	150	678	220	544	200	520	190	476	170	401
	Fe	950	4440	910	4600	940	7300	1300	5140	1000	4050
	U	0.70	3.56	0.84	4.57	1.1	13.5	2.8	12.4	2.8	5.86
	V	130	422	98	740	170	637	130	871	190	865
	Zr	340	2060	460	1090	240	1820	360	1460	310	894
	Hf	8.8	46.3	10	29.0	6.5	44.9	8.9	37.3	8.1	30.3
	Cr	8.9	26.0	6.3	46.7	11	63.0	13	78.1	18	69.9
	Nb	270	763	170	1240	280	928	180	751	160	833
	Ta	13	33.6	7.6	91.4	21	40.1	8.1	27.9	6.1	29.7
	Zn	4.6	8.29	4.5	5.94	4.6	6.75	4.8	2.53	3.6	4.44
	Mo	13	48.6	11	59.6	13	73.6	15	73.7	16	52.3
	W	8.8	28.9	6.7	50.7	12	44.3	9.1	46.2	10	47.9
	Sb	0.26	1.06	0.30	1.20	0.32	1.08	0.28	1.09	0.28	1.23
	Sn	3.0	15.5	3.7	12.9	3.1	13.3	2.8	14.2	3.3	12.2
Ratios	Nb/Ta		22.7		13.6		23.1		26.9		28.0
	Zr/Hf		44.5		37.6		40.5		39.2		29.6
Thermometry	Ln (Zr)		7.63		6.99		7.51		7.29		6.80
	P (Kbars)		12		12		12		12		12
	Temperature (°C)	36	846	40	776	36	832	37	807	38	756
Distance from grain boundary (µm)			26		39		58		50		47
	GROD		0.385		0.565		0.125		0.335		0.255

Table S2 - LA-ICP-MS trace element analyses from rutile of leucocratic domains

Grain number**	Elements (ppm) (MDL filtered)	23		No U-Pb		No U-Pb		No U-Pb		25	
		$\pm 2\sigma$	6_J1-1	$\pm 2\sigma$	6_J5-1	$\pm 2\sigma$	7_B-1	$\pm 2\sigma$	7_C-1	$\pm 2\sigma$	7_G1-3
Analyses	Si	160	939	270	753	230	406	160	278	130	553
	Fe	810	4110	700	5390	980	4510	1000	3830	860	5000
	U	1.3	7.96	1.6	5.60	1.1	1.86	0.50	0.0643	0.020	8.18
	V	190	725	150	746	150	486	130	229	58	814
	Zr	190	2300	440	1620	320	1400	350	811	200	872
	Hf	6.6	46.7	9.0	42.0	8.2	38.6	9.8	23.2	5.7	24.2
	Cr	16	57.4	12	46.5	9.8	47.4	13	8.4	2.6	51.1
	Nb	180	1450	280	1420	280	975	250	893	220	903
	Ta	6.5	68.1	13	61.6	12	45.9	12	69.3	17	40.9
	Zn	3.8	4.76	4.0	8.08	4.4	3.35	4.3	4.50	4.3	4.45
	Mo	11	49.5	9.6	75.4	15	65.2	16	14.4	3.6	81.9
	W	11	62.4	13	52.4	11	40.0	11	54.2	14	47.1
	Sb	0.32	1.90	0.44	1.69	0.40	1.27	0.38	1.74	0.50	1.11
	Sn	2.8	12.0	2.5	13.4	2.8	13.7	3.7	8.12	2.1	15.9
Ratios	Nb/Ta		21.3		23.0		21.2		12.9		22.1
	Zr/Hf		49.3		38.6		36.3		34.9		36.0
Thermometry	Ln (Zr)		7.74		7.39		7.24		6.70		6.77
	P (Kbars)		12		12		12		12		12
	Temperature (°C)	35	859	37	819	36	803	42	747	37	754
Distance from grain boundary (µm)			29		34		46		12		147
	GROD		0.385		0.335		4.52		2.38		2.43

Table S2 - LA-ICP-MS trace element analyses from rutile of leucocratic domains

Grain number**		25		26		26		No U-Pb		27	
	Elements (ppm) (MDL filtered)	$\pm 2\sigma$	7_G1-8	$\pm 2\sigma$	7_G2-1	$\pm 2\sigma$	7_G2-2	$\pm 2\sigma$	7_K-2	$\pm 2\sigma$	7_L1-3
Analyses	Si	190	610	210	341	140	197	120	403	160	695
	Fe	1100	4680	1000	4750	1000	4690	1000	4010	860	8170
	U	2.0	7.94	2.0	13.1	3.3	9.52	2.4	0.483	0.12	10.6
	V	200	789	190	506	130	510	130	627	150	735
	Zr	210	1160	280	1940	470	1720	420	1350	320	1500
	Hf	5.8	31.9	7.6	46.1	11	44.3	11	33.3	7.8	39.0
	Cr	13	44.2	11	53.6	14	62.2	16	20.0	5.2	52.5
	Nb	210	921	220	992	240	1050	250	462	110	996
	Ta	9.8	41.3	10	43.4	11	42.1	10	18.3	4.3	44.6
	Zn	4.2	b.d.l.	4.1	2.27	4.0	0.641	4.1	11.6	5.3	9.38
	Mo	19	76.1	18	86.4	21	80.9	19	35.2	8.2	86.7
	W	12	41.6	10	48.2	12	48.1	12	18.9	4.6	48.9
	Sb	0.32	1.19	0.34	0.895	0.26	0.91	0.26	1.23	0.34	1.22
	Sn	4.0	14.8	3.8	13.9	3.5	13.9	3.6	15.1	3.7	15.5
Ratios	Nb/Ta		22.3		22.9		24.9		25.3		22.3
	Zr/Hf		36.4		42.1		38.9		40.5		38.5
Thermometry	Ln (Zr)		7.06		7.57		7.45		7.21		7.31
	P (Kbars)		12		12		12		12		12
	Temperature (°C)	36	783	38	839	42	825	42	799	39	810
Distance from grain boundary (µm)			71		51		89		15		88
	GROD		2.22		0.805		1.25		0.535		0.125

Table S2 - LA-ICP-MS trace element analyses from rutile of leucocratic domains

Grain number**	28			
	Elements (ppm) (MDL filtered)	$\pm 2\sigma$	7_L2-1	$\pm 2\sigma$
Analyses	Si	230	674	220
	Fe	1710	4330	900
	U	2.5	8.69	2.1
	V	170	536	130
	Zr	340	1680	390
	Hf	8.9	40.2	9.3
	Cr	13	50.3	12
	Nb	230	1030	240
	Ta	10	44.5	10
	Zn	4.9	5.40	4.2
	Mo	20	77.9	18
	W	12	48.5	12
	Sb	0.34	0.932	0.26
	Sn	3.8	14.3	3.5
Ratios	Nb/Ta		23.1	
	Zr/Hf		41.8	
Thermometry	Ln (Zr)		7.43	
	P (Kbars)		12	
	Temperature (°C)	39	823	40
Distance from grain boundary (μm)			64	
	GROD		0.325	

Table S3 - EMPA major and trace element data for all lithologies

Lithology	Amphibolite					
Type						
Analyses	17FJ05_R1_1	17FJ05_R1_2	17FJ05_R2_1	17FJ05_R2_2	17FJ05_R2_3	17FJ05_R2_4
Wt% oxide						
SiO ₂	0.200	0.758	0.415	0.0636	0.652	0.137
TiO ₂	99.1	96.3	99.7	101	96.6	98.9
Al ₂ O ₃	0.0227	0.0610	0.144	0.0138	0.153	0.0375
Cr ₂ O ₃	b.d.l.	b.d.l.	0.0658	0.0556	0.0469	0.0393
FeO	0.485	0.606	0.376	0.276	0.337	0.322
MnO	0.0160	0.0152	b.d.l.	b.d.l.	b.d.l.	b.d.l.
NiO	b.d.l.	0.00736	b.d.l.	b.d.l.	b.d.l.	b.d.l.
CaO	0.709	1.05	0.698	0.463	1.12	0.714
Nb ₂ O ₅	0.0275	0.0179	0.0184	0.0123	0.0133	0.0167
ZrO ₂	0.0527	0.0456	0.0276	0.0234	0.0305	0.0197
HfO ₂	b.d.l.	b.d.l.	b.d.l.	b.d.l.	b.d.l.	b.d.l.
V ₂ O ₃	0.0464	b.d.l.	0.0824	0.0914	0.0569	0.0931
Total	101	98.8	102	102	99.0	100
Elements (ppm)						
Si	936	3540	1940	297	3050	640
Al	120	323	762	73	808	199
Cr	b.d.l.	b.d.l.	451	381	321	269
Fe	3770	4710	2930	2150	2620	2500
Ni	b.d.l.	57.8	b.d.l.	b.d.l.	b.d.l.	b.d.l.
V	260	b.d.l.	462	512	319	522
Nb	192	125	129	86.0	92.7	117
Zr	390	337	205	173	226	146
Thermometer (Tomkins et al 2007)						
In (Zr ppm)	5.97	5.82	5.32	5.15	5.42	4.98
P (Kbar)	13	13	13	13	13	13
Temperature (°C)	685	672	632	620	640	607
Error (2σ)*	19	20	24	25	23	27

Table S3 - EMPA major and trace element data for all lithologies

Lithology								
Type								
Analyses	17FJ05_R2	17FJ05_R2	17FJ05_R3	17FJ05_R3	17FJ05_R3	17FJ05_R3	17FJ05_R3	H2 R15
Wt% oxide								
SiO ₂	0.0807	0.878	0.0546	0.0428	0.0385	0.0429	0.361	0.581
TiO ₂	99.8	99.3	100	101	101	101	99.8	98.3
Al ₂ O ₃	0.00519	0.306	0.0198	b.d.l.	0.00781	0.0103	0.110	0.254
Cr ₂ O ₃	0.0539	0.0404	0.0505	0.0415	0.0708	0.0583	0.0533	b.d.l.
FeO	0.413	0.667	0.383	0.359	0.327	0.323	0.387	0.421
MnO	b.d.l.	b.d.l.	b.d.l.	b.d.l.	0.0106	0.00611	b.d.l.	0.00693
NiO	b.d.l.	b.d.l.	b.d.l.	b.d.l.	b.d.l.	b.d.l.	b.d.l.	0.00988
CaO	0.548	0.744	0.314	0.270	0.268	0.286	0.557	1.00
Nb ₂ O ₅	0.0182	0.0156	0.0196	0.0140	0.0191	0.0152	0.0130	0.0447
ZrO ₂	0.0254	0.0209	0.0557	0.0340	0.0291	0.0469	0.0564	0.0712
HfO ₂	b.d.l.	b.d.l.	b.d.l.	b.d.l.	b.d.l.	b.d.l.	b.d.l.	b.d.l.
V ₂ O ₃	0.0974	0.0610	0.0573	0.0757	0.0732	0.0600	0.0667	0.0187
Total	101	102	101	101	102	102	101	101
Elements (ppm)								
Si	377	4110	255	200	180	201	1690	2720
Al	27.5	1620	105	b.d.l.	41.3	54.5	582	1340
Cr	369	276	346	284	485	399	364	b.d.l.
Fe	3210	5180	2970	2790	2550	2510	3010	3270
Ni	b.d.l.	b.d.l.	b.d.l.	b.d.l.	b.d.l.	b.d.l.	b.d.l.	77.7
V	545	342	321	424	410	336	374	105
Nb	128	109	137	97.9	134	106	90.8	313
Zr	188	155	412	252	216	347	418	527
Thermometer (Tomki)								
In (Zr ppm)	5.24	5.04	6.02	5.53	5.37	5.85	6.03	6.27
P (Kbar)	13	13	13	13	13	13	13	13
Temperature (°C)	626	612	689	648	636	675	690	715
Error (2σ)*	25	26	19	22	24	20	19	18

Table S3 - EMPA major and trace element data for all lithologies

Lithology Type	Strained amphibolite							
	H2 R16	FJ7-2 R1	FJ7-2 R2	FJ7-2 R2	FJ7-2 R7	FJ7-2 R9	FJ7-2 R6	FJ7-2 R10
Analyses								
Wt% oxide								
SiO ₂	0.0997	0.0416	0.0411	0.0859	0.274	0.104	0.254	0.0853
TiO ₂	100	100	101	101	99.4	100	101	101
Al ₂ O ₃	0.00759	b.d.l.	b.d.l.	0.0198	0.0912	0.0361	0.0745	0.0247
Cr ₂ O ₃	b.d.l.	0.0370	b.d.l.	0.0254	0.0341	0.0621	0.0248	0.0378
FeO	0.385	0.412	0.396	0.504	0.637	0.480	0.650	0.564
MnO	b.d.l.	b.d.l.	b.d.l.	b.d.l.	b.d.l.	0.00988	0.0114	b.d.l.
NiO	b.d.l.	b.d.l.	b.d.l.	b.d.l.	b.d.l.	b.d.l.	b.d.l.	b.d.l.
CaO	1.00	0.0244	0.0276	0.0398	0.513	0.244	0.525	0.334
Nb ₂ O ₅	0.0476	0.0890	0.0681	0.218	0.0899	0.142	0.0878	0.1635
ZrO ₂	0.0772	0.0196	0.0261	0.0100	0.0175	0.0241	0.0334	0.0112
HfO ₂	b.d.l.	b.d.l.	b.d.l.	b.d.l.	b.d.l.	b.d.l.	b.d.l.	b.d.l.
V ₂ O ₃	b.d.l.	0.0234	0.0329	0.0165	0.0267	0.0341	b.d.l.	b.d.l.
Total	102	101	101	102	101	101	103	103
Elements (ppm)								
Si	466	195	192	401	1280	486	1190	399
Al	40.2	b.d.l.	b.d.l.	105	482	191	394	131
Cr	b.d.l.	253	b.d.l.	174	233	425	170	259
Fe	2990	3200	3080	3920	4950	3730	5060	4390
Ni	b.d.l.	b.d.l.	b.d.l.	b.d.l.	b.d.l.	b.d.l.	b.d.l.	b.d.l.
V	b.d.l.	131	184	92.4	149	191	b.d.l.	b.d.l.
Nb	333	622	476	1530	628	994	614	1140
Zr	572	145	193	73.9	129	178	247	83
Thermometer (Tomki)								
In (Zr ppm)	6.35	4.97	5.26	4.30	4.86	5.18	5.51	4.42
P (Kbar)	13	12	12	12	12	12	12	12
Temperature (°C)	727	603	624	557	595	618	655	580
Error (2σ)*	17	26	24	35	27	25	22	34

Table S3 - EMPA major and trace element data for all lithologies

Lithology	Fracture type-I halo				
Type					
Analyses	17FJ02A_R2_1	17FJ02A_R2_2	17FJ02A_R2_3	17FJ02A_R3_1	17FJ02A_R3_2
Wt% oxide					
SiO ₂	0.0446	0.0352	0.0444	0.0598	0.0522
TiO ₂	98.4	99.7	100	99.7	101
Al ₂ O ₃	b.d.l.	b.d.l.	b.d.l.	b.d.l.	b.d.l.
Cr ₂ O ₃	0.140	0.139	0.165	0.0861	0.0853
FeO	0.322	0.299	0.322	0.383	0.377
MnO	0.0107	b.d.l.	b.d.l.	b.d.l.	b.d.l.
NiO	b.d.l.	b.d.l.	b.d.l.	b.d.l.	b.d.l.
CaO	0.304	0.250	0.311	0.261	0.222
Nb ₂ O ₅	0.0351	0.0252	0.0211	0.0657	0.0573
ZrO ₂	0.0198	0.0291	0.0336	0.0276	0.0265
HfO ₂	b.d.l.	b.d.l.	b.d.l.	b.d.l.	b.d.l.
V ₂ O ₃	0.0435	0.0503	0.0559	0.0876	0.0703
Total	99.4	100	101	101	102
Elements (ppm)					
Si	208	165	207	279	244
Al	b.d.l.	b.d.l.	b.d.l.	b.d.l.	b.d.l.
Cr	959	952	1130	589	584
Fe	2500	2320	2500	2980	2930
Ni	b.d.l.	b.d.l.	b.d.l.	b.d.l.	b.d.l.
V	244	282	313	491	394
Nb	245	176	148	459	401
Zr	147	215	249	204	196
Thermometer (Tomki)					
In (Zr ppm)	4.99	5.37	5.52	5.32	5.28
P (Kbar)	11	11	11	11	11
Temperature (°C)	599	628	639	624	621
Error (2σ)*	27	23	22	24	24

Table S3 - EMPA major and trace element data for all lithologies

Lithology					
Type					
Analyses	17FJ02A_R3_3	17FJ02A_R3_4	17FJ02A_R3_7	17FJ02A_R3_8	17FJ02A_R4_2
Wt% oxide					
SiO ₂	0.0532	0.0514	0.109	0.0972	0.0423
TiO ₂	100	99.0	99.8	98.4	101
Al ₂ O ₃	b.d.l.	b.d.l.	0.0106	b.d.l.	b.d.l.
Cr ₂ O ₃	0.108	0.105	0.0813	0.0992	0.101
FeO	0.369	0.373	0.424	0.495	0.372
MnO	b.d.l.	0.00920	b.d.l.	b.d.l.	b.d.l.
NiO	b.d.l.	0.00615	b.d.l.	b.d.l.	b.d.l.
CaO	0.212	0.210	0.557	0.495	0.206
Nb ₂ O ₅	0.0512	0.0635	0.0482	0.0729	0.0283
ZrO ₂	0.0169	0.0242	0.0328	0.0622	0.0337
HfO ₂	b.d.l.	b.d.l.	0.0233	b.d.l.	0.0102
V ₂ O ₃	0.0814	0.0797	0.0586	0.0720	0.0843
Total	101	99.9	101	99.8	101
Elements (ppm)					
Si	249	240	511	454	198
Al	b.d.l.	b.d.l.	55.96	b.d.l.	b.d.l.
Cr	737	719	556	679	690
Fe	2870	2900	3290	3850	2890
Ni	b.d.l.	48.3	b.d.l.	b.d.l.	b.d.l.
V	456	446	328	404	472
Nb	358	444	337	509	198
Zr	125	179	242	460	249
Thermometer (Tomki)					
In (Zr ppm)	4.83	5.19	5.49	6.13	5.52
P (Kbar)	11	11	11	11	11
Temperature (°C)	588	614	637	690	639
Error (2σ)*	28	25	23	18	22

Table S3 - EMPA major and trace element data for all lithologies

Lithology					
Type					
Analyses	17FJ02A_R4_3	17FJ02A_R4_4	17FJ02A_R4_5	17FJ02A_R4_6	17FJ02A_R4_7
Wt% oxide					
SiO ₂	0.0406	0.0597	0.0920	0.0794	0.0867
TiO ₂	100	101	99.5	101	101
Al ₂ O ₃	b.d.l.	b.d.l.	b.d.l.	b.d.l.	b.d.l.
Cr ₂ O ₃	0.105	0.102	0.0983	0.0888	0.0933
FeO	0.364	0.439	0.473	0.480	0.511
MnO	b.d.l.	b.d.l.	0.00622	0.0125	b.d.l.
NiO	b.d.l.	b.d.l.	0.00603	b.d.l.	b.d.l.
CaO	0.252	0.320	0.441	0.413	0.467
Nb ₂ O ₅	0.0326	0.0345	0.0397	0.0353	0.0513
ZrO ₂	0.0486	0.0325	0.0373	0.0290	0.0505
HfO ₂	b.d.l.	0.0168	b.d.l.	b.d.l.	b.d.l.
V ₂ O ₃	0.0837	0.0648	0.0433	0.0669	0.0733
Total	101	102	101	103	102
Elements (ppm)					
Si	190	279	430	371	405
Al	b.d.l.	b.d.l.	b.d.l.	b.d.l.	b.d.l.
Cr	717	695	673	607	638
Fe	2830	3410	3680	3730	3970
Ni	b.d.l.	b.d.l.	47.4	b.d.l.	b.d.l.
V	469	363	242	375	411
Nb	228	241	278	246	359
Zr	360	241	276	215	374
Thermometer (Tomki)					
In (Zr ppm)	5.89	5.48	5.62	5.37	5.92
P (Kbar)	11	11	11	11	11
Temperature (°C)	669	637	647	628	672
Error (2σ)*	19	23	22	23	19

Table S3 - EMPA major and trace element data for all lithologies

Lithology					
Type					
Analyses	17FJ02A_R4_8	17FJ02A_R4_9	17FJ02A_R5_2	17FJ02A_R5_3	17FJ02A_R6_3
Wt% oxide					
SiO ₂	0.0752	0.0582	0.106	0.186	0.0662
TiO ₂	100	99.5	101	98.9	101
Al ₂ O ₃	0.00592	b.d.l	0.00713	0.0169	b.d.l
Cr ₂ O ₃	0.0832	0.0754	0.231	0.252	0.307
FeO	0.475	0.525	0.390	0.430	0.325
MnO	b.d.l.	b.d.l.	b.d.l.	b.d.l.	b.d.l.
NiO	b.d.l.	b.d.l.	b.d.l.	b.d.l.	b.d.l.
CaO	0.392	0.385	0.475	0.567	0.380
Nb ₂ O ₅	0.0502	0.0380	0.0539	0.0615	0.0282
ZrO ₂	0.0407	0.0293	0.0421	0.0624	0.0331
HfO ₂	b.d.l.	0.0198	b.d.l.	b.d.l.	b.d.l.
V ₂ O ₃	0.0684	0.0337	0.0456	0.0653	0.0654
Total	102	101	102	101	102
Elements (ppm)					
Si	352	272	497	871	310
Al	31.34	b.d.l	37.74	89.64	b.d.l.
Cr	569	516	1578	1724	2100
Fe	3690	4080	3030	3340	2530
Ni	b.d.l.	b.d.l.	b.d.l.	b.d.l.	b.d.l.
V	383	189	255	366	366
Nb	351	266	377	430	197
Zr	301	217	312	462	245
Thermometer (Tomki)					
ln (Zr ppm)	5.71	5.38	5.74	6.14	5.50
P (Kbar)	11	11	11	11	11
Temperature (°C)	654	629	657	690	638
Error (2σ)*	20	23	20	18	23

Table S3 - EMPA major and trace element data for all lithologies

Lithology Type	Fracture type-II halo				
	Analyses	17FJ02A_R6_4	17FJ02A_R6_5	17FJ06B_R1_1	17FJ06B_R1_2 17FJ06B_R1_3
Wt% oxide					
SiO ₂		0.0831	0.105	0.0827	0.0330 0.0501
TiO ₂		99.4	99.5	101	99.5 99.4
Al ₂ O ₃		b.d.l.	b.d.l.	b.d.l.	b.d.l. b.d.l.
Cr ₂ O ₃		0.271	0.279	0.0288	b.d.l. 0.0361
FeO		0.338	0.383	0.465	0.437 0.453
MnO		b.d.l.	b.d.l.	b.d.l.	0.0114 b.d.l.
NiO		b.d.l.	b.d.l.	0.0102	b.d.l. b.d.l.
CaO		0.408	0.524	0.594	0.543 0.582
Nb ₂ O ₅		0.0321	0.0279	0.0808	0.0772 0.0731
ZrO ₂		0.0178	0.0431	0.0322	0.0394 0.0485
HfO ₂		b.d.l.	b.d.l.	b.d.l.	b.d.l. b.d.l.
V ₂ O ₃		0.0766	0.0444	0.0305	0.0268 0.0268
Total		101	101	102	101 101
Elements (ppm)					
Si		388	489	387	154 234
Al		b.d.l.	b.d.l.	b.d.l.	b.d.l. b.d.l.
Cr		1853	1910	197	b.d.l. 247
Fe		2630	2980	3610	3400 3520
Ni		b.d.l.	b.d.l.	80.2	b.d.l. b.d.l.
V		429	249	171	150 150
Nb		225	195	565	539 511
Zr		132	319	238	291 359
Thermometer (Tomki)					
ln (Zr ppm)		4.88	5.77	5.47	5.67 5.88
P (Kbar)		11	11	12	12 12
Temperature (°C)		592	659	640	656 673
Error (2σ)*		27	20	23	22 19

Table S3 - EMPA major and trace element data for all lithologies

Lithology						Leucocratic domain
Type						Small
Analyses	17FJ06B_R1_4	17FJ06B_R1_5	17FJ06B_R2_2	17FJ06B_R2_3	FJ6a-1	R2
Wt% oxide						
SiO ₂	0.0951	0.204	0.722	0.188	0.0513	
TiO ₂	98.8	99.5	99.9	100	101	
Al ₂ O ₃	0.0140	0.155	b.d.l	0.0316	0.00889	
Cr ₂ O ₃	0.0320	0.0127	0.0177	0.101	0.0304	
FeO	0.496	0.500	0.194	0.193	0.342	
MnO	b.d.l.	b.d.l.	b.d.l.	b.d.l.	b.d.l.	
NiO	b.d.l.	b.d.l.	0.0586	0.0125	b.d.l.	
CaO	0.887	0.840	0.410	0.515	0.129	
Nb ₂ O ₅	0.0706	0.0723	0.0102	0.0197	0.166	
ZrO ₂	0.0379	0.0423	0.0635	0.0530	0.0223	
HfO ₂	b.d.l.	b.d.l.	b.d.l.	b.d.l.	b.d.l.	
V ₂ O ₃	0.0513	0.0396	0.0834	0.114	0.127	
Total	101	101	102	102	102	
Elements (ppm)						
Si	444	953	3370	877	240	
Al	74.18	822.18	b.d.l	167.10	47.07	
Cr	219	87.0	121	692	208	
Fe	3860	3890	1510	1500	2660	
Ni	b.d.l.	b.d.l.	461	98.6	b.d.l.	
V	287	222	467	637	710	
Nb	493	506	71.6	138	1160	
Zr	281	313	470	392	165	
Thermometer (Tomki)						
In (Zr ppm)	5.64	5.75	6.15	5.97	5.11	
P (Kbar)	12	12	12	12	12	
Temperature (°C)	653	662	696	681	612	
Error (2σ)*	22	20	18	19	25	

Table S3 - EMPA major and trace element data for all lithologies

Lithology								
Type	Large	Large	Large	Large	Large	LAB	LAB	LAB
Analyses	FJ6a-1 R5	FJ6a-1 R7	FJ6a-1 R9	FJ6a-1 R10	FJ6a-1 R11	FJ6a-1 R14	FJ6a-1 R15	FJ6a-1 R17
Wt% oxide								
SiO ₂	b.d.l.	0.00691	0.0134	0.0147	0.0116	b.d.l.	0.00778	b.d.l.
TiO ₂	101	101	101	101	101	101	100	101
Al ₂ O ₃	b.d.l.	b.d.l.	b.d.l.	0.0292	b.d.l.	b.d.l.	b.d.l.	b.d.l.
Cr ₂ O ₃	0.0282	0.0456	0.0501	0.0570	0.0334	0.0349	0.0269	0.0293
FeO	0.550	0.441	0.446	0.372	0.288	0.381	0.384	0.363
MnO	b.d.l.	b.d.l.	b.d.l.	b.d.l.	b.d.l.	b.d.l.	b.d.l.	0.00894
NiO	b.d.l.	b.d.l.	b.d.l.	b.d.l.	b.d.l.	0.00288	0.00593	b.d.l.
CaO	0.00440	0.00467	0.0202	0.0145	0.0246	0.00362	0.0180	0.00312
Nb ₂ O ₅	0.205	0.191	0.193	0.190	0.176	0.0685	0.0728	0.0612
ZrO ₂	0.1230	0.1173	0.0445	0.0440	0.122	0.110	0.122	0.0698
HfO ₂	b.d.l.	b.d.l.	b.d.l.	b.d.l.	b.d.l.	b.d.l.	b.d.l.	b.d.l.
V ₂ O ₃	0.109	0.119	0.140	0.134	0.195	0.257	0.278	0.269
Total	102	102	101	102	102	102	101	102
Elements (ppm)								
Si	b.d.l.	32.3	62.7	68.7	54.3	b.d.l.	36.3	b.d.l.
Al	b.d.l.	b.d.l.	b.d.l.	154.59	b.d.l.	b.d.l.	b.d.l.	b.d.l.
Cr	193	312	343	390	229	239	184	201
Fe	4270	3430	3470	2890	2240	2960	2990	2820
Ni	b.d.l.	b.d.l.	b.d.l.	b.d.l.	b.d.l.	22.6	46.6	b.d.l.
V	613	667	783	751	1090	1440	1560	1510
Nb	1440	1340	1350	1330	1230	479	509	428
Zr	911	869	329	326	906	813	903	516
Thermometer (Tomki)								
In (Zr ppm)	6.81	6.77	5.80	5.79	6.81	6.70	6.81	6.25
P (Kbar)	12	12	12	12	12	12	12	12
Temperature (°C)	758	753	666	665	758	747	757	705
Error (2σ)*	16	16	20	20	16	16	16	18

Table S3 - EMPA major and trace element data for all lithologies

Lithology							
Type	LAB	LAB	Large	Large	Small	Small	Large
Analyses	FJ6a-1 R19	FJ6a-1 R20	FJ6a-1 R21	FJ6a-1 R22	FJ6a-1 R1	FJ6a-1 R3	FJ6a-1 R4
Wt% oxide							
SiO ₂	0.0132	0.00717	0.0148	0.0238	0.0246	0.0387	0.0250
TiO ₂	101	100	100	101	102	102	101
Al ₂ O ₃	b.d.l	b.d.l	b.d.l	b.d.l	b.d.l	b.d.l	0.00635
Cr ₂ O ₃	0.0420	0.0064	b.d.l	0.0191	0.0585	0.0205	0.0591
FeO	0.440	0.407	0.316	0.315	0.354	0.362	0.493
MnO	b.d.l.	b.d.l.	b.d.l.	b.d.l.	0.00767	0.00859	0.00822
NiO	b.d.l.	b.d.l.	b.d.l.	b.d.l.	b.d.l.	b.d.l.	b.d.l.
CaO	0.0088	0.0143	0.0587	0.0524	0.0189	0.0823	0.0141
Nb ₂ O ₅	0.0720	0.0718	0.0383	0.0224	0.121	0.0970	0.186
ZrO ₂	0.123	0.104	0.0439	0.0310	0.0353	0.0131	0.0855
HfO ₂	b.d.l.	b.d.l.	b.d.l.	b.d.l.	b.d.l.	b.d.l.	b.d.l.
V ₂ O ₃	0.250	0.250	0.162	0.163	0.150	0.132	0.117
Total	102	101	101	101	103	103	102
Elements (ppm)							
Si	61.6	33.5	69.2	111	115	181	117
Al	b.d.l	b.d.l	b.d.l	b.d.l	b.d.l	b.d.l	33.6
Cr	287	43.7	b.d.l	131	400	140	404
Fe	3420	3170	2460	2450	2750	2810	3830
Ni	b.d.l.	b.d.l.	b.d.l.	b.d.l.	b.d.l.	b.d.l.	b.d.l.
V	1400	1400	908	915	838	738	657
Nb	503	502	268	157	845	678	1300
Zr	909	767	325	230	262	97.1	633
Thermometer (Tomki)							
In (Zr ppm)	6.81	6.64	5.78	5.44	5.57	4.58	6.45
P (Kbar)	12	12	12	12	12	12	12
Temperature (°C)	758	741	665	637	669	598	755
Error (2σ)*	16	17	20	23	22	32	17

Table S3 - EMPA major and trace element data for all lithologies

Lithology					
Type	Large	LAB	LAB	LAB	LAB
Analyses	FJ6a-1 R6	FJ6a-1 R12	FJ6a-1 R13	FJ6a-1 R16	FJ6a-1 R18
Wt% oxide					
SiO ₂	0.0120	0.0146	0.00742	b.d.l.	0.00590
TiO ₂	101	101	102	101	101
Al ₂ O ₃	b.d.l.	0.00627	b.d.l.	b.d.l.	0.0175
Cr ₂ O ₃	0.0346	0.0530	0.0332	0.0177	0.0289
FeO	0.478	0.311	0.257	1.13	0.381
MnO	b.d.l.	b.d.l.	b.d.l.	b.d.l.	b.d.l.
NiO	b.d.l.	b.d.l.	b.d.l.	b.d.l.	b.d.l.
CaO	0.0160	0.0143	0.00788	0.00346	0.00253
Nb ₂ O ₅	0.192	0.0534	0.0584	0.0282	0.0651
ZrO ₂	0.0650	0.0472	0.0788	0.0390	0.0928
HfO ₂	b.d.l.	b.d.l.	b.d.l.	b.d.l.	b.d.l.
V ₂ O ₃	0.151	0.281	0.273	0.293	0.296
Total	102	102	102	102	102
Elements (ppm)					
Si	56.2	68.3	34.7	b.d.l.	27.6
Al	b.d.l.	33.2	b.d.l.	b.d.l.	92.7
Cr	236	362	227	121	198
Fe	3720	2410	2000	8790	2960
Ni	b.d.l.	b.d.l.	b.d.l.	b.d.l.	b.d.l.
V	845	1570	1530	1640	1660
Nb	1340	373	408	197	455
Zr	481	350	584	288	687
Thermometer (Tomkins)					
ln (Zr ppm)	6.18	5.86	6.37	5.66	6.53
P (Kbar)	12	12	12	12	12
Temperature (°C)	734	710	761	702	786
Error (2σ)*	18	19	17	21	17

Table S4a - LA-ICP-MS U-Pb data for large rutile grains in leucocratic domains

Grain	Analyses	Distance from grain boundary (μm)	U (ppm)	Pb _c	Ratios						Ages		
					<i>f</i> 206%	²⁰⁷ Pb/ ²³⁵ U	±2σ	²⁰⁶ Pb/ ²³⁸ U	±2σ	²⁰⁷ Pb/ ²⁰⁶ Pb	±2σ	rho	²⁰⁶ Pb/ ²³⁸ U
1	1_1-1	77	8.99	4.9	0.477	0.040	0.0644	0.0020	0.0537	0.0041	0.37	402	
	1_1-2	69	4.96	8.0	0.470	0.056	0.0643	0.0019	0.0530	0.0061	0.25	402	
2	1_2-1	31	5.06	7.5	0.488	0.062	0.0645	0.0018	0.0549	0.0068	0.22	403	
	1_2-2	167	8.70	4.1	0.480	0.047	0.0637	0.0024	0.0547	0.0049	0.39	398	
	1_2-3	173	10.5	3.6	0.483	0.036	0.0641	0.0021	0.0546	0.0037	0.43	401	
	1_2-4	10	8.6	4.8	0.479	0.038	0.0645	0.0019	0.0538	0.0040	0.37	403	
	1_2-5	10	8.01	5.8	0.472	0.051	0.0626	0.0026	0.0548	0.0055	0.38	391	
3	1_3-1	55	3.39	6.8	0.570	0.079	0.0734	0.0030	0.0563	0.0075	0.30	456	
	1_3-2	95	7.80	3.7	0.508	0.053	0.0667	0.0041	0.0553	0.0047	0.59	416	
4	1_4-1	97	23.5	1.7	0.458	0.038	0.0584	0.0037	0.0569	0.0030	0.77	366	
	1_4-2	114	3.72	8.9	0.628	0.076	0.0715	0.0024	0.0637	0.0074	0.28	445	
5	1_5-1	80	6.25	5.4	0.476	0.071	0.0634	0.0027	0.0545	0.0077	0.29	396	
	1_5-2	126	8.12	3.9	0.484	0.043	0.0647	0.0023	0.0542	0.0044	0.40	404	
	1_5-3	105	7.94	3.9	0.489	0.041	0.0645	0.0029	0.0550	0.0039	0.53	403	
	1_5-4	10	5.22	5.9	0.494	0.057	0.0650	0.0038	0.0550	0.0054	0.50	406	
6	1_5-5	64	8.68	6.0	0.451	0.045	0.0613	0.0023	0.0534	0.0050	0.37	383	
	1_5-6	154	9.32	3.8	0.487	0.037	0.0650	0.0023	0.0543	0.0037	0.46	406	
	1_5-8	92	7.03	4.4	0.488	0.044	0.0641	0.0037	0.0552	0.0038	0.65	401	
7	2_D-5	36	13.8	2.7	0.479	0.040	0.0645	0.0041	0.0538	0.0029	0.77	403	
8	2_G-1	90	7.51	4.9	0.480	0.032	0.0639	0.0018	0.0545	0.0034	0.41	399	
9	3_C-2	80	5.12	5.9	0.542	0.068	0.0641	0.0047	0.0613	0.0062	0.58	401	
10	3_G2-2	84	7.74	4.0	0.499	0.056	0.0660	0.0033	0.0549	0.0055	0.44	412	
	3_G2-3	40	8.47	3.3	0.498	0.050	0.0660	0.0029	0.0547	0.0050	0.43	412	
11	3_K-1	86	7.78	3.9	0.525	0.040	0.0686	0.0021	0.0556	0.0039	0.39	428	
	3_K-2	142	6.95	4.3	0.519	0.061	0.0698	0.0024	0.0539	0.0060	0.30	435	
	3_K-3	89	5.42	6.0	0.502	0.068	0.0654	0.0026	0.0557	0.0073	0.29	408	
12	4_BI-3	22	4.35	8.8	0.508	0.059	0.0667	0.0039	0.0552	0.0056	0.50	417	
13	4_I-1	33	5.26	6.9	0.562	0.066	0.0726	0.0038	0.0562	0.0059	0.44	451	

Table S4a - LA-ICP-MS U-Pb data for large rutile grains in leucocratic domains

		<i>f</i> 206%		²⁰⁷ Pb/ ²³⁵ U	±2σ	²⁰⁶ Pb/ ²³⁸ U	±2σ	²⁰⁷ Pb/ ²⁰⁶ Pb	±2σ	rho	²⁰⁶ Pb/ ²³⁸ U
14 4_M-2	69	4.33	4.6	0.458	0.054	0.0643	0.0044	0.0517	0.0049	0.59	402
15 4_N-5	33	8.74	3.9	0.485	0.046	0.0674	0.0020	0.0523	0.0048	0.31	420
4_N-6	74	7.22	4.7	0.510	0.051	0.0699	0.0019	0.0529	0.0051	0.27	436
16 4_NII-2	36	8.00	5.0	0.541	0.048	0.0712	0.0034	0.0552	0.0041	0.54	443
17 5_D-1	47	11.3	3.0	0.497	0.044	0.0646	0.0034	0.0558	0.0040	0.59	404
5_D-2	49	3.42	9.9	0.496	0.072	0.0671	0.0029	0.0536	0.0074	0.30	419
5_D-3	160	17.4	2.3	0.492	0.042	0.0656	0.0026	0.0544	0.0041	0.47	410
5_D-4	20	6.50	4.7	0.573	0.046	0.0738	0.0029	0.0563	0.0039	0.49	459
5_D-5	46	13.0	2.9	0.484	0.030	0.0682	0.0025	0.0516	0.0026	0.60	425
18 6_B-2	43	4.35	7.7	0.603	0.079	0.0773	0.0036	0.0566	0.0069	0.36	480
19 6_G2-2	27	10.9	3.1	0.544	0.029	0.0718	0.0017	0.0550	0.0026	0.45	447
6_G2-3	36	6.13	5.2	0.544	0.048	0.0704	0.0022	0.0560	0.0046	0.36	439
6_G2-4	28	4.43	7.1	0.577	0.088	0.0742	0.0022	0.0564	0.0084	0.19	461
20 6_H1-1	24	12.0	2.7	0.526	0.040	0.0687	0.0015	0.0555	0.0041	0.29	428
6_H1-2	73	12.6	2.8	0.521	0.029	0.0672	0.0019	0.0563	0.0027	0.50	419
6_H1-3	70	14.4	2.5	0.530	0.032	0.0686	0.0026	0.0560	0.0026	0.63	428
6_H1-4	67	14.0	2.6	0.555	0.038	0.0684	0.0023	0.0589	0.0036	0.48	426
21 6_H1-6	46	9.90	3.4	0.526	0.043	0.0691	0.0029	0.0552	0.0039	0.51	431
6_H1-7	9	12.1	3.0	0.523	0.041	0.0686	0.0020	0.0553	0.0041	0.37	427
22 6_H3-1	33	9.93	3.5	0.493	0.030	0.0683	0.0021	0.0523	0.0028	0.50	426
6_H3-3	46	13.7	2.7	0.503	0.044	0.0699	0.0049	0.0522	0.0027	0.81	435
23 6_J1-2	37	11.9	3.4	0.491	0.057	0.0642	0.0053	0.0555	0.0045	0.71	401
6_J1-3	73	5.37	7.1	0.497	0.068	0.0647	0.0028	0.0558	0.0072	0.32	404
24 7_E-1	34	4.35	6.2	0.526	0.058	0.0670	0.0025	0.0570	0.0059	0.34	418
25 7_G1-3	252	9.79	4.8	0.445	0.031	0.0622	0.0013	0.0520	0.0034	0.31	389
7_G1-4	144	8.31	3.1	0.530	0.037	0.0697	0.0025	0.0552	0.0033	0.51	434
7_G1-5	60	12.5	2.2	0.483	0.027	0.0639	0.0025	0.0548	0.0023	0.68	400
7_G1-6	170	9.28	2.8	0.500	0.032	0.0648	0.0021	0.0560	0.0030	0.52	405
7_G1-7	71	9.09	3.1	0.447	0.034	0.0598	0.0019	0.0541	0.0038	0.42	375
26 7_G2-1	35	7.36	3.8	0.521	0.044	0.0653	0.0020	0.0578	0.0045	0.37	408
7_G2-2	56	5.80	4.9	0.484	0.038	0.0642	0.0018	0.0547	0.0040	0.37	401

Table S4a - LA-ICP-MS U-Pb data for large rutile grains in leucocratic domains

			<i>f</i> 206%	²⁰⁷ Pb/ ²³⁵ U	±2σ	²⁰⁶ Pb/ ²³⁸ U	±2σ	²⁰⁷ Pb/ ²⁰⁶ Pb	±2σ	rho	²⁰⁶ Pb/ ²³⁸ U
7_G2-3	62	12.2	2.3	0.511	0.026	0.0679	0.0017	0.0546	0.0024	0.50	424
7_G2-4	33	3.90	7.8	0.538	0.060	0.0711	0.0020	0.0549	0.0059	0.25	443
27 7_L1-1	56	7.07	3.4	0.484	0.045	0.0643	0.0033	0.0546	0.0042	0.55	402
7_L1-2	21	12.4	2.5	0.472	0.037	0.0665	0.0026	0.0515	0.0035	0.51	415
7_L1-3	143	13.9	2.1	0.499	0.040	0.0660	0.0030	0.0548	0.0037	0.56	412
7_L1-4	26	12.1	2.4	0.518	0.031	0.0679	0.0020	0.0553	0.0028	0.50	423
7_L1-6	6	9.21	2.6	0.489	0.038	0.0650	0.0036	0.0546	0.0031	0.70	406
28 7_L2-1	30	8.04	3.4	0.617	0.050	0.0788	0.0026	0.0568	0.0042	0.41	489
7_L2-2	60	12.1	2.8	0.542	0.045	0.0708	0.0044	0.0555	0.0031	0.74	441

Table S4a - LA-ICP-MS U-Pb data for large rutile grains in leucocratic domains

Grain	Analyses		Discordance (%)		Peak age on radial plot (Fig. 10e)	Mean grain age	Mean grain age		Mean ratios	
	$\pm 2\sigma$	$^{207}\text{Pb}/^{235}\text{U}$	$\pm 2\sigma$	$^{207}\text{Pb}/^{235}\text{U} /$ $(^{206}\text{Pb}/^{238}\text{U})$		$^{207}\text{Pb}/^{235}\text{U}$	$\pm 2\sigma$	$^{206}\text{Pb}/^{238}\text{U}$	$\pm 2\sigma$	$^{207}\text{Pb}/^{235}\text{U}$
1 1_1-1	12	396	27	1.6	1	394	22	402	8.3	0.475
1 1_1-2	11	391	39	2.7	1					
2 1_2-1	11	403	43	-0.15	1	398	14	400	5.7	0.480
1 2_2-2	15	398	32	-0.024	1					
1 2_2-3	12	400	25	0.19	1					
1 2_2-4	11	397	26	1.5	1					
1 2_2-5	16	393	35	-0.42	1					
3 1_3-1	18	458	51	-0.33	2	431	29	442	15	0.527
1 3_3-2	25	417	36	-0.27	1					
4 1_4-1	23	383	26	-4.6	exc.	409	23	422	12	0.490
1 4_4-2	15	495	48	-11	1					
5 1_5-1	17	396	49	0.10	1	403	17	402	8.5	0.487
1 5_5-2	14	400	29	0.9	1					
1 5_5-3	18	404	28	-0.34	1					
1 5_5-4	23	407	38	-0.27	1					
6 1_5-5	14	378	32	1.4	1	393	20	396	8.9	0.477
1 5_5-6	14	403	25	0.77	1					
1 5_5-8	23	404	30	-0.75	1					
7 2_D-5	25	397	27	1.5	1	397	27	403	25	0.479
8 2_G-1	11	398	22	0.29	1	398	22	399	11	0.480
9 3_C-2	28	440	45	-9.8	exc.	440	45	401	28	0.542
10 3_G2-2	20	411	38	0.13	1	411	25	412	13	0.499
3_G2-3	17	410	34	0.46	1					
11 3_K-1	12	429	27	-0.28	2	427	22	425	8.1	0.519
3_K-2	15	425	40	2.4	2					
3_K-3	16	413	46	-1.2	1					
12 4_BI-3	24	417	40	-0.21	1	417	40	417	24	0.508
13 4_I-1	23	453	43	-0.34	2	453	43	451	23	0.562

Table S4a - LA-ICP-MS U-Pb data for large rutile grains in leucocratic domains

	$\pm 2\sigma$	$^{207}\text{Pb}/^{235}\text{U}$	$\pm 2\sigma$	$\frac{^{207}\text{Pb}/^{235}\text{U}}{(^{206}\text{Pb}/^{238}\text{U})}$		$^{207}\text{Pb}/^{235}\text{U}$	$\pm 2\sigma$	$^{206}\text{Pb}/^{238}\text{U}$	$\pm 2\sigma$	$^{207}\text{Pb}/^{235}\text{U}$
14 4_M-2	27	383	37	4.7	1	383	37	402	27	0.458
15 4_N-5	12	402	32	4.4	2	409	23	428	8.2	0.496
4_N-6	11	418	34	4.0	2					
16 4_NII-2	21	439	32	0.88	2	439	32	443	21	0.541
17 5_D-1	20	410	30	-1.5	1	415	13	411	10	0.504
5_D-2	17	409	49	2.3	1					
5_D-3	16	407	29	0.77	1					
5_D-4	17	460	30	-0.26	2					
5_D-5	15	401	21	5.6	exc.					
18 6_B-2	22	479	50	0.16	2	479	50	480	22	0.603
19 6_G2-2	10	441	19	1.3	2	443	16	449	7.0	0.547
6_G2-3	13	441	32	-0.51	2					
6_G2-4	13	463	57	-0.27	2					
20 6_H1-1	9.1	429	27	-0.15	2	433	11	426	5.8	0.531
6_H1-2	11	426	19	-1.6	2					
6_H1-3	15	432	21	-0.92	2					
6_H1-4	14	448	25	-5.1	exc.					
21 6_H1-6	17	429	29	0.30	2	428	20	429	10	0.524
6_H1-7	12	427	28	0.13	2					
22 6_H3-1	13	407	21	4.5	2	409	17	424	11	0.496
6_H3-3	30	414	30	5.0	exc.					
23 6_J1-2	32	406	39	-1.2	1	407	30	403	15	0.494
6_J1-3	17	410	46	-1.5	1					
24 7_E-1	15	429	39	-2.7	1	429	39	418	15	0.526
25 7_G1-3	8.1	374	22	3.8	1	398	10	390	5.5	0.479
7_G1-4	15	432	24	0.50	2					
7_G1-5	15	400	19	-0.15	1					
7_G1-6	13	412	21	-1.8	1					
7_G1-7	12	375	24	-0.086	1					
26 7_G2-1	12	426	29	-4.3	1	418	12	419	7.8	0.509
7_G2-2	11	401	26	0.042	1					

Table S4a - LA-ICP-MS U-Pb data for large rutile grains in leucocratic domains

	$\pm 2\sigma$	$^{207}\text{Pb}/^{235}\text{U}$	$\pm 2\sigma$	$\frac{^{207}\text{Pb}/^{235}\text{U}}{(^{206}\text{Pb}/^{238}\text{U})}$		$^{207}\text{Pb}/^{235}\text{U}$	$\pm 2\sigma$	$^{206}\text{Pb}/^{238}\text{U}$	$\pm 2\sigma$	$^{207}\text{Pb}/^{235}\text{U}$
7_G2-3	10	419	17	1.1	2					
7_G2-4	12	437	40	1.3	2					
27 7_L1-1	20	401	31	0.16	1	409	11	415	8.3	0.495
7_L1-2	16	393	26	5.3	exc.					
7_L1-3	18	411	27	0.24	1					
7_L1-4	12	424	21	-0.11	2					
7_L1-6	22	404	26	0.39	1					
28 7_L2-1	16	488	31	0.22	2	462	22	477	13	0.580
7_L2-2	26	440	30	0.32	2					

Table S4a - LA-ICP-MS U-Pb data for large rutile grains in leucocratic domains

Grain	Analyses				Mean rho	Grain diameter (μm)	Grain orientation spread (°)
		±2σ	²⁰⁶ Pb/ ²³⁸ U	±2σ			
1	1_1-1	0.032	0.064	0.001	0.310	352	0.35
	1_1-2						
2	1_2-1	0.020	0.064	0.001	0.356	660	0.3
	1_2-2						
	1_2-3						
	1_2-4						
	1_2-5						
3	1_3-1	0.044	0.071	0.041	0.442	366	0.44
	1_3-2						
4	1_4-1	0.860	0.068	0.077	0.524	512	4.4
	1_4-2						
5	1_5-1	0.025	0.064	0.001	0.432	481	0.38
	1_5-2						
	1_5-3						
	1_5-4						
6	1_5-5	0.024	0.063	0.005	0.490	679	3.7
	1_5-6						
	1_5-8						
7	2_D-5	0.040	0.065	0.004	0.765	511	3.0
8	2_G-1	0.032	0.064	0.002	0.415	396	0.88
9	3_C-2	0.068	0.064	0.005	0.585	337	0.82
10	3_G2-2	0.037	0.066	0.002	0.439	459	0.53
	3_G2-3						
11	3_K-1	0.030	0.068	0.005	0.327	666	2.1
	3_K-2						
	3_K-3						
12	4_BI-3	0.059	0.067	0.004	0.503	224	6.1
13	4_I-1	0.066	0.073	0.004	0.444	368	0.42

Table S4a - LA-ICP-MS U-Pb data for large rutile grains in leucocratic domains

	$\pm 2\sigma$	$^{206}\text{Pb}/^{238}\text{U}$	$\pm 2\sigma$			
14 4_M-2	0.054	0.064	0.004	0.589	361	0.54
15 4_N-5	0.034	0.069	0.016	0.288	428	1.5
4_N-6						
16 4_NII-2	0.048	0.071	0.003	0.541	229	0.16
17 5_D-1	0.043	0.068	0.004	0.490	471	0.38
5_D-2						
5_D-3						
5_D-4						
5_D-5						
18 6_B-2	0.079	0.077	0.004	0.357	276	1.4
19 6_G2-2	0.024	0.072	0.004	0.333	311	0.52
6_G2-3						
6_G2-4						
20 6_H1-1	0.017	0.068	0.001	0.474	464	0.34
6_H1-2						
6_H1-3						
6_H1-4						
21 6_H1-6	0.030	0.069	0.002	0.440	315	1.5
6_H1-7						
22 6_H3-1	0.025	0.069	0.002	0.654	392	0.51
6_H3-3						
23 6_J1-2	0.044	0.065	0.002	0.516	328	0.52
6_J1-3						
24 7_E-1	0.058	0.067	0.003	0.343	376	0.5
25 7_G1-3	0.042	0.063	0.004	0.490	774	4.7
7_G1-4						
7_G1-5						
7_G1-6						
7_G1-7						
26 7_G2-1	0.018	0.067	0.005	0.371	588	1.1
7_G2-2						

Table S4a - LA-ICP-MS U-Pb data for large rutile grains in leucocratic domains

	$\pm 2\sigma$	$^{206}\text{Pb}/^{238}\text{U}$	$\pm 2\sigma$		
7_G2-3					
7_G2-4					
27 7_L1-1	0.017	0.066	0.537	521	0.38
7_L1-2					
7_L1-3					
7_L1-4					
7_L1-6					
28 7_L2-1	0.480		0.740	320	0.29
7_L2-2					

Table S4b - SHRIMP U-Pb data for large rutile grains in leucocratic domains

Grain	Analyses	U (ppm)	Pb _c	Ratios						Ages				
				<i>f</i> 206%	²⁰⁷ Pb/ ²³⁵ U	±2σ	²⁰⁶ Pb/ ²³⁸ U	±2σ	²⁰⁷ Pb/ ²⁰⁶ Pb	±2σ	rho	²⁰⁶ Pb/ ²³⁸ U	±2σ	²⁰⁷ Pb/ ²³⁵ U
29	N17-44A1-3	12.3	0.41	0.524	0.013	0.0659	0.0011	0.0577	0.0011	0.64		411	6.4	428
	N17-44A.1-6	8.90	0.58	0.484	0.013	0.0644	0.00097	0.0545	0.0013	0.52		402	5.9	401
	N17-44A.1-7	8.47	0.79	0.506	0.014	0.0659	0.00099	0.0556	0.0013	0.50		411	6.0	416
	N17-44A.1-9	8.70	0.81	0.456	0.013	0.0636	0.00095	0.0521	0.0013	0.49		397	5.8	381
	N17-44A.1-11	9.01	0.77	0.504	0.015	0.0665	0.0014	0.0549	0.0013	0.63		415	8.4	414
30	N17-44B.2-2	6.92	1.2	0.500	0.024	0.0642	0.0013	0.0565	0.0024	0.38		401	7.8	412
	N17-44B.2-10	5.11	1.1	0.515	0.043	0.0675	0.0014	0.0554	0.0044	0.25		421	8.6	422
31	N17-44C.1-2	10.9	0.92	0.491	0.021	0.0669	0.0013	0.0532	0.0020	0.42		417	8.1	406
	N17-44C.1-3	11.0	0.60	0.508	0.014	0.0672	0.0012	0.0549	0.0012	0.61		419	7.3	417
	N17-44C.1-4	7.89	0.73	0.517	0.020	0.0663	0.0021	0.0565	0.0014	0.76		414	12	423
	N17-44C.1-5	7.14	0.75	0.509	0.020	0.0652	0.0019	0.0566	0.0016	0.68		407	11	418
	N17-44C.1-6	6.25	0.95	0.520	0.023	0.0662	0.0030	0.0570	0.0018	0.76		413	18	425
	N17-44C.1-8	7.75	1.1	0.522	0.017	0.0673	0.0015	0.0562	0.0015	0.64		420	9.4	426
	N17-44C.1-9	5.27	1.3	0.516	0.019	0.0654	0.0016	0.0572	0.0018	0.53		408	9.5	422
	N17-44C.1-16	9.47	0.73	0.518	0.017	0.0674	0.0017	0.0557	0.0012	0.72		420	10	424
	N17-44C.1-17	10.1	0.75	0.519	0.017	0.0674	0.0017	0.0557	0.0012	0.72		420	10	424
32	N17-44E.1-2	13.6	0.51	0.476	0.019	0.0636	0.0014	0.0543	0.0018	0.53		397	8.5	395
	N17-44E.1-3	13.8	0.46	0.498	0.020	0.0649	0.0015	0.0556	0.0018	0.56		405	9.0	410
	N17-44E.1-4	13.0	0.66	0.474	0.018	0.0606	0.0011	0.0567	0.0019	0.44		379	6.6	394
	N17-44E.1-5	13.5	0.66	0.489	0.030	0.0634	0.0016	0.0559	0.0031	0.42		396	10	404
	N17-44E.1-6	13.7	0.66	0.489	0.030	0.0634	0.0016	0.0559	0.0031	0.42		396	10	404
33	N17-44G.1-10	10.2	0.65	0.553	0.017	0.0706	0.0016	0.0569	0.0013	0.77		440	9.4	447
	N17-44G.1-12	10.8	0.66	0.524	0.013	0.0689	0.0010	0.0551	0.0011	0.37		430	6.2	428
	N17-44G.1-13	8.44	0.43	0.544	0.013	0.0703	0.0012	0.0561	0.0010	0.31		438	7.2	441
	N17-44G.1-16	7.59	0.41	0.533	0.011	0.0711	0.0010	0.0543	0.00087	0.51		443	6.0	434
	N17-44G.1-17	11.1	0.38	0.528	0.011	0.0704	0.00092	0.0544	0.00082	0.66		439	5.5	430
	N17-44G.1-2	8.24	1.3	0.526	0.023	0.0697	0.0013	0.0547	0.0021	0.67		434	8.0	429
	N17-44G.1-3	9.58	1.1	0.523	0.017	0.0690	0.0019	0.0550	0.0012	0.56		430	11	427
	N17-44G.1-4	11.7	0.50	0.521	0.019	0.0685	0.0013	0.0552	0.0019	0.68		427	7.9	426
	N17-44G.1-5	15.2	1.4	0.532	0.024	0.0732	0.0014	0.0527	0.0023	0.63		455	8.4	433
	N17-44G.1-6	15.8	0.89	0.527	0.014	0.0706	0.0024	0.0541	0.0016	0.64		440	14	430

Table S4b - SHRIMP U-Pb data for large rutile grains in leucocratic domains

Grain	Analyses	U (ppm)	Pb _c	Ratios							Ages			
				<i>f</i> 206%	²⁰⁷ Pb/ ²³⁵ U	±2σ	²⁰⁶ Pb/ ²³⁸ U	±2σ	²⁰⁷ Pb/ ²⁰⁶ Pb	±2σ	rho	²⁰⁶ Pb/ ²³⁸ U	±2σ	²⁰⁷ Pb/ ²³⁵ U
	N17-44G.1-7	9.46	0.86		0.578	0.016	0.0719	0.0015	0.0583	0.0012	0.40	448	9.1	463

Table S4b - SHRIMP U-Pb data for large rutile grains in leucocratic domains

Grain	Analyses	Discordance (%)		Mean grain age	Grain diameter (μm)	Grain orientation spread (°)	
		$\pm 2\sigma$	$(^{206}\text{Pb}/^{238}\text{U} - ^{207}\text{Pb}/^{235}\text{U}) / (^{206}\text{Pb}/^{238}\text{U})$	$^{206}\text{Pb}/^{238}\text{U}$	$\pm 2\sigma$		
29	N17-44A1-3	8.7	-4.0	406	2.8	384	3.9
	N17-44A.1-6	8.9	0.38				
	N17-44A.1-7	9.6	-1.1				
	N17-44A.1-9	8.9	4.0				
	N17-44A.1-11	10	0.15				
30	N17-44B.2-2	16	-2.6	410	7.0	n.m	n.m
	N17-44B.2-10	29	-0.17				
31	N17-44C.1-2	14	2.8	416	3.5	896	2.8
	N17-44C.1-3	9.2	0.52				
	N17-44C.1-4	14	-2.3				
	N17-44C.1-5	13	-2.6				
	N17-44C.1-6	16	-2.9				
	N17-44C.1-8	12	-1.6				
	N17-44C.1-9	13	-3.5				
	N17-44C.1-16	11	-0.79				
32	N17-44E.1-2	13	0.54	393	5.4	n.m	n.m
	N17-44E.1-3	14	-1.2				
	N17-44E.1-4	12	-3.9				
	N17-44E.1-5	20	-2.0				
33	N17-44G.1-10	11	-1.6	437	2.4	483	0.69
	N17-44G.1-12	8.7	0.40				
	N17-44G.1-13	8.6	-0.71				
	N17-44G.1-16	7.4	2.0				
	N17-44G.1-17	7.0	1.8				
	N17-44G.1-2	15	1.2				
	N17-44G.1-3	12	0.69				
	N17-44G.1-4	13	0.30				
	N17-44G.1-5	16	4.9				
	N17-44G.1-6	9.5	2.3				

Table S4b - SHRIMP U-Pb data for large rutile grains in leucocratic domains

Grain	Analyses	Discordance (%)	Mean grain age	Grain diameter (μm)	Grain orientation spread (°)
		$\frac{(^{206}\text{Pb}/^{238}\text{U} - ^{207}\text{Pb}/^{235}\text{U})}{(^{206}\text{Pb}/^{238}\text{U})}$	$^{206}\text{Pb}/^{238}\text{U}$		
	$\pm 2\sigma$		$\pm 2\sigma$		
N17-44G.1-7	10	-3.5			